Tailored Laser-Droplet Interaction

for target formation in extreme ultraviolet sources

Ph.D. thesis, Vrije Universiteit Amsterdam, 2021
Tailored Laser-Droplet Interaction for Target Formation in Extreme Ultraviolet Sources.
Randy A. Meijer

ISBN 978-94-92323-57-6
An electronic version of this dissertation is available at: research.vu.nl

VRIJE UNIVERSITEIT

Tailored Laser-Droplet Interaction

for target formation in extreme ultraviolet sources

ACADEMISCH PROEFSCHRIFT

ter verkrijging van de graad van Doctor of Philosophy
aan de Vrije Universiteit Amsterdam,
op gezag van de rector magnificus
prof.dr. V. Subramaniam,
in het openbaar te verdedigen
ten overstaan van de promotiecommissie
van de Faculteit der Bètawetenschappen
op maandag 4 oktober 2021 om 11.45 uur
in de aula van de universiteit,
De Boelelaan 1105

door

Randy Anthonius Meijer

geboren te Amsterdam

promotoren: dr. S.M. Witte
prof.dr. K.S.E. Eikema

This thesis was approved by the members of the reading committee:

prof.dr.ir. J.P.H. Benschop	Universiteit Twente
dr.ir. H. Gelderblom	Technische Universiteit Eindhoven
prof.dr. J. Limpert	Friedrich-Schiller-Universität Jena
dr. D. van Oosten	Universiteit Utrecht
prof.dr. W.M.G. Ubachs	Vrije Universiteit Amsterdam

The work described in this thesis was carried out at the Advanced Research Center for Nanolithography (ARCNL), a public-private partnership between the University of Amsterdam (UvA), the Vrije Universiteit Amsterdam (VU), the Netherlands Organisation for Scientific Research (NWO), and the semiconductor equipment manufacturer ASML.

Contents

Chapter 1

Introduction

Although it is Prometheus often accredited with bringing *the gift of fire* to mankind [1], it wasn't long before we figured out how to rub sticks together and strike flint [2]. Ever since, we have been able to create light when we needed it, allowing us to observe the world around us[1] in the absence of the sun and the moon. Nowadays, many man-made sources of light, or electromagnetic radiation, are abundant and have left their mark on science and society. Among them are the incandescent light bulb, light-emitting diodes, x-ray tubes, lasers, synchrotrons, and various plasma sources. History has shown us that with any advances in light-source development, for example by increasing intensity or efficiency, or covering a previously unreachable part of the electromagnetic spectrum, came new applications and technological progress. In some cases the roles are reversed, where development of new light sources is directly driven by the needs and foresight of society and industry. This is the case for enabling extreme ultraviolet lithography, where a high-power source is required that supplies light at a specific wavelength of 13.5 nm.

[1] Or to take a selfie in a dark nightclub.

1.1. Extreme ultraviolet lithography

Modern, everyday life is without a doubt dominated by the technology that surrounds us. The generation, flow, and consumption of content and information has never been this large, and is increasing at rapid pace [3]. This is the result of the ever-increasing capacity, complexity, and crucially, availability of integrated circuits. An integrated circuit (IC) is, as the name suggests, a multitude of electronic components and circuits integrated together in a single (flat) piece of semiconductor material (almost always silicon), also referred to as a microchip. Well-known examples are the central and graphics processing units (CPU & GPU)[2] in the personal computers and smartphones we use every day.

Lithography using light, or *photolithography*, is the main technique enabling the mass production of integrated circuits. In photolithography, a mask containing the to-be-transferred pattern is illuminated by a light source and its transmission or reflection subsequently imaged onto a photosensitive material (resist). This core step, termed the *exposure* step, is the starting point of the patterning procedure and sets the initial dimensions of the "printed" structures. The complete IC structure is then built up in a repeating combination of chemical development, etching, ion implantation, deposition, and exposure steps [4].

The transistor is the fundamental component of essentially all ICs, since the ability of the transistor to "switch" is what allows bits to be stored and computations to be performed. By decreasing the size of transistors, the packing density can be increased and more of them can be placed on a single chip. As a result the chip's total efficiency and computational power, or storage capacity in the case of memory chips, will increase. This process of miniaturization has continued for decades: It is what has ultimately led to powerful and widely available microchips, capable of performing billions of permutations per second, being implemented in so many devices we use on a daily basis.

Fundamentally, the lateral resolution Δx of an imaging system is limited by the diffraction limit [5], given by

$$\Delta x = \frac{\lambda}{2\mathrm{NA}}, \tag{1.1}$$

with λ the wavelength of the light and NA the numerical aperture of the imaging system. Therefore, to increase the resolution of the exposure step the NA can be increased or λ decreased. In industry, the central enabler of the aforementioned miniaturization has been the decrease of the exposure wavelength, typically followed by increases in NA within each wavelength generation. Early photolithography systems designed for the fabrication of ICs made use of light with a wavelength of 436 nm supplied by mercury arc lamps [6]. Since then the wavelength has stepwise decreased, starting with 365 nm, also supplied by mercury lamps, followed by deep ultraviolet (DUV) 248 nm and 193 nm wavelengths supplied by KrF and ArF excimer lasers, respectively. To continue facilitating a shrinking of the printable

[2] Which often are again integrated in a single microchip.

feature size the wavelength has to be decreased further. This means entering the *extreme ultraviolet*[3] (EUV) wavelength regime.

The selection process of the next exposure wavelength was influenced by many factors: The availability of sources and suitable resists, but mainly by the limitations of multilayer mirrors (MLMs) [7, 8]. For the EUV wavelength range, transparent materials to fabricate lenses from do not exist and MLMs are used to bend and transport the light. Since MLMs only reflect efficiently within a narrow wavelength range their design needs to be strongly matched to the emission spectrum of a possible source. Ultimately, a consensus was reached on the next candidate wavelength of 13.5 nm, making use of Mo/Si MLMs [9]. A capable 13.5 nm source was found in the form of a CO_2-driven tin laser-produced plasma (LPP), making use of liquid droplet targets.

More than two decades of research preceded the application of EUV for commercial lithography. Especially demands on EUV-source power and reliability provided significant hurdles to overcome. In the meantime, smart patterning techniques allowed for a continued shrinking of IC elements using 193 nm exposure, reaching feature dimensions many times smaller than the wavelength [10]. Eventually *extreme-ultraviolet lithography* (EUVL) reached industrial maturity [11, 12] and is now in use by the semiconductor industry.

1.2. The extreme ultraviolet light source and pre-pulse

One of the primary requirements for any source is that it supplies enough power for the job at hand. Regarding EUV sources for lithography this aspect proved to be particularly challenging, with one of the main reasons being the limitations of MLMs. Although MLMs are relatively good normal-incidence reflectors in the EUV range, their peak efficiency does not exceed $\sim 70\%$ and their bandwidth is limited ($\sim 2\%$). This means that with every mirror in the exposure tool, and there are roughly 10 in current-day machines, a significant amount of EUV power is lost. Besides putting stringent requirements on power management in the exposure tool, it simply means the source needs to compensate these losses with a higher output to deliver enough EUV power to the photoresist. Out of several possible source techniques, laser-produced plasma (LPP) sources seemed most likely to be able to supply such power levels [11, 13], and out of a handful of possible source materials, tin showed the most promise [6]. The spectrum of highly ionized tin plasma of optimum density and temperature peaks close to 13.5 nm, strongly matching the high-reflectivity range obtainable with Mo/Si MLMs. Thus, the tin LPP was selected to serve as the next light source for EUVL.

Several LPP source architectures with varying target geometries were considered [7]. Evidently, debris generated by the laser-matter interaction proved to be a serious issue in LPP sources. To collect the EUV emission from the LPP and direct it towards the illuminator, an ellipsoidal mirror surrounds the LPP on the

[3] Although no hard definition exists, the extreme ultraviolet (EUV, sometimes abbreviated with XUV) regime typically refers to wavelengths ranging from approximately 120 nm down to 10 nm, and partly overlaps with the regime commonly referred to as soft X-rays.

laser-facing hemisphere. Mitigating contamination of this costly "collector" mirror and extending its lifetime is crucial to source operation. By using mass-limited *microdroplet* targets, as opposed to for instance planar or liquid-jet targets, debris is minimized to a great extent [14]. In the source a monodisperse stream of droplets is generated at a high repetition rate ranging from 40 kHz to 100 kHz and, to attain sufficient spacing between droplets, with a high velocity of 60 m s^{-1} to 120 m s^{-1}. Each droplet, with a typical diameter between 20 µm to 30 µm, provides a fresh LPP target with, in an ideal case, the exact amount of tin mass necessary for generating optimum plasma conditions in which as many tin ions as possible contribute to the desired EUV emission.

Even in the case of mass-limited droplet targets, additional debris mitigation methods are needed to extend the collector mirror lifetime. A hydrogen buffer gas is used to slow down highly energetic tin ions, and guide them away from the collector mirror. At the same time, dissociation of molecular hydrogen in the source vessel forms radicals that efficiently etch tin debris from the collector [15, 16]. Furthermore, a debris mitigation scheme has been presented that makes use of a magnetic field to guide away tin ions [17, 18].

The tin LPP is driven by a high-power (>20 kW) nanosecond CO_2 laser operating at a wavelength of 10.6 µm. The CO_2 laser was not only chosen because of practical and availability considerations, but also because of the high obtainable conversion efficiency (CE), i.e. the conversion of laser light into in-band EUV radiation at 13.5 nm within a 2% bandwidth, as compared to for example 1 µm-wavelength Nd:YAG lasers [20–22]. In early implementations of the source, the main CO_2 drive laser pulse directly irradiates the tin droplet. These sources provide a CE of approximately 1% and up to 30 W of relevant EUV power [16]. To enable high-volume manufacturing (HVM) in semiconductor fabrication plants the EUV output power had to be increased to $\sim$250 W. This was partly achieved by increasing CO_2 laser power, but a major stride forward was made by the introduction of the *pre-pulse* [16], a pulse preceding the *main-pulse* with the purpose of preparing a more optimal tin target from the initial droplet. Implementation of the pre-pulse enabled an increase in CE of several percent and thereby a power scaling to the required 250 W and beyond [14, 23].

Early mentioning of a pre-pulse for the purposes of increased CE refers to the generation of a pre-plasma on a nanosecond timescale [24–26], a distinct topic still actively studied today [27, 28]. However, the now established idea is to employ a pre-pulse to induce a hydrodynamic expansion of the droplet on a microsecond timescale [29, 30]. The motivation for this expansion is the mismatch between the optimal density and length scale of a CO_2-driven plasma and that of the initial droplet [16, 21, 31]. Efficient absorption of CO_2 laser light and, likewise, efficient EUV emission, require a plasma size of several 100 µm, which is also the typical main-pulse diameter at the laser-target interaction point [16]. Therefore, to make efficient use of the available tin "fuel" in the droplet and the available laser energy, expansion and redistribution of the material through pre-pulse impact is advantageous. Achieving optimal CE now mainly comprises optimization of the tin target.

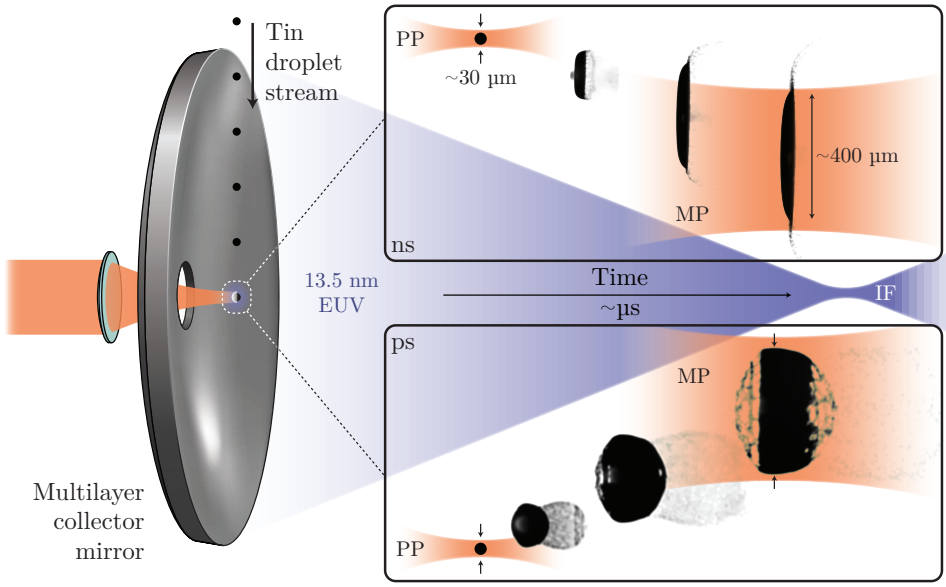

Figure 1.1: Illustration of the droplet-based EUV source operation principle with a pre-pulse (PP) plus main-pulse (MP) irradiation scheme. Each droplet in a droplet stream is impacted by a pre-pulse to initiate expansion of the $\sim 30\,\mu m$ diameter droplet to a target of several $100\,\mu m$ in diameter. The top panel shows the typical sheet-type deformation occurring after impact of a ns-duration pre-pulse and the lower panel the spherical bubble-like expansion following impact of a ps-duration pre-pulse. In both cases a typical desired target size is attained after several µs, at which instance the target is irradiated by a more energetic main-pulse. This generates a highly ionized tin plasma that emits the relevant 13.5 nm EUV radiation. The EUV emission is collected by the ellipsoidal multilayer-coated "collector" mirror and focused at the intermediate focus (IF) which serves as an entry point into the illuminator part of the wafer stepper machine. Note that the displacement of the deforming targets indicates time, not space, and serves visual clarity. In reality the ns-type target is propelled (to $\sim 100\,m\,s^{-1}$) and will displace sideways, whereas a center-of-mass propulsion is absent for the ps case. Both targets would retain the initial downward velocity of the droplet. Droplet and target dimensions indicated in the ns panel also apply to the ps panel. Illustration is adapted from Ref. [19].

The character of the induced expansion dynamics strongly depends on the choice of pre-pulse parameters. Two main types of deformation have been identified and employed in industrial sources capable of supplying sufficient power for high-volume manufacturing. Figure 1.1 illustrates the operation principle of the EUV source and depicts the typical deformation for these two types of pre-pulses. Impact of a nanosecond-duration pulse ($\gtrsim 10\,ns$) on the droplet propels it and induces an expansion of the droplet into a thinning sheet [32, 33], resulting in what is often referred to as a "disk" target. Nanosecond pre-pulses are currently generated using the same CO_2 laser that outputs the main-pulse [16]. Using a separate 1 µm-wavelength source to generate the ns-pre-pulse instead [34, 35], might provide several engineering advantages and leaves maximal CO_2-power available for the main-pulse. Impact of shorter picosecond- or femtosecond-duration pulses leads to a spherical

bubble-like expansion and targets referred to as “dome” or “cloud” targets. These targets showed much promise for obtaining high CE, likely due to their volumetric nature, but provide additional debris mitigation challenges due to fast (neutral) debris resulting from spallation [36, 37]. In the ps-pre-pulse case, using a separate laser system, typically also with a 1 µm wavelength [34], is the only option. For both nanosecond- and picosecond-pre-pulse cases CE values exceeding 5% have been reached [16, 34].

With many details of pre-pulse-related physics still unclear, these promising results serve as a motivation and backdrop for in-depth scientific investigation of the pre-pulse concept and target preparation in general. Ideally, one would design the ideal target mass distribution for interaction with the main-pulse in a ‘bottom up’ approach. It is generally agreed upon that such a target would be a low-density (vapor) target with a diameter of several 100 µm, and without steep density gradients to prevent reflection of CO_2 main-pulse light. Nevertheless, a detailed target design has so far not been presented and would also need to include debris and stability considerations. Regardless, a comprehensive understanding of the droplet dynamics following pre-pulse impact—and identifying all possible outcomes—is of great value to improved target design, and necessary to uncover which targets can eventually be generated, possibly making use of more complex multi-pulse schemes.

1.3. Timescales of laser-induced droplet deformation

The transformation process of deforming a micron-sized tin droplet into a target using laser pulses involves a broad range of physical processes and disciplines. Paramount to the outcome of the interaction between a laser pulse and a droplet is the order of timescales involved [38] which are accordingly introduced here.

The electron-ion relaxation time $\tau_{\text{e-i}}$ governs the exchange of energy or temperature between the free electrons and ions lasting $\sim 10\,\text{ps}$ [39], and plays an important role in the absorption process of the laser pulse. A plasma-hydrodynamic timescale $\tau_{\text{h}} \sim 100\,\text{ps}$ [38, 40] follows from the distance between the droplet and critical surfaces, and the speed of sound in the laser-produced plasma, i.e. the typical velocity of the ablation flow. Ablation using laser pulses similar or longer in duration than this timescale will enter a quasi-stationary ablation regime [40]. The liquid acoustic timescale $\tau_{\text{a}} = R_0/c \sim 10\,\text{ns}$ is that at which acoustic waves traverse the droplet with radius R_0 at the speed of sound c. The inertial timescale $\tau_{\text{i}} \sim U_{\text{rel}}/R_0 \sim 10-100\,\text{ns}$ sets the time it takes for the droplet to lose its initial shape and deform into the distinct expansion geometry. Universally this relevant velocity $U_{\text{rel}} = \dot{R}_0$, with $\dot{R}_0$ the initial radial expansion rate, but correlated velocities like the center-of-mass propulsion U can be used based on the type of induced deformation. Finally, the capillary timescale $\tau_{\text{c}} = \sqrt{\rho R_0^3/\sigma} \sim 10\,\mu\text{s}$, with liquid density ρ and surface tension σ, sets the time at which liquid surfaces decelerate and retract. In general we can thus order the timescales as follows:

$$\tau_{\text{e-i}} \ll \tau_{\text{h}} < \tau_{\text{a}} < \tau_{\text{i}} < \tau_{\text{c}}. \tag{1.2}$$

Here, I consciously refrain from using $\ll$ for most separations in this order, as in some extreme cases a subset of these timescales will approach each other closely as a function of laser energy and pulse duration, and R_0. A crux of this thesis is that the position of the pulse duration τ_{p}, or more specifically the timescale of changes in laser intensity, within this timescale arrangement is arguably the most important factor determining the fluid-dynamic deformation of the droplet. Embracing a broad perspective, relevant (pre-)pulse durations can be positioned anywhere below the capillary timescale, i.e. $\tau_{\text{p}} < \tau_{\text{c}}$.

1.4. Outline of this thesis

This thesis investigates the interaction between laser pulses and metallic microdroplets, and the ensuing dynamics, with a specific focus on exploiting the tunability of laser pulses and pulse sequences.

In **Chapter two**, we present the laser system that made this possible. The system combines arbitrary pulse shaping, enabled by the use of high-speed electro-optic modulators, with amplification to pulse energies of several hundred millijoules. Each following chapter presents experimental work in which we employed this system and which profited from its unique capabilities.

In **Chapter three**, we study the fluid dynamic deformation of tin microdroplets resulting from impact of short pulses. If intense enough, these pulses will launch shock waves into the droplet interior that subsequently induce cavitation and spallation. We quantify the resulting deformation velocities for a large range of laser pulse energies and droplet sizes by combining data from multiple experiments.

Chapter four presents a study on the laser-induced droplet deformation for pulses of varying duration and Gaussian and square temporal shapes. The range of pulse durations studied bridges the transition from shock-wave-dominated deformation, i.e. cavitation and spallation, as presented in Chap. 3 to sheet-type expansion. We quantitatively study the pulse-duration dependence of the center-of-mass propulsion, and expansion and spall-debris velocities.

In **Chapter five**, we study the deformation following impact of two pulses of 0.4 ns each. The time delay between the two pulses is scanned from 1 ns to 100 ns and repeated for various droplet sizes. These scans reveal a reduction of the spall velocity which takes place at increasing interpulse spacing for increasing droplet size.

In **Chapter six**, we measure the time-resolved reflection from the droplet to study the moment of plasma onset and the plasma-formation fluence threshold.

In **Chapter seven**, we study the mass distribution of a stretching sheet of liquid tin formed after ns-pre-pulse impact by using an auxiliary, low-intensity *vaporization pulse* (VP). This VP gradually vaporizes the sheet enabling an investigation of the sheet thickness and mass.

A supplementary **shadowgram gallery** presents a selection of captivating and intriguing shadowgrams that did not make it into any of the main chapters.

1.5. Experimental setup

All experiments described in this thesis have been performed making use of the same microdroplet-generator setup, including shadowgraphy systems. Although many parts of the setup have undergone changes over the years, and even the core vacuum vessel has been upgraded, the basis of the experimental arrangement has remained the same. This section describes the main operation principles of the experimental apparatus and means to complement the experiments and methods sections of the independent chapters which describe more topic-specific aspects of each experiment.

Although I have enthusiastically performed experiments with this setup, my role in the design, build-up, and maintenance has been minor. I would therefore, here, like to acknowledge the exemplary efforts in this regard of my direct research colleagues, the involved technicians, and the people at the mechanical design and engineering departments of AMOLF & ARCNL. The following strongly borrows from the detailed report of this setup by D. Kurilovich in Ref. [19] to which we refer the reader for additional information.

The experimental setup supplies a stable stream of tin microdroplets in a high-vacuum environment ($\sim 10^{-7}$ mbar) with excellent (optical) access from many ports. Figure 1.2 shows side- and top-view cross-section illustrations of the setup. The microdroplet generator, consisting of a tank containing the (liquid) tin and a nozzle assembly, is positioned on top of the vacuum vessel with a port aligner to control its angle. In preparation of an experiment, the tank is filled with high-purity (99.995%) tin, pumped down through a connected vacuum line, and together with a nozzle heater heated to approximately 260 °C, above the melting point of tin (232 °C). The tank is subsequently pressurized using argon gas, typically to a pressure of 10.5 mbar, which starts the stream of liquid tin into the vessel at a velocity of approximately $10\,\mathrm{m\,s^{-1}}$. Attached to the bottom of the vessel is an assembly connected to the vacuum pumps and a tin catcher. The tin catcher collects the tin stream and is also heated to prevent solidification.

Controlled breakup of the tin stream into equal-sized droplets is achieved by driving a piezo element integrated in the nozzle. The frequency of the piezo-driving signal, the tank pressure, and the diameter of the nozzle orifice together determine the size of the droplets. The frequency f of the piezo-driving signal provides the best control over the droplet diameter d and can be easily changed during streaming operation. Furthermore, the relation $d \propto f^{-1/3}$ follows from a straightforward mass-conservation argument. Therefore, with a single calibration measurement at fixed nozzle orifice size and tank pressure, $d(f)$ is known and the droplet size can be accurately scanned as is done for example in Chap. 5. Values for f range from 5 kHz to 100 kHz yielding available droplet diameters between 20 µm and 60 µm with a typical uncertainty of ± 1 µm. The tank pressure can also be changed relatively easily during streaming, but has limited stable operation range and a smaller effect on the droplet size. Additionally, it also alters the stream velocity which affects tin consumption and trigger timings. The combination of stream velocity and operation frequency sets the inter-droplet spacing.

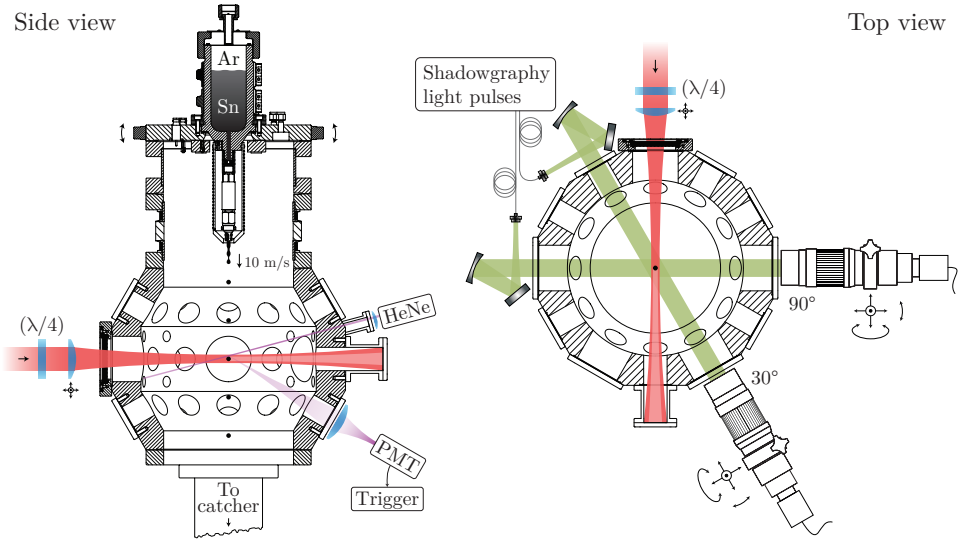

Figure 1.2: Illustrations of the droplet-generator experimental setup. Left and right images show a side- and top-view cross section, respectively.

On their way down the droplets pass through a horizontally-aligned light sheet produced with a CW helium-neon laser. The light scattered by the droplets as they pass this sheet is detected by a photo-multiplier tube (PMT) and the kHz-frequency signal is down-converted to 10 Hz to serve as a trigger for the acquisition, including multiple oscilloscopes and cameras, and laser systems. The light sheet is typically positioned 2–3 mm above the center of the vacuum vessel to leave 200–300 µs travel time to the laser-droplet-interaction point. The minimum required travel time is determined by the pump-pulse duration (fluorescence lifetime) of the laser systems used. This may be avoided by using an alternate trigger scheme in which the laser pump is delayed by a full cycle, making the system ready for instant firing on the next trigger pulse. Currently, no significant instabilities arise from several ~ 100 µs travel time between droplet detection and laser-droplet interaction and such an implementation is not needed. Nevertheless, it might become necessary at increased stream velocities.

The pre-pulse laser beam is generally focused down to a Gaussian spot (ranging 45 µm to 130 µm FWHM depending on the study) in the center of the chamber using a single lens. This lens is mounted on a xyz-translation assembly which is used for the final alignment of the focal spot onto the droplet, performed by observing the target tilt and center-of-mass velocity [41]. Furthermore, a quarter waveplate is typically inserted before the lens to modify the polarization of the laser beam into circular, preserving cylindrical symmetry in absorption on the droplet surface. Exceptions to the above are experiment A in Chap. 3, in which a flat-top spatial profile was imaged onto the droplet using a more complex high-NA

arrangement and the linear polarization of the laser beam was retained, and the combination of vaporization pulse and pre-pulse in Chap. 7, which also required an imaging arrangement with beam-combining beam-splitter cubes. In all cases, the energy of the laser beam is set by means of a waveplate-polarizer combination (not shown in Fig. 1.2). Furthermore, from a camera recording of the focal spot and known droplet diameter, we determine the geometric overlap between the focal spot and the droplet. This overlap factor is used to determine the laser pulse energy fraction impinging on the droplet E_{od}, an important parameter for laser-droplet interaction [32].

The dynamics of the irradiated targets are captured by stroboscopic shadowgraphy imaging systems [32, 33, 37]. These systems combine incoherent pulsed backlight-illumination at 560 nm with CCD cameras (AVT Manta G-145B NIR) coupled to long-distance microscopes (K2 Distamax), yielding a spatial resolution of approximately 5 µm. Fluorescence from a 532-nm-pumped dye cell provides the backlighting shadowgraphy pulses with a spectral bandwidth of 12 nm (FWHM) and a pulse duration of 5 ns (FWHM, setting the temporal resolution), which are delivered to the setup through optical fibers. The shadowgraphy systems simultaneously provide front- and side-view images of the tin targets, along 30° and 90° angles with respect to the laser beam propagation direction, respectively. By delaying the back-lighting source with respect to the focused pre-pulse we record the deformation of the droplet following laser impact in a stroboscopic fashion. Per shadowgraphy time delay, multiple (typically 10) frames are recorded to allow for post-filtering on optimal laser-to-droplet alignment.

Chapter 2

An Nd:YAG Laser System With Arbitrary Sub-Nanosecond Pulse Shaping

It's not particularly silly, is it? I mean, the right leg isn't silly at all and the left leg merely does a forward aerial half turn every alternate step.

John Cleese

We report on a laser system capable of generating high-energy (>270 mJ) temporally shaped pulses at 1064 nm with 0.43 ns shaping resolution. The pulses are generated by modulation of a continuous-wave seed laser, and subsequent amplification by a dual-stage grazing-incidence Nd:YVO_4 'bounce' amplifier and an Nd:YAG power amplifier (all quasi-continuous diode-pumped). The system produces pulses with a high-quality top-hat spatial beam profile, up to 0.6 GW of peak power and 44 W of average power, a power stability of 0.22% rms, and fully programmable complex temporal shapes.

Parts of this chapter have been published in Optics Letters **42**, 2758 (2017) [42].

2.1. Introduction

Laser pulses are a powerful tool for inducing a large diversity of dynamical phenomena in matter. Temporal shaping of laser pulses and pulse sequences has been used in a wide variety of fields and applications to control such dynamics. Shaping of femtosecond and picosecond pulses is generally performed in the spectral domain [43] using spatial light modulators or acousto-optic programmable dispersive filters; it is often aimed towards coherent control and photochemistry [43–45]. Shaping on the nanosecond to millisecond timescales is generally done by acousto- or electro-optic modulation and is mostly aimed towards ablation mechanics in, for example, micromachining [46, 47]. Other fields employing temporal pulse shaping based on varying methods of pulse combining include fusion ignition [48], x-ray lasers [49], and laser-produced plasma (LPP) extreme-ultraviolet (EUV) sources [50].

In the context of droplet-based EUV sources we aim to improve control over laser-induced droplet deformation for target preparation [32, 37], and over laser-produced plasmas and specifically their EUV emission characteristics. Such plasmas display rich dynamics on the nanosecond timescale [51], and the ability to control plasma parameters by optical means requires a combination of high-energy laser pulses with GHz-bandwidth pulse-shaping capabilities. Yet this intermediate regime of pulse shaping on (sub-)nanosecond timescales, especially in combination with high-energy pulses, has to the best of our knowledge remained largely unexplored. Passive shaping methods based on coherent or incoherent pulse combining have been used to generate complex pulse shapes in this parameter range. Yet these methods are inflexible as they require precise adjustment of an array of different optical paths, and are intended to produce only one or a few specific pulse shapes [52, 53].

The development of fast, compact, integrated electro-optic modulators (EOM) has made arbitrary temporal shaping at GHz speed accessible [54, 55] and has proven capable of bridging the gap between spectral-domain shaping of ultrafast pulses and temporal modulation by acousto-optic modulators (AOM) and Pockels cells. However, the penalty for their fast modulation speed is a low average power threshold, usually in the mW regime. Therefore, to apply temporal shaping on the 0.1 ns to 10 ns timescale to high-energy laser pulses, amplification after shaping is necessary. Several systems have already been developed aimed at high average power [54, 56] and peak powers reaching tens of kW.

In this Chapter we present a laser system delivering arbitrary shaped pulses with 0.43 ns resolution and pulse energies ranging between 270 and 440 mJ at 1064 nm wavelength and 100 Hz repetition rate. The highest achieved peak power is 0.6 GW, at an average power of 27 W and pulse duration of 0.43 ns. The system is based on a modulated continuous-wave (CW) laser which seeds a dual-stage grazing-incidence amplifier utilizing Nd:YVO_4 crystals pumped at 880 nm [57]. Further amplification is obtained by using a quasi-continuous-wave (QCW) diode-pumped Nd:YAG power amplifier. The laser output is characterized and several examples of pulse shapes are presented showing the complex pulse-shaping capabilities.

2.2. System description

Figure 2.1 shows a schematic of the full laser system in which the pulse shaping, pre-amplifier, and power-amplification stages are indicated by their respective frames. The pulse-shaping section is fully fiber coupled (polarization maintaining) and starts with a CW-fiber laser (NKT Koheras BoostiK Y10) delivering 2 Watts of continuous laser light at 1064 nm. This light is first gated by an AOM (Gooch & Housego Fiber-Q, operating at a 150 MHz carrier frequency), resulting in square pulses. The function of the AOM is to deliver high-contrast modulation (50 dB), minimizing parasitic seed light, and simultaneously limit the average input power to two high-speed EOMs following it. Each EOM (Jenoptik AM 1064, amplitude modulator, 200 ps rise time, 30 dB dynamic range) is individually driven by one of the two channels of a 2.3 Gs/s arbitrary waveform generator (AWG) (Tabor Electronics WX2182C). Working in tandem they create the final pulse shape to be amplified. A second EOM was necessary to improve contrast by effectively blocking light leaking through the first EOM and to improve pulse shaping at the rising edge of a pulse, where the gain saturation effect present in the amplifiers is the strongest.

The shaped pulses are initially amplified by a dual-stage triple-pass grazing-incidence 'bounce' pre-amplifier, containing two Nd:YVO_4 crystals (a-cut) with doping percentages of 1% and 0.5% and dimensions of 5 x 2 x 20 mm and 6 x 4 x 20 mm respectively. The crystals are optically pumped from the side by QCW diode arrays (Dilas MY-Series), thermally tuned to around 50° C to emit at the upper lasing level of Nd:YVO_4 around 880 nm, delivering approximately 240 W of optical pump power during 110 µs long pulses. The beam enters the Nd:YVO_4 crystals through the side facet and undergoes total internal reflection on the pumped surface of the crystal, the 'bounce'. This geometry allows for strong pumping and provides homogeneous amplification of the seed preventing spatial distortion of the beam profile. Note that the side facets of the crystal have a small angle of 5° to prevent parasitic lasing in the crystal. Furthermore, optical isolators and a spatial filter are placed between the passes to block back reflections, keeping amplified spontaneous emission (ASE) to a minimum, and preventing parasitic self-lasing of the amplifier. The available seed energy depends on chosen pulse duration and (pre-compensated) pulse shape. Given the 2 W output from the CW laser and assuming a specified insertion loss of the three modulators together of 12 dB, an upper limit for the energy of seed pulses of known shape can be determined. For example, a 500 ns square seed pulse leads to an estimated seed energy of 63 nJ which is amplified to 2.84 mJ by the total of three amplification passes. This corresponds to a saturated gain of 46.5 dB for the full bounce amplifier. A 0.5 ns FWHM Gaussian pulse is estimated to have an energy of 30 pJ and is amplified to 0.4 mJ at a gain of 71 dB.

After the bounce amplifier the beam is further amplified in a power amplification stage, which is separated from the pre-amplifier by a Pockels cell acting as a temporal gate to suppress ASE. In this power amplifier we make use of a QCW diode-pumped Nd:YAG module (Northrop Grumman REA6308) containing a 6.35 mm diameter Nd:YAG rod 146 mm in length. Nd:YAG is used here as a gain medium instead of Nd:YVO_4 because of its higher energy storage capability, albeit

providing less gain than Nd:YVO_4 [58]. Before passing through the module the Gaussian beam is expanded slightly to 1.8 mm FWHM and clipped by a 2.4 mm hard aperture. This controlled clipping of the beam prevents further unwanted clipping of the beam at the edges of the Nd:YAG rod and allows for a better control of the filling fraction of the rod. An initial relay telescope (f = 200 mm and f = 400 mm), with a weak spatial filter (2.5 mm diameter) at the focus, images the aperture plane near the end face of the module with 2 times magnification, leading to a 4.8 mm beam size in the module. Increasing the filling fraction of the Nd:YAG rod will evidently result in a higher output energy, but also to beam distortion due to the 5-fold side pumping geometry utilized in the module that gives an inhomogeneous gain profile near the outer edge. A 1:1 relay telescope, with a vacuum tube at the focus to prevent breakdown in air, images the previous image plane onto the end mirror which reflects the beam for the second pass. Between the two passes through the module the polarization is rotated by a Faraday rotator. In combination with relay imaging this neutralizes the effects of thermal birefringence in the Nd:YAG crystal rod [59]. A thin-film polarizer (TFP) is used to couple out the beam, while an additional TFP has been inserted to increase isolation and prevent parasitic lasing. The temperature of the Nd:YAG rod influences its pump absorption, which provides some control over the radial gain profile in the rod. This profile is such that the gain increases towards the edges of the rod. By seeding with a clipped Gaussian input shape and controlling both the rod surface temperature and pump power, we can optimize the output beam profile to obtain a high quality flat-top as can be seen in Fig. 2.2(a). We drive the module with 250 µs pulses at 110 A and operate the system at a cooling temperature of 20° C. Depending on input pulse shape and energy we achieve a gain between 23.9 and 30.6 dB, corresponding to output pulse energies between 270 and 440 mJ. The limiting factor in the achievable gain of the present double-pass amplifier configuration is the occurrence of self-lasing at higher pump currents. A route towards further power scaling can be the implementation of an additional double-pass amplifier stage, with increased rod diameter. Since the gain bandwidths of Nd:YVO_4 and Nd:YAG are not identical, we adjust the wavelength of the CW source at sub-nm scale such that the overall output energy is optimized.

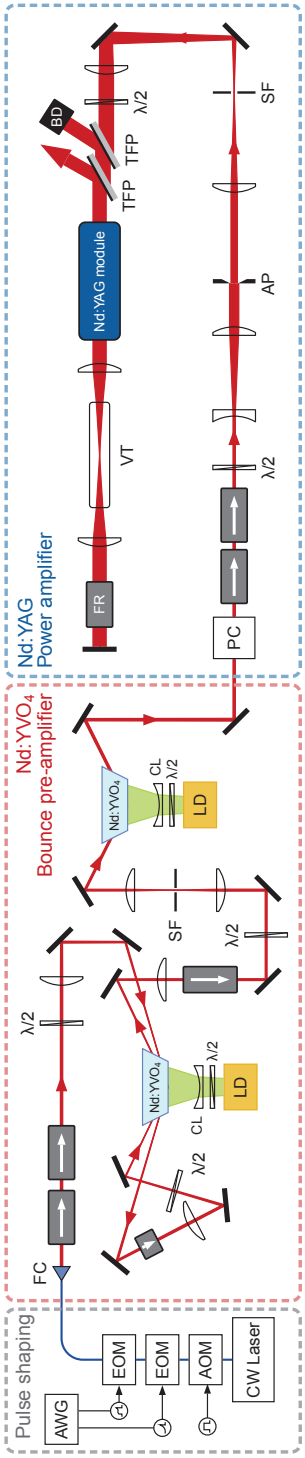

Figure 2.1: Schematic of the all-fiber pulse-shaping chain, the dual-stage Nd:YVO_4 bounce pre-amplifier, and Nd:YAG power amplifier (AOM: acousto-optic modulator, EOM: electro-optic modulator, AWG: arbitrary waveform generator, FC: Fiber collimator, ⇒: Isolator, λ/2: Half-wave plate, CL: Cylindrical lens, LD: Laser diode, SF: Spatial filter, PC: Pockels cell, AP: Aperture, TFP: Thin-film polarizer, VT: Vacuum tube, FR: Faraday rotator, BD: Beam dump).

2.3. System characterisation

Figure 2.2(b) shows the measured output stability of the complete all-diode-pumped system. A power stability of 0.22% rms over 24 hours was obtained for the pulse shown in Fig. 2.3(a) with 437 mJ output energy. The long-term stability is limited to 0.22% rms by the cooling cycle (≈1.2 min) of the Nd:YAG module in the power amplifier as can be seen from the zoom-in. By subtracting this oscillation we find a short-term power stability of 0.11% rms.

The advanced temporal shaping capabilities of our laser system are demonstrated in Fig. 2.3. Figure 2.3(a) shows the measured pulse shape produced by the amplifiers for a square 500 ns input pulse, showing gain depletion from the amplifiers within only a few ns. As a result, the output pulse is asymmetric with a duration reduced to only 1.2 ns FWHM. With active shaping, we achieve a minimum pulse duration of 0.43 ns FWHM, as shown in Fig. 2.3(b). Figures 2.3(c-h) display several pulse shapes over a time span of 10 ns, demonstrating the fast pulse-shaping capabilities. More specifically, Fig. 2.3(c) shows a pulse train demonstrating the shaping resolution obtained by alternating consecutive sample points in the AWG waveform. The average distance between the peaks and valleys is found to be 0.43 ns. This, as well as the minimum pulse length of 0.43 ns, corresponds very accurately to the sample rate of the AWG of 2.3 GHz. Furthermore, as shown in Fig. 2.3(j), the system can generate pulses up to 1 µs (limited by the opening time of the Pockels cell), spanning four orders of magnitude in pulse length. The temporal intensity of the 1 µs pulse remains very constant; it deviates from a perfect flat intensity profile by just 2.9% rms over the full pulse duration. For shorter square pulses, such as the 20 ns pulse shown in Fig. 2.3(i), we achieved deviations from a perfect flat temporal profile of only 1.6% rms. To illustrate the level of suppression necessary to compensate for temporal distortion we have added the corresponding waveforms applied to the EOMs for this case.

In the present configuration, the achievable output energy from the amplifier system exhibits a significant dependence on the target pulse shape. An example is given in Fig. 2.4, which shows the measured pulse energy for pulses with a square intensity profile of different duration. A maximum output energy of 400 mJ is found at a pulse duration of 5 ns. The observed energy increase for short pulses is readily explained by the increasing seed energy that is available when the pulse becomes longer. To understand the decrease for pulse durations above 5 ns, we modeled the gain dynamics in a double-pass amplifier [60] for the case of square output pulses of different durations. The input pulses were approximated by an exponential shape (increasing in time) with energies equal to the measured values before the first pass of the Nd:YAG module. Although the assumed single exponential input pulse shape is not fully accurate, the results explain the trend in energy accurately. The time at which the drop in energy occurs corresponds to the round-trip time τ_r of a light pulse traveling between the two passes through the power amplifier, in our case approximately 6.5 ns. For pulse durations longer than 6.5 ns, the leading edge of the pulse will have traversed the Nd:YAG rod twice before the trailing edge has completed the first pass. This effect causes gain stripping for parts of

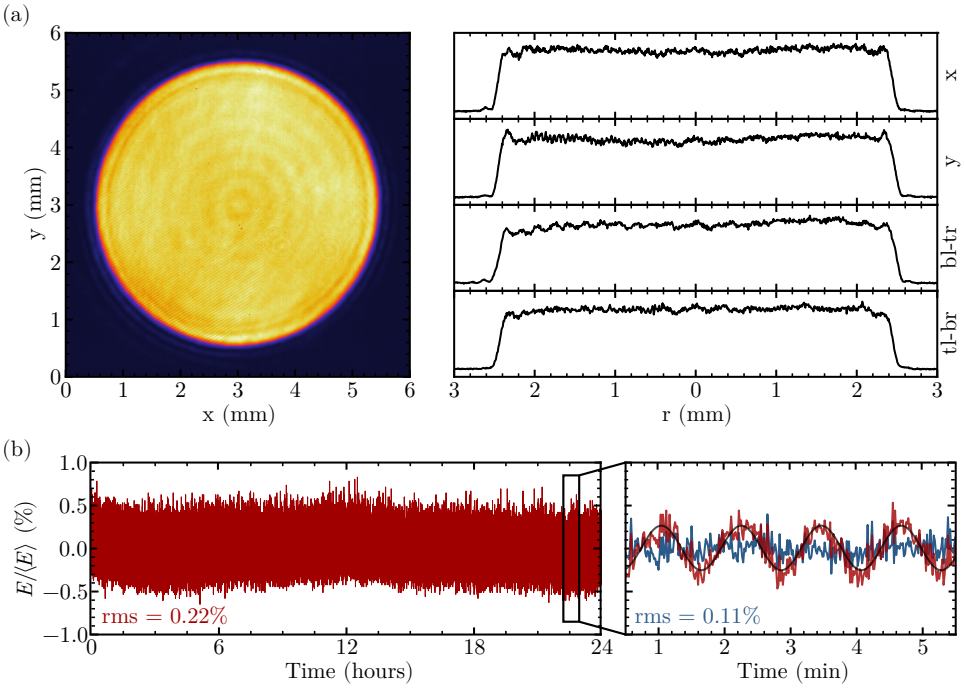

Figure 2.2: (a) Near field beam profile of the amplified pulses measured with 1:1 relay imaging at the output of the system. Horizontal, vertical and diagonal cross sections (from bottom left to top right and top left to bottom right) are included. Diffraction rings caused by spatial filtering before amplification in the power amplifier are visible as well as a weak cross geometry due to remaining thermally induced birefringence in the Nd:YAG rod. Small scale diagonal fringes present in the image are an artifact from interference in the CCD camera (they are mostly visible in the cross sections as small scale ripples). (b) Long (24 hours) and short (5 min) time duration stability of the output pulse energy.

the pulse $> 6.5\,\mathrm{ns}$, and leads to a lower overall gain and reduced energy extraction efficiency for longer pulses. More information on this phenomena and the performed simulations is given in Sec. 2.A.1. The data points for pulse lengths $< \tau_\mathrm{r}$ (where pulse shape has no influence) were fitted to obtain an effective saturation fluence for this amplification stage of $0.83\,\mathrm{J/cm^2}$. With a higher available seed intensity the effects of gain stripping due to the described pulse overlap can be averted by fully saturating the power-amplifier. At the current repetition rate of 100 Hz, and in combination with the AOM as a first temporal gating device, the average input power to the EOMs is still several orders of magnitude below their specified damage threshold. Therefore, there is still room to increase the available seed pulse energy to the amplifiers by using a more intense seed laser, such as a pulsed diode source [56]. The round-trip time of the double pass through the first crystal of the bounce amplifier is approximately 3 ns. However, any significant drop in output energy from the bounce amplifier due to pulse overlap was absent. This is as expected as there is no significant energy extraction in this amplification stage.

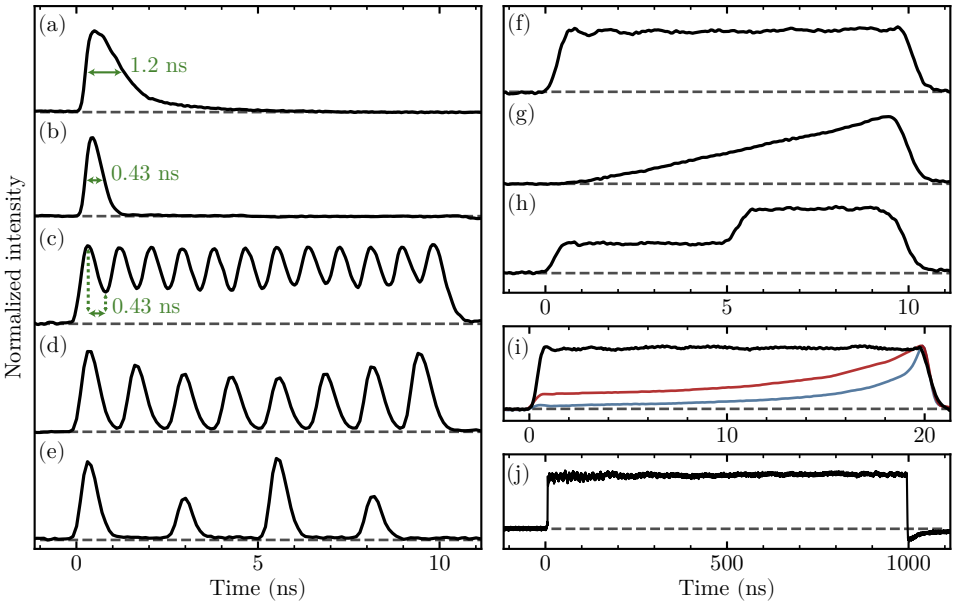

Figure 2.3: Measured temporal pulse shapes demonstrating the shaping capabilities of the laser system. Including (a) the response of the system when given a flat-intensity input pulse, (b) the shortest pulse obtained using active shaping with a FWHM of 0.43 ns, (c-e) varying pulse trains, (f) a square 10 ns pulse, (g) a linear rising slope, (h) a 2-step flat pulse, (i) a square 20 ns pulse, and (j) a 1 µs square pulse. In (i) the blue and red curves are the waveforms applied to the first and second EOM respectively. The dip at the end of the 1 µs pulse is attributed to the photodiode response. All pulses are measured using a >15 GHz photodiode positioned at a focus and a 4 GHz oscilloscope. All traces shown are averaged over 16 pulses.

The strong gain dynamics require significant pre-shaping of the input pulse shape to obtain a desired output shape. In a first implementation these shapes have been manually programmed and optimized. As a first step towards automated optimization of a target output shape, we have implemented a feedback algorithm that optimizes towards basic pulse shapes. This algorithm uses a straightforward approach, optimizing temporal sections of the pulse from early to later times while setting the intensity of each section relative to preceding sections, under the assumption that a each point in the intensity profile only influences later parts of the pulse. Although, as already discussed above, this assumption is not fully justified in a double-pass amplifier, the approach works well when sufficient dynamic range is used and gain depletion is avoided before the end of the pulse is reached. In addition to setting specific pulse shapes, we envision the use of evolutionary algorithms to enable automatic optimization to any complex shape, using specific experimental parameters to define a fitness function [47, 61].

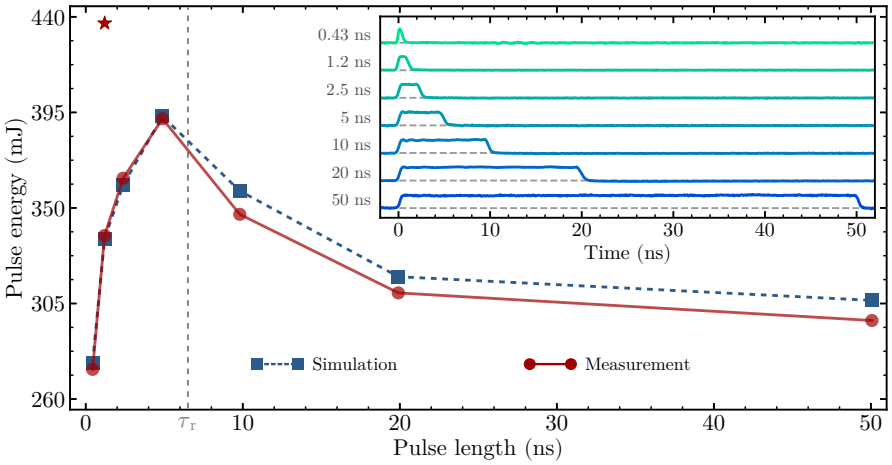

Figure 2.4: Measured and simulated pulse energy as a function of pulse length for output pulses with a square intensity profile. The traces of the corresponding measured pulses are shown in the inset. The star-marked data point corresponds to the saturated response of the system as shown in Figure 2.3(a). For pulse lengths above 50 ns the curve flattens out at approximately 300 mJ.

2.4. System conclusions & outlook

In this chapter we have presented a laser system that combines true arbitrary temporal intensity shaping of laser pulses with a resolution of 0.43 ns, pulse energies up to 437 mJ, an average power of 44 W, and peak powers up to 0.6 GW. The large dynamic range in shaping achieved by two EOMs ensures that we can always achieve a combination of accurate pulse shape and good energy extraction that reaches 30-40% of the stored energy. We achieve excellent beam quality and output stability independent of the produced pulse shape. Implementation of faster EOMs and driving electronics can further improve the shaping resolution. The addition of further amplifier stages, employing a larger diameter Nd:YAG rod and higher stored energy, will allow extension of this technology to pulse energies above the Joule level, and multi-GW peak powers. We believe that the ability to temporally tailor nanosecond pulses with the demonstrated temporal resolution and range makes this a versatile and valuable system for high-energy laser-matter interaction studies.

Comment on published target preparation method

In the published work [42], we speculated on using the temporal shaping ability of the system to create a metal vapor target for laser-produced plasma experiments, stating the following:

> A possible application that we envision involves temporal control over the vaporization of a metal target by an optimized laser pulse shape. The target can be heated up in a controlled way by adjusting the temporal pulse shape and pulse energy. In these conditions, the metal target adiabatically follows an equilibrium vaporization path through the phase diagram and avoids both super-heating and subsequent phase explosion, which are commonly observed for high-energy laser-matter interaction. This approach could lead to a slowly expanding gas target with a homogeneous density profile without significant generation of ions or nanoparticles, which would be a desirable starting point for laser-produced plasma experiments.

The ablation threshold work presented in Chap. 6 shows that currently we are not able to vaporize a complete liquid tin droplet using this laser system. In fact, for a 30 µm-diameter droplet, we estimate that a laser pulse of approximately 25 µs is needed to supply enough energy to the liquid to vaporize the droplet fully whilst staying below the plasma formation threshold. Such pulse durations are achievable with this laser system if the current pulse-duration-limiting Pockels cell is removed or exchanged with a different solution. Regardless, the high $\sim 50\,\mathrm{kHz}$ repetition rate and $\sim 80\,\mathrm{m\,s^{-1}}$ velocity of the droplets used in industrial EUV sources [14] limit the applicability of such a long ($\gtrsim 10\,\mu\mathrm{s}$) pulse tasked with vaporizing a full droplet. However, vaporizing a liquid sheet of tin with a thickness of only several tens of nanometers is very applicable as it can be done with ns-duration pulses as shown in Chapter 7.

2.5. Work made possible by this laser system

The unique pulse-shaping capabilities of the system presented in this chapter have proven to be extremely valuable for the research performed at the Advanced Research Center for Nanolithography. Not only within the context of droplet deformation and EUV-source target preparation, which are the main topics of this thesis, but also for spectroscopic investigations of laser-produced plasmas [62, 63] and studies into the achievable conversion efficiency of laser light into EUV light using a 1064 nm wavelength [22, 64, 65].

Furthermore, the chapters in this thesis are by themselves a testimony to the broad applicability of this laser system. Chapters 3 and 5 are made possible by the sub-nanosecond shaping resolution of the system, being able to generate pulses with a minimum duration of 0.43 ns. Furthermore, Chapter 5 specifically makes use of the ability to fairly effortlessly make and tune colinear pulse pairs in a completely digitally controlled manner. In Chapter 4 we make use of the fine arbitrary pulse-shaping capability of the system, comparing droplet deformation resulting from

impact of Gaussian and square shaped pulses of different durations. The basic (and possibly underrated) ability to make square constant-intensity pulses (thereby stepping away from the standard but not particularly optimal Gaussian shape) and scan their duration has also enabled the works presented in Chapters 6 and 7. Lastly, the high achievable pulse energy and flat-top spatial profile were specifically essential to the work presented in Chapters 3 and 7, respectively.

Appendix

2.A. Temporal pulse distortion by gain saturation

As a laser pulse travels trough a gain medium, like the Nd:YVO_4 or Nd:YAG crystals used in the system presented in this chapter, it extracts the energy stored in the medium through stimulated emission. This leads to an amplification of the laser pulse through space and time. The amplification factor, or gain, depends on the energy of the laser pulse and the amount of stored energy in the gain medium. With increasing input pulse energy, the amount of energy extracted from the medium will also increase and approach the total initial amount of stored energy. This prevents any further amplification of the laser pulse, and the gain will *saturate*. Often, laser amplifiers operate in this saturation regime, where as much of the stored energy is extracted as possible. This is of course desired from an efficiency point of view and also increases operational stability. However, it often leads to a significant *temporal distortion* of the laser pulse when saturation occurs during the pulse amplification process.

In 1963 Lee M. Frantz and John S. Nodvik succesfully described one-dimensional pulse propagation through a laser amplifier [66], starting their derivation from the rate equations that describe the absorption and stimulated emission of photons by the medium and the corresponding transfer of atom between the excited and ground states. The resulting *Frantz-Nodvik equations* describe the amplification process for any arbitrary distribution of photon density over time t in the input laser pulse, $n_0(t)$ and arbitrary initial distribution of inverted population $\Delta_0(x)$ along the propagation distance x through the gain medium. The Franz-Nodvik equations can be written as

$$n(x,t) = \frac{n_0(t - x/c)}{1 - (1 - S)S_-}, \tag{2.1}$$

$$\Delta(x,t) = \frac{\Delta_0(x)S}{S_+ + S - 1}, \tag{2.2}$$

with the terms

$$S(x) = \exp\left(-\sigma \int_0^x \Delta_0(x')dx'\right), \tag{2.3}$$

$$S_{\pm}(x,t) = \exp\left(\pm\gamma\sigma c \int_{-\infty}^{t-x/c} n_0(t')dt'\right), \tag{2.4}$$

where σ is the absorption cross section of the resonant transition and c the speed of light. The factor γ accounts for the reduction in population inversion on emission of a single photon [58]. For a four-level system $\gamma = 1$ and for a three-level system in the absence of degeneracy $\gamma = 2$ (as originally used by Frantz and Nodvik [66]). Using equation 2.1 we can compute[1] the full amplification process and obtain the output pulse energy and shape.

The integrals in terms 2.3 and 2.4 lead to interesting relations between the input pulse and the resulting output pulse after amplification. If we consider a gain medium with a finite length L we can derive the temporal pulse shape at any point in space $x \geq L$, i.e. after exiting the medium. Let us for generality consider $x = \infty$. Then, since the photons in the input pulse defined at time t reach ∞ at time $t = t + \infty/c$, we obtain for the output photon density

$$n_\infty(t) = n(\infty, t + \infty/c) = \frac{n_0(t)}{1 - [1 - \exp(-\sigma\Delta_{\text{tot}})]S_-(\infty, t + \infty/c)}, \tag{2.5}$$

with $\Delta_{\text{tot}} = \int_0^\infty \Delta_0(x')dx'$ the total integrated inversion of the medium. Equation 2.5 tells us that the output pulse shape, and therefore also the output pulse energy, is independent of the initial spatial distribution of inversion, which is typically determined by the specific (pumping) geometry. Essentially, if only the laser pulse is of interest, any spatial dependence of the inversion population can always be safely ignored. Similarly, the final inversion distribution after passage of the laser pulse at $t = \infty$ is given by

$$\Delta_\infty(x) = \Delta(x, \infty) = \frac{\Delta_0(x)S(x)}{\exp(\gamma\sigma c n_{\text{tot}}) + S(x) - 1}, \tag{2.6}$$

and is independent of the initial pulse shape and only depends on the total amount of photons in the input pulse $n_{\text{tot}} = \int_{-\infty}^{\infty} n_0(t')dt'$. Since the increase in pulse energy and decrease in population inversion are complementary, the output pulse energy also does not depend on the temporal shape of the input pulse, but only on its energy.

Assuming a homogeneous distribution of Δ_0 and using Eq. (2.1) we write the output photon density as

$$n_{\text{out}}(x,t) = n(x, t + x/c) = \frac{n_0(t)}{1 - [1 - \exp(-\sigma\Delta_0 x)]S_-(x, t + x/c)}, \tag{2.7}$$

[1] In practice this is conveniently done numerically by using a cumulative integral function to solve the integrals.

with $\Delta_0 = \Delta_{\text{tot}}/L$. We can cast this equation in a different form by using more characteristic laser parameters [58, 67]. We choose to express the problem in terms of laser intensity $I = h\nu cn(t)$, and define the small-signal gain coefficient $g_0 = \sigma\Delta_0$ and saturation fluence $F_{\text{sat}} = h\nu/\gamma\sigma$. The output pulse intensity I_{out} at $x = L$ in terms of the input intensity I_{in} then becomes

$$I_{\text{out}}(t) = \frac{I_{\text{in}}(t)}{1 - [1 - \exp(-g_0 L)] \exp(-F_{\text{sat}}^{-1} \int_{-\infty}^{t} I_{\text{in}}(t')dt')}, \tag{2.8}$$

with time $t = t - x/c$ in a reference frame co-moving at the speed of light. This can also be written in terms of a commonly used equivalent stored energy fluence $F_{\text{sto}} = \gamma g_0 F_{\text{sat}} L$ or directly measurable small-signal single-pass gain $G_0 = \exp(g_0 L) = \exp(F_{\text{sto}}/F_{\text{sat}})$.

In the above, starting from the Frantz-Nodvik equations, we assumed a homogeneous transverse laser beam intensity and stored energy distribution. In reality, both often have a radial dependence, like in the power amplifier as presented in Sec. 2.2. The module used in that amplification-step contains an Nd:YAG crystal rod that is pumped from five sides by diode arrays. This pumping geometry allows us to efficiently control the stored energy profile, and therefore the gain profile, by tuning the cooling temperature of the module, which subsequently alters the penetration depth of the pump light into the crystal rod. Since the input beam profile has the shape of a clipped Gaussian, we tune the temperature such that the gain profile is "scooped", i.e. low in the center of the rod. These two profiles compensate such that the resulting output beam profile is a flat-top. Evidently, such strong radially dependent laser beam and gain profiles can be taken into account if more accurate calculations are desired. Nevertheless, it is often sufficient to ignore the radial variations and use system-specific 'effective' stored energy and saturation fluences.

To illustrate temporal pulse distortion by amplification, Eq. (2.8) is used to calculate output pulses for several cases which are shown in Fig. 2.A.1(a,b,d). The outcome of the amplification process and the amount of temporal distortion is determined by the ratios between F_{sto}, F_{sat}, and F_{in}. Different combinations will lead to a different gain and different distortion as can been seen in Fig. 2.A.1(a,b). In reality, to extract energy from the medium efficiently we need, $F_{\text{in}} \gtrsim F_{\text{sat}}$, and to have any significant amplification at all we need $F_{\text{sto}} > F_{\text{in}}$. In Fig. 2.A.1(a,b) this is best represented by the most strongly distorted purple dash-dot-dotted curve. For a square input pulse, distortion by amplification saturation leads to a sharp spike followed by a tail (Fig. 2.A.1(a)). For the laser system presented in this chapter the spike resulting from a square-shaped input pulse has a width of only 1.2 ns as shown in Fig. 2.3. For a Gaussian-shaped pulse the distortion leads to a characteristic skewing of the shape as shown in Fig. 2.A.1(c).

When a laser system makes use of pulse shaping before amplification, preshaping of the laser pulse is needed to compensate for the distortion and achieve a desired output shape. Equation (2.8) can be inverted [54, 67] to be able to determine

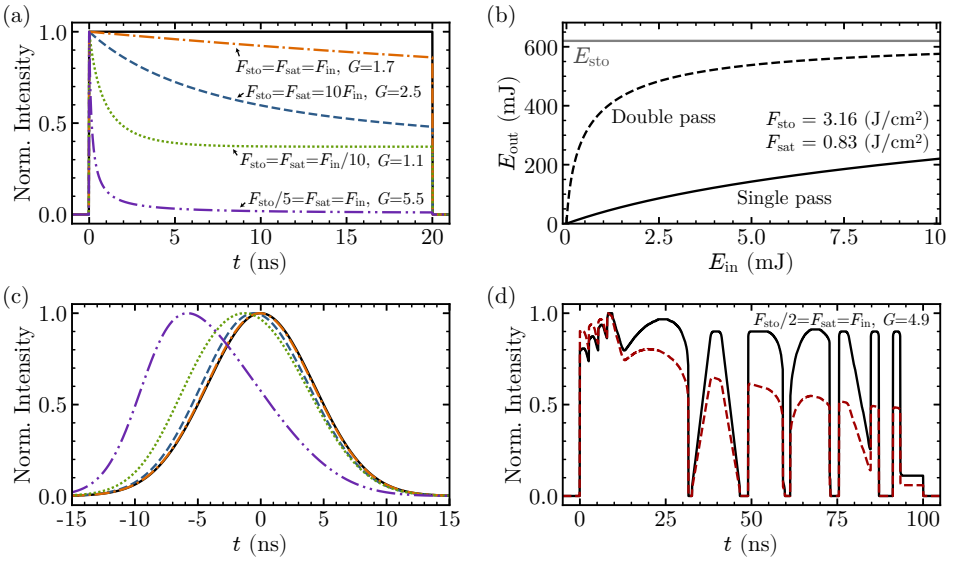

Figure 2.A.1: (a) Examples of pulse distortion of a 20 ns-square input pulse for varying combinations of F_{sto}, F_{sat}, and F_{in} and resulting gain G, calculated using Eq. (2.8). (b) Output pulse energy E_{out} as a function of input energy E_{in} calculated using Eq. (2.10) and parameters of the Nd:YAG-power-amplification stage as presented in Sec. 2.2. (c) Similar as (a), but for a Gaussian shaped pulse. (d) Temporal distortion of a laser pulse shaped like the outline of the ARCNL logo.

the input pulse shape I_{in} given a desired output I_{out}, which results in

$$I_{in}(t) = \frac{I_{out}(t)}{1-[1-\exp(g_0 L)]\exp(-F_{sat}^{-1}\int_{-\infty}^{t} I_{out}(t')dt')}. \tag{2.9}$$

With a known input pulse I_{in}, a fit of Eq. (2.8) to a measured I_{out} can be used to obtain the relevant parameters G_0 and F_{sat} (and thereby F_{sto}). With the parameters known, Eq. (2.9) can then be used to predict the input pulse needed for the desired output pulse. This approach has been successfully applied in many laser systems with arbitrary pulse-shaping capabilities [54, 56, 67–71].

By integrating both sides of Eq. (2.8) over time we obtain the output fluence F_{out} as a function the input fluence F_{in} [58, 67], given by

$$F_{out} = F_{sat}\ln\left(1+\left[\exp\left(\frac{F_{in}}{F_{sat}}\right)-1\right]G_0\right). \tag{2.10}$$

Equation (2.10) can be used when only the total output fluence is of interest. Furthermore, Eq. (2.10) again shows how the output energy, or total gain (F_{out}/F_{in}) is independent of the input pulse shape. An example of the behavior and saturation of output energy E_{out} as a function of input pulse energy E_{in} is calculated using Eq. (2.10) and shown in Fig. 2.A.1(b). Here we made use of the parameters of the Nd:YAG-power-amplification stage presented in this chapter. Using the diameters of the laser beam and Nd:YAG rod, the length of the Nd:YAG rod, the

estimated stored energy as specified by the supplier, typical input energies E_{in}, and $F_{\text{sat}} = 0.83\,\text{J/cm}^2$ resulting from the analysis presented in Sec. 2.3. As can be seen from Fig. 2.A.1(b), a double pass is needed to extract most of the energy out of the rod and achieve strong saturation of the amplifier.

2.A.1. Pulse overlap

Many laser amplifier systems make use of stages with a double-pass configuration, such as the first stage in the bounce amplifier and the power-amplification stage of the system presented in this chapter (see Fig. 2.1). In such a double-pass setup the laser pulse traverses the same gain medium twice, typically traveling in opposite directions. Making a double pass is not only a way to extract as much energy as possible from the gain medium and saturate amplification, it is often also used as a (necessary) way to compensate for depolarization effects induced by thermal birefringence [58].

A pulse duration τ_{p} that is longer than the round-trip time τ_{r} needed for the front of the laser pulse (indicated by $t = 0$ in the co-moving reference frame) to exit and again enter the gain medium will result in spatial overlap of parts of the pulse within the gain medium. That is, if $\tau_{\text{p}} > l/c = \tau_{\text{r}}$, with l the path length between the first exit and second entry point of the gain medium, overlap will occur. As is schematically illustrated in Fig. 2.A.2 the part of the pulse that is affected during the first pass runs from $t = \tau_{\text{r}}$ to the end of the pulse ($t = \tau_{\text{p}}$), and the part of the pulse that is affected during the second pass runs from the start of the pulse ($t = 0$) to $t = \tau_{\text{p}} - \tau_{\text{r}}$. Therefore, a central region of the pulse exists, that does not experience any overlap during amplification, or, during both passes when $\tau_{\text{p}} > 2\tau_{\text{r}}$.

The overlap of counter-propagating parts of the laser pulse in the gain medium will result in a decrease of the total output energy compared to when no overlap is present. In (one of) the first observations of this phenomena [72] it was described as the 'robbing' of gain from the input pass by the return pass. The distinctive trend of output energy versus pulse duration as presented in Fig. 2.4, is a result of pulse overlap.

In the case of complete overlap, when $\tau_{\text{r}} = 0$, analytical solutions to the problem of pulse amplification with overlap exist [73, 74]. For cases of partial overlap a numerical approach is required [74, 75]. Here we follow the approach of Jeong et al. [60] which consists of the following set of equations

$$G_{\text{E}}^{(n)} = \frac{F_{\text{sat}}}{F_{\text{in1}}^{(n)} + F_{\text{in2}}^{(n)}} \ln\left\{1 + \left[\exp\left(\frac{F_{\text{in1}}^{(n)} + F_{\text{in2}}^{(n)}}{F_{\text{sat}}}\right) - 1\right] \exp\left(\frac{F_{\text{sto}}^{(n)}}{F_{\text{sat}}}\right)\right\}, \tag{2.11}$$

$$F_{\text{out1}}^{(n)} = G_{\text{E}}^{(n)} F_{\text{in1}}^{(n)}, \tag{2.12}$$

$$F_{\text{out2}}^{(n)} = G_{\text{E}}^{(n)} F_{\text{in2}}^{(n)}, \tag{2.13}$$

$$F_{\text{sto}}^{(n+1)} = F_{\text{sto}}^{(n)} - \left(G_{\text{E}}^{(n)} - 1\right)\left(F_{\text{in1}}^{(n)} + F_{\text{in2}}^{(n)}\right) - F_{\text{ASE}}^{(n)} + F_{\text{pump}}^{(n)}. \tag{2.14}$$

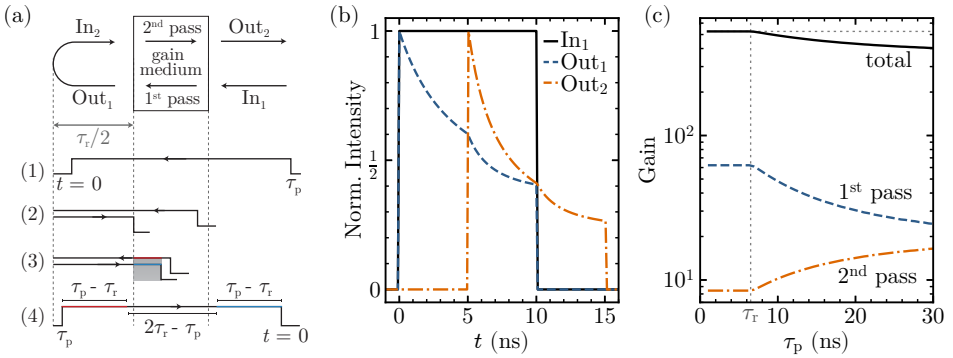

Figure 2.A.2: (a) Schematic illustration of double-pass amplification with pulse overlap. Four depicted stages of pulse propagation are: (1) The pulse is undergoing the first pass and has not yet reached the turning point. (2) The pulse is separated into forward and backward propagating parts, with the backward part having reached the gain medium. At this point overlap starts. (3) Part of the forward and backward propagating parts overlap in the gain medium. The overlap region is indicated in grey, the part of the pulse experiencing overlap-affected amplification during the 1st pass is indicated in red, and likewise indicated in blue the region undergoing the 2nd pass. (4) The pulse is now fully traveling backwards and no temporal overlap is present. As indicated, a central region of the pulse with a length $|\tau_{\mathrm{ctr}}|$, with $\tau_{\mathrm{ctr}} = 2\tau_{\mathrm{r}} - \tau_{\mathrm{p}}$, experiences no overlap when $\tau_{\mathrm{ctr}} > 0$, or overlap during both passes when $\tau_{\mathrm{ctr}} < 0$. (b) Example of pulse distortion as a result of pulse overlap with $F_{\mathrm{sto}} = F_{\mathrm{sat}} = F_{\mathrm{in}}$, and $\tau_{\mathrm{r}} = \tau_{\mathrm{p}}/2 = 5\,\mathrm{ns}$. (c) Gain as a function of pulse duration for square input pulses with an input pulse energy of $E_{\mathrm{in}} = 1\,\mathrm{mJ}$ and amplifier properties of the Nd:YAG power-amplification stage.

Equations (2.11) to (2.13) are essentially a segmented version of Eq. (2.10) for two simultaneous input and output pulses as depicted in Fig. 2.A.2(a), coupled to the stored fluence F_{sto}. By dividing any arbitrary pulse up in N parts, we can use this set of equations to amplify each part subsequently and take into account the overlap during a double pass. Note that the gain medium is assumed infinitesimally thin and Eq. (2.11) does not distinguish between the two counter propagation directions. Equation (2.14) also includes losses due to amplified stimulated emission (ASE) and an increase of F_{sto} due to simultaneous pumping. Both can often be safely ignored. If needed, additional terms like a single-pass transmission loss by reflections from optical surfaces could also be incorporated.

Figure 2.A.2(b) shows an example of pulse distortion resulting from double-pass amplification with overlap calculated using Eqs. (2.11) to (2.14). Here, for simplicity, we take a square input pulse and the conditions $F_{\mathrm{sto}} = F_{\mathrm{sat}} = F_{\mathrm{in}}$ and $\tau_{\mathrm{r}} = \tau_{\mathrm{p}}/2$. The resulting output pulses (now we have one for each pass) show two distinct distortion regions. During the first pass the drop in gain is clearly visible when overlap with the second pass starts. To illustrate the "robbing" of gain by the second pass from the first pass, the gain for both passes is calculated as a function of input pulse duration and shown in Fig. 2.A.2(c). This time we take square input pulses with an energy of 1 mJ and use again the parameters of the Nd:YAG power-amplification stage, which has a round-trip time of $\tau_{\mathrm{r}} = 6.5\,\mathrm{ns}$. As τ_{p} increases and passes τ_{r} we see an exchange of gain from the first to the second pass. Unfortunately

this results in a lower overall gain, which significantly decreases the output energy of our laser system.

Solving the pre-shaping problem in the case of a double pass with overlap is slightly more complex than in the single-pass case. In theory, everything can be calculated numerically as long as the amplification stages are properly characterised. However, it is practically more efficient to implement an optimization feedback algorithm to obtain a desired shape. A peculiar "side effect" of the presence of pulse overlap is an apparent violation of causality during pulse shaping. Altering a sample point on the (here EOM) modulation waveform at time t^*, and therefore altering the input to the amplification stage, will change the laser pulse output starting from a preceding time $t^* - \tau_\mathrm{r}$.

Chapter 3

Shock-Wave-Induced Deformation of Tin Microdroplets

In this chapter we present the deformation of tin microdroplets resulting from a shock wave launched into the droplet interior by rapid laser ablation of the droplet surface. A sufficiently intense shock wave (with a trailing rarefaction wave) induces cavitation and spallation in the droplet interior causing it to expand. Using shadowgraphy imaging we accurately record the deformation and track the expansion of the main body and the spalled layer. We find that the expansion and spall velocities mainly depend on the ratio between the laser energy incident on the droplet and the droplet volume. By combining data from several experiments using different droplet sizes and laser focal spot sizes, we conclude that this similarity holds for a remarkably large range of experimental parameters, but observe significant differences between pulses of different durations. More specifically, we compare the deformation induced by pulses with durations of 200 fs and 0.4 ns. Both the expansion and spall velocities are found to accurately follow a power-law scaling over more than 2 orders of magnitude with approximate exponents of respectively 0.7 and 0.4.

3.1. Introduction

Current state-of-the-art nanolithography exposure tools utilize extreme ultraviolet (EUV) light with a wavelength of 13.5 nm for patterning. This light is generated by ionizing a droplet of liquid tin, several tens of microns in diameter, with a high-energy laser pulse. To improve the efficiency of conversion of laser light into EUV light, which depends strongly on target morphology and the overlap between the target and laser beam, an initial *pre-pulse* is used to deform the droplet. Subsequently, a following *main-pulse* is tasked with ionizing the liquid tin which subsequently emits the relevant EUV light [62].

It was found that using a laser pulse of several tens of picoseconds or shorter as a pre-pulse leads to a spectacular explosive expansion and fragmentation of the droplet [76]. The resulting volumetric target was predicted to provide a higher conversion efficiency compared to the dense planar sheet-like targets resulting from impact of pulses with a nanosecond duration [30, 32, 77]. Using targets formed with ps-duration pre-pulses, EUV light was successfully generated with conversion efficiencies reaching 4% to 6% [16, 34, 78–80].

Several works, both through experiment [36, 37, 76, 81, 82] and simulation [39, 83], have revealed the complex processes that lead to the observed deformation after irradiating a metallic droplet with fs, or ps pulses. Since the metallic droplet is opaque to optical radiation, a direct observation of the internal dynamics is rather challenging. Therefore, the detailed understanding of this fascinating deformation process, in general and as presented in this chapter, relies heavily on the learnings from simulation [39, 83] and similar observations from experiments on transparent water droplets [84, 85].

The deformation process, as illustrated in Fig. 3.1, is driven by high pressure *shock waves* launched into the droplet interior following laser impact. For the case of femtosecond-duration pulses, when $\tau_{\mathrm{p}} \ll \tau_{\mathrm{e\text{-}i}}$, the rapid pressure pulse is applied through an isochoric heating of a thin surface layer and its subsequent rapid expansion. When $\tau_{\mathrm{p}} \gg \tau_{\mathrm{e\text{-}i}}$ the majority of the laser pulse will be absorbed in a plasma layer surrounding the droplet and by that supply the ablation pressure. The spherical geometry of the droplet causes a convergence of the propagating wave to the center of the droplet. Although, the peak pressure of a shock wave decreases with propagation due to hydrodynamic attenuation [86] along the propagation direction, the transverse convergence (focusing) is accompanied by an increase in pressure. This allows for an effective increase of the shock wave pressure as it approaches the droplet center. A negative pressure wave, or rarefaction wave, trails the high-pressure shock front, and applies tensile stress to the liquid. If the tensile strength of the liquid is exceeded, void formation (cavitation) will occur [87]. Due to the converging trajectory of the shock wave the first cavitation region is generated in the center of the droplet. The second region is generated at reflection of the shock wave on the opposing surface of the droplet. This process, in which a thin layer is ejected from the surface, is known as *spallation* [88, 89]. It has already been shown that the laser energy threshold of spallation exceeds that of the formation of the central cavity [37, 39, 82]. Thus, overall, this means the droplet expands into a

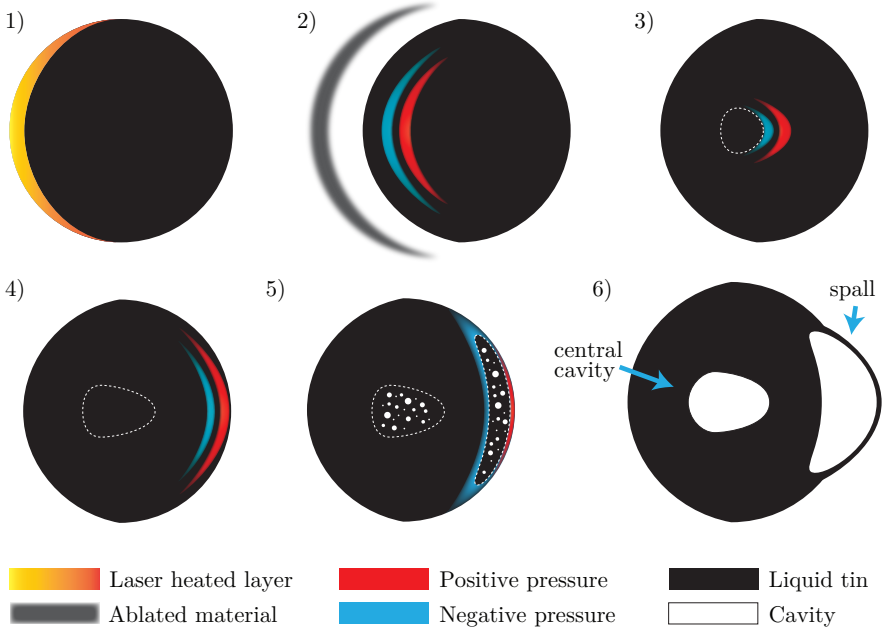

Figure 3.1: Schematic illustration of the shock-wave-excitation and deformation mechanism. 1) Rapid isochoric heating of a thin surface layer by absorption of the laser pulse incident from the left. 2) Ablation of a thin layer from the droplet surface as a result of the large temperature increase launches a shock wave. 3) Due to the droplet's spherical shape, the shock wave and accompanying rarefaction wave converge towards the center of the droplet, and a sufficiently large negative pressure results in tensile breakup of a central region. 4) The shock wave arrives at the opposing side of the droplet. 5) Reflection of the shock wave leads to spallation and voids start to form in both affected regions. 6) Both central and spall cavities are fully formed and undergo expansion.

single- or double-domed-like structure. The double-dome geometry is often said to resemble the shape of an acorn.

In this chapter we study shock-wave-induced deformation of tin microdroplets with quantitative detail by varying laser pulse length, wavelength, and droplet size. The material presented in this chapter strongly links to the studies presented in Chaps. 4 and 5, where especially the spall velocity has proven to be a valuable probe of the laser-droplet interaction process.

3.2. Experiments & Methods

In the experiment a micron-sized tin droplet is impacted by a laser pulse and the resulting deformation is recorded using two shadowgraphy imaging systems with a spatial resolution of 5 µm. The two systems simultaneously provide a side- and front-view at respectively 90° and 30° with respect to the laser propagation axis. The shadowgraphy backlighting pulse has a wavelength of approximately 560 nm and

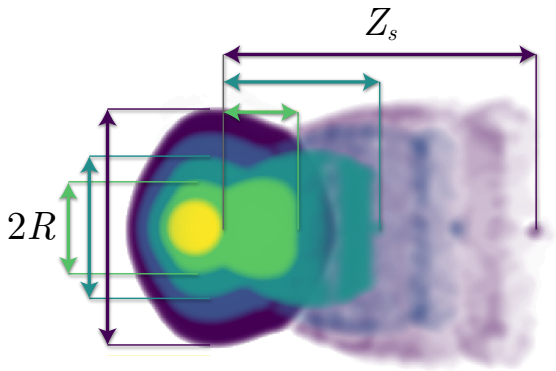

Figure 3.2: Illustration of the tracking of the two quantified deformation observables. The radius of the main cavitation bubble is obtained by tracking the diameter $2R$ at the widest point. The spall-front displacement Z_s relative to the initial droplet surface is also recorded.

duration of 5 ns, setting the temporal resolution. By scanning the shadowgraphy laser pulse with respect to the drive laser pulse we record a stroboscopic sequence of the deforming droplet. Further information on the experimental setup can be found in Sec. 1.5 and Refs. [19, 32].

To quantify the deformation as a function of time we use the side-view images to track the size of the central cavity bubble at its widest point $2R$, and the displacement of the spall front Z_s, as illustrated in Fig. 3.2. As some ambiguity of spall terminology exists in literature, note that with *the spall* we here refer to the detached layer or its fragments, not the internal plane at which spallation occurs, most often referred to as the spall plane. We omit a direct study of the obtained trajectories and limit ourselves to only initial velocities of both the central cavity and spall obtained by linear fits to a selected early time range. The motivation for this approach is twofold. Firstly, it has already been shown that the expansion dynamics of the cavitation bubble can be described with a single experimental observable [37], namely the initial rate of radial expansion $\dot{R}(t = 0)$, from hereon referred to as R_0. The absence of a (significant) center-of-mass propulsion naturally implies that the energy transfer from laser energy to kinetic energy of the liquid tin can be characterized by only this velocity (similar to the observation in Ref. [85]). Secondly, at expansion velocities similar to, or exceeding, those relevant for application in the EUV source ($\sim 100\,\mathrm{m\,s^{-1}}$), the fragmentation time of the deforming liquid tin decreases to well below the capillary time scale τ_c (see Sec. 1.3) [37] at which any possible contraction of the expanding body takes place [38]. As a result the expansion trajectories become fully ballistic up until and after fragmentation. This applies to a large part of the measurement range reported on in this chapter, with a significant deceleration of the main expanding body and spall observed only for the lower energy range.

Over several experiment runs different combinations of droplet radius R_0, laser wavelength λ, laser pulse duration τ_p, focal spot size w_0, and laser pulse energies

Label	d (µm)	τ_p	λ (nm)	Foc. Spot	w_0 (µm)	Pol.
A	45, (20 - 65)	0.4 ns	1064	Flat-top	110 x 92	Lin.
B	19-52	0.4 ns	1064	Gaussian	130 x 121	Circ.
C	45	0.4 ns	1064	Gaussian	45	Circ.
D	27	0.4 ns	1064	Gaussian	89 x 80	Circ.
F	30, 45	220 fs	1550	Gaussian	100 x 70	Circ.
Ref. [39]	49	800 fs	800	Gaussian	60	Circ.

Table 3.1: Overview of experimental parameters for all data presented in this chapter. The listed parameters in order are the droplet diameter d, the full width at half maximum (FWHM) pulse duration τ_p, the wavelength λ, the laser focal spot shape, the FWHM focal spot size w_0, and the polarization.

were studied. Table 3.1 gives an overview of all experiments and their respective parameter spaces, including the experiment reported on in Ref. [39] by Grigoryev et al. In all measurement runs, excluding the data from Ref. [39], a recording of the laser focal spot is used to determine the geometric overlap of the focal spot with the droplet. From this overlap and a direct measurement of the laser pulse energy we obtain the energy impinging on the droplet E_{od}. Between all the measurements reported on in this chapter, the peak laser fluence ranges over three orders of magnitude from approximately 3 to $7 \times 10^3\,\mathrm{J\,cm^{-2}}$ and the peak intensity spans more than four orders of magnitude, from 1.4×10^{10} up to $2.9 \times 10^{14}\,\mathrm{W\,cm^{-2}}$.

The data presented in this chapter has a significant overlap with experiments discussed in other chapters and/or publications: The data presented in Refs. [22, 63, 64] was obtained as part of experimental run A, and the data presented in Chaps. 4 and 5 was taken during experimental runs C and B, respectively. For experiments labeled A to D the in-house built laser system presented in Chap. 2 was used as the drive laser [42]. Experiment F was performed with pulses from a likewise in-house built OPCPA system [90], and is reported on in more detail in Ref. [82].

3.3. The observed deformation

The observed shock-wave-induced deformation obtained from shadowgraphy during experiments D ($\tau_p = 0.4\,\mathrm{ns}$, $d = 27\,\mu\mathrm{m}$) and F ($\tau_p = 220\,\mathrm{fs}$, $d = 30\,\mu\mathrm{m}$) is presented in Fig. 3.3. For all laser energies the formation of an expanding central cavity bubble is present. With increasing laser energy the cavity clearly expands more rapidly. For $E_{od} = 0.1\,\mathrm{mJ}$ spall formation appears close to threshold in both Fig. 3.3(a) and (b) as can be seen by the spall's low velocity and early retraction. In Fig. 3.3(a, $E_{od} = 0.2\,\mathrm{mJ}$) the spall velocity is still low enough for it to be partially retracted by surface tension, but with increased energy the spall strongly fragments at early times. The early fragmentation of the spall layer compared to the main cavity bubble wall indicates a significantly lower spall thickness arising from the distinct differences in the formation processes (see Fig. 3.1). In Ref. [36] the thickness of the spall layer was estimated to be in the order of 10 nm. Another noticeable feature, only absent for the lowest laser energies, is the formation of a 'tunnel' (confirmed in

the front view images) due to fragmentation of the front and back side of the central shell occurring first. This early fragmentation is possibly caused by a thinning of the front (laser-facing) side by the initial laser ablation and a thinning of the back side by spall ejection. Additionally, some ejection of material on the front side of the droplet (towards the laser) is present in some cases (e.g. Fig. 3.3(a, 0.1 mJ, 0.5 mJ)). This ejection is not directly predicted by simulation [39, 83] and its origin is unknown. Many of the aforementioned 'common' characteristics of the deformation have all been observed previously in Refs. [36, 37, 39, 76, 82].

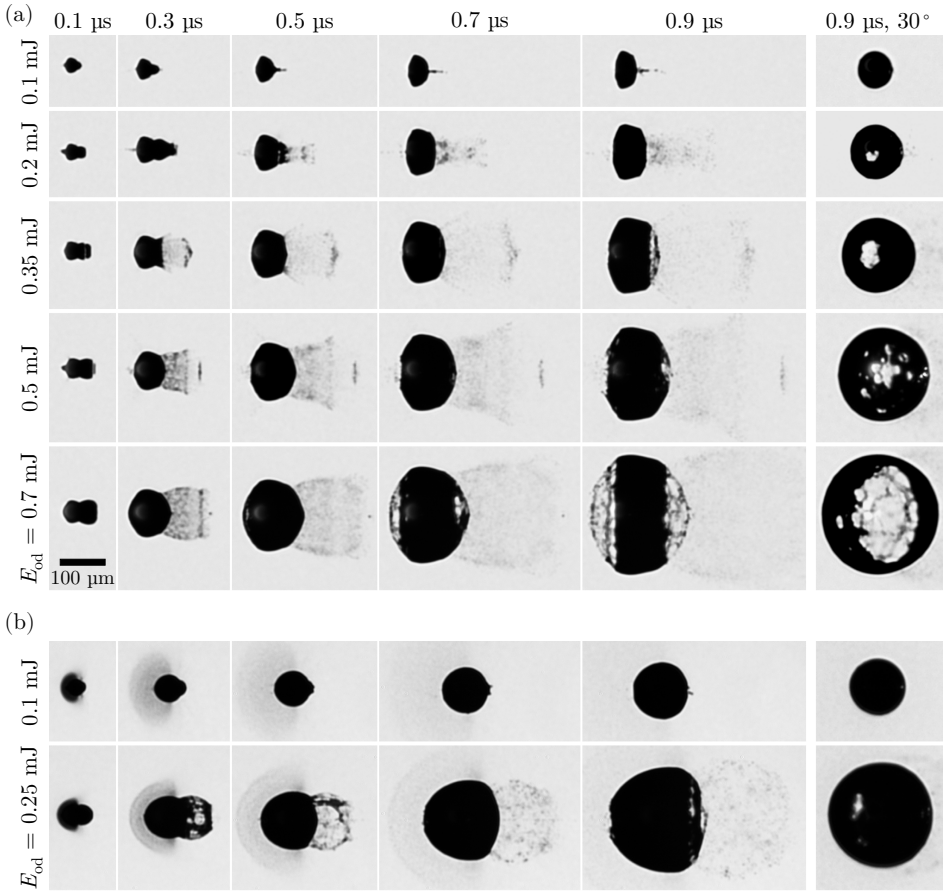

Figure 3.3: Shadowgraphy images of a deforming droplet after impact of (a) a 0.4 ns duration pulse of wavelength $\lambda = 1064\,\text{nm}$ and (b) a 220 fs pulse with $\lambda = 1550\,\text{nm}$. Columns show increasing time with respect to the moment of laser pulse impact, and rows show increasing laser energy on droplet E_{od}. All columns except the last show a 90° side-view, with the last column showing a 30° front-view at the last time delay. The data presented in (a) and (b) are obtained during experimental runs D and F with droplet sizes of 27 µm and 30 µm, respectively (see Table 3.1). The laser pulse is incident from the left.

3.4. Comparison between fs and 0.4 ns pulse induced deformation

Although impact of a pulse with a duration of 0.4 ns still induces mainly cavitation and spallation as shown in Fig. 3.3(a), a comparison with the deformation resulting from fs duration pulses as presented in Fig. 3.3(b) reveals noticeable differences. In Chapter 4 we show that the deformation resulting from a pulse with this duration (of several 100 ps) resides at the boundary of the 'pure' shock-wave-induced deformation regime. We can attempt to understand this from a basic consideration of the time and length scales involved [38] (see Eq. 1.2). Since the pulse duration is significantly longer than the electron-ion relaxation time, and similar to the plasma-hydrodynamic time scale, i.e. $\tau_{\text{e-i}} < \tau_{\text{p}} = 0.4\,\text{ns} \sim \tau_{\text{h}}$, a critical surface is likely able to form during the pulse, accompanied by a significant absorption of the laser light by the plasma, which is supported by a visible plasma emission in Fig. 3.3(a). Although it is likely that the generation of a plasma cloud layer lowers the material ablation rate through a plasma shielding mechanism [91, 92], it does not necessarily reduce the ablation pressure, or, i.e. the pressure exerted on the droplet surface as compared to direct absorption on the droplet surface. In Ref. [93] the propulsion resulting from impact of laser pulses with a duration of 10 ns FWHM is compared to simulation. A pulse of $10\,\text{ns} > \tau_{\text{h}}$ is predominately absorbed in a quasi-stationary plasma layer surrounding the droplet instead of heating the droplet surface directly. In the simulations, polar pressure impulse values ranging 10^2 to $10^3\,\text{g}\,\text{cm}^{-1}\,\text{s}^{-1}$ (0.1 Pa s) are obtained. This means (dividing by the pulse duration) that the pressure exerted on the droplet surface at its pole reaches 1 to 10 GPa, which approaches the pressures attained in the thin surface layer after rapid heating by a fs duration pulse of approximately 30 GPa as predicted by simulations [39]. A complete numerical treatment therefore seems necessary to determine if passing the onset of plasma generation and entering a regime of quasi-stationary plasma flow (termed the fully-ablative regime in Ref. [93]) leads to a significant drop in the ablation pressure.

If we assume that the transition into a different absorption and ablation regime can be mostly ignored, the instantaneous pressure on the droplet surface is proportional to the instantaneous laser pulse intensity (for $\tau_{\text{p}} > \tau_{\text{e-i}}$). In this case, to analyze the deformation we should only consider the hydrodynamic response of the fluid to the pressure pulse. From Ref. [39] we estimate that a propagating shock wave resulting from fs pulse impact quickly attains an approximate typical width of $R_0/4$. The time scale associated with this length scale is therefore given by $\tau_{\text{s}} \sim \tau_{\text{a}}/4 \sim 1\,\text{ns}$, with $\tau_{\text{a}} = R_0/c$ the acoustic time scale (see Eq. 1.2). As the pulse duration $\tau_{\text{p}} = 0.4\,\text{ns}$ approaches τ_{s} it can no longer be considered instantaneous with regards to the formed shock wave, and the resulting pressure wave will broaden and the peak pressure will drop. We can then strongly relate our discussion to the work by Reijers et al. [94], in which the pressure field evolution in the droplet is explored for the weakly-compressible regime.

In Chap. 4 we will see that for pulses with a square temporal shape, a duration of several ns, and a fast rise time of approximately 200 ps, an effective partitioning

of the absorbed energy into different (deformation) channels seems to take place. These include spherical expansion due to cavitation and spall ejection, signifying the presence of strongly compressible flow, but also center-of-mass propulsion and cylindrical expansion with flattening which can be explained assuming an incompressible liquid [30]. Predicting such deformation in detail is highly non-trivial and likely requires full numerical treatment with accurate knowledge of the equation of state of the liquid. Similarly, a direct relation between the presumed broadening of the shock wave, the resulting velocity profile inside the drop, and the distinct differences observed in the shape of the expanding shell between the 0.4 ns and fs case in Fig. 3.3(a) vs. (b) is not easily made. Nevertheless, it is reasonable to attribute the flattening of the laser facing side to the longer pulse duration. Likewise, a small, but measurable, center-of-mass propulsion U for the 0.4 ns case, as presented in Chap. 4, is related to the increased pulse duration. Overall, it is striking that, although the laser intensities between the cases shown in Fig. 3.3(a) and (b) differ by three orders of magnitude, we observe such similar target morphologies.

3.5. Similarity in deformation

A close to perfect hydrodynamic similarity of the shock-wave-induced deformation is presented in Ref. [39], where smoothed-particle hydrodynamics (SPH) simulations of 1 µm and 2 µm diameter droplets were compared to experiments on droplets with a 49 µm diameter. In these simulations, similarity of internal pressure and velocity profiles in terms of dimensionless time $ct/R_0 = t/\tau_a$ and space x/R_0 was achieved if the total deposited energy Q_{tot} per droplet volume R_0^3 (or, similarly, mass) was kept constant. Furthermore, by assuming $Q_{tot} \propto E_{od}$ they found a good agreement of expansion and spall velocities $\dot{R}_0$ and u_s between experiment (see Table 3.1) and simulation taking a reasonable constant absorption coefficient of 0.125. Refs. [32, 82] both report on a collapse of scaled $\dot{R}_0 R_0$ velocities, which is essentially an identical scaling of the dependent variable ($\dot{R}_0$) instead of the independent variable (laser energy). This collapse confirms the proposed similarity for $\dot{R}_0$ assuming an uninterrupted power-law dependence with laser energy within the given measurement range. In summary, in our experiment, we expect $\dot{R}_0$ and u_s to solely depend on E_{od}/R_0^3 for any given pulse duration and wavelength.

Figure 3.4 shows expansion and spall velocities $\dot{R}_0$ and u_s obtained from experiments A and B, with droplet diameters ranging 19 µm to 65 µm. When normalizing E_{od} by R_0^3 we indeed observe, for both $\dot{R}_0$ and u_s, a collapse of all data onto a single power-law curve whose parameter values will be discussed in Sec. 3.6. This collapse undoubtedly serves as strong experimental confirmation of a similarity in deformation and indicates that this similarity holds over a large range of R_0 and laser parameters.

In both experiment A and B the focal spot was large compared to even the largest droplet. For experiment B, where the focal spot was Gaussian, this means that the part of the focal spot incident on the droplet can be considered equally flat for different droplet sizes. Furthermore, in A the flat-top profile ensures absence of a spatial gradient in laser intensity. Subsequently, we can not yet conclude that an

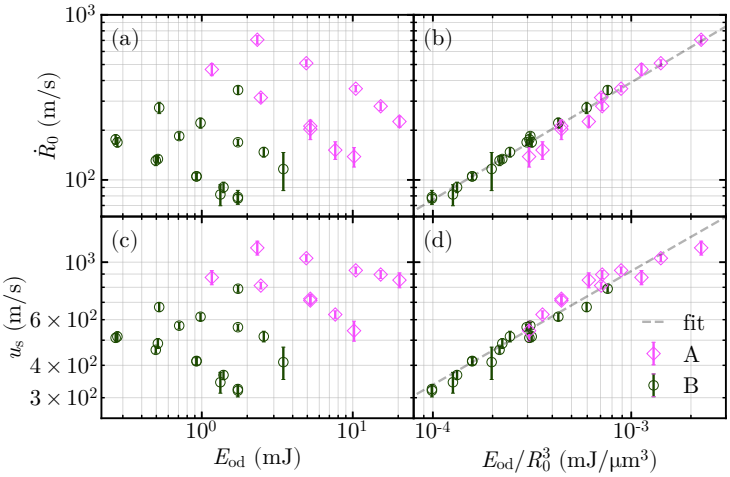

Figure 3.4: (a,c) Initial expansion velocities $\dot{R}_0$ and spall velocities u_s as a function of energy on droplet E_{od} for two droplet size scans in which the droplet diameter is varied from 19 to 65 µm. (b,d) The same data as in (a,c) as a function of E_{od}/R_0 with a power-law fit (dashed line).

anisotropic laser intensity profile has no effect on the observed collapse. However, in the next section (Sec. 3.6), with inclusion of all experiments, we will see that also with tightly focused beams (relative to the droplet size) E_{od}/R_0^3 is the sole parameter to be considered.

In Ref [82] it was shown that impact of a linearly polarized fs-duration pulse leads to a significant asymmetry in expansion of the central cavity and an even stronger asymmetric spall formation. This asymmetry is simply attributed to the inhomogeneous absorption profile of a linearly-polarized pulse arising from the different angle-of-incidence-dependent absorption for s- and p-polarized light. For experiment A, the polarization was also linear, but with only minute qualitative changes in the spall morphology as a result (not shown here). This suggests the existence of a largely 'plasma-assisted' absorption process for the 0.4 ns pulse, which is to be expected since the pulse duration is significantly longer than the electron-ion relaxation time, i.e. $\tau_p > \tau_{e\text{-}i}$. In the presence of a plasma cloud the laser energy is predominantly absorbed by the inverse-bremsstrahlung mechanism in which polarization plays a minor role. A smoothing of the pressure field by the plasma would also help explain the absence of any visible differences in deformation due to the high-frequency inhomogeneities present in the flat-top intensity profile but absent in a smooth Gaussian focal spot.

3.6. Thresholds and scaling laws of expansion and spall velocities

The $\dot{R}_0$ and u_s values from all experiments listed in Table 3.1 are shown in Fig. 3.5. We again observe a strong collapse of the data when normalizing E_{od} by R_0^3. In this case, two main separated curves for both the $\dot{R}_0$ and u_s data remain, corresponding to the data obtained using 220 fs pulses (experiment F, labeled 'fs'), and all data obtained using 0.4 ns pulses (experiment A-D, labeled 'ns'). The observed collapses again nicely confirm the proposed similarity in deformation and reveal important quantitative differences between the different pulse durations and possibly wavelengths. The data from Grigoryev et al. [39] remains separated, but follows a very similar trend to the fs curve (F). Based on refractive index data [95] we predict the absorption at 800 nm wavelength to be approximately 10% higher than that at 1550 nm. The observed discrepancy is therefore unlikely caused by the difference in wavelength, and since both pulse durations are below 1 ps, no significant effect of the difference in pulse duration is expected [76, 82]. The reason for this discrepancy therefore possibly lies in systematic (experimental) inaccuracies, such as an inaccurate determination of E_{od}/R_0^3 (from the parameters available in the published work [39]), or the velocities themselves.

The difference between the fs data (F) and 0.4 ns data (A-D) however, likely finds its origin in the pulse duration. The relative absorption difference between 1550 nm and 1064 nm wavelengths in the absence of a plasma layer is evidently below 10%, and cannot explain the observed difference in the velocities. In Sec. 3.3 we qualitatively discussed the implications of increasing the pulse duration from the fs scale to the longer 0.4 ns pulse. Considering those same arguments, it is not straightforward to conclude that this increase in pulse duration leads to a decrease in $\dot{R}_0$ and u_s as observed in Fig 3.5. Due to the presence of absorption in a plasma layer for the 0.4 ns case, the total absorbed fraction of laser energy Q_{tot} is likely higher. However, a large fraction of that energy is lost in radiation [93], and therefore does not end up as kinetic energy of the expanding liquid. Regardless of the underlying mechanisms, expansion using fs pulses is about 2.5 times more energy efficient than when using 0.4 ns pulses. From an application standpoint this contributes to enabling the selection of a preferred pulse duration. Although sub-ps pulses appear most efficient in inducing expansion, using longer pulses can have a significant practical benefit, as it is easier to obtain higher energies and the lower peak intensity typically allows for simplified laser-system architecture as compared to fs (OPCPA) systems. In such a selection process, other aspects might also have to be considered, such as the relative generation of highly-energetic ions.

From Fig. 3.5(b) we conclude that overall, the scaling of the initial expansion velocity $\dot{R}_0$ with E_{od}/R_0^3 seems to be well represented by a power law. Towards lower E_{od}/R_0^3 a downward curvature is present in both fs and ns curves, but most apparent for the fs case. This curvature is indicative of a threshold behavior, motivating us to describe the data in Fig. 3.5(b) with a shifted power law, defined as

$$\dot{R}_0 = K_{\dot{R}}(E_{od}/R_0^3 - A_{\dot{R}})^{\gamma}. \tag{3.1}$$

We simultaneously fit both the fs and ns curve in Fig. 3.5(b) with Eq. (3.1), with a shared exponent γ and threshold $A_{\dot{R}}$ but separate $K_{\dot{R}}$. The We find an excellent agreement and obtain $\gamma = 0.71(2)$, $A_{\dot{R}} = 2(1) \times 10^{-6}\,\mathrm{mJ\,\mu m^{-3}}$, and proportionality constants $K_{\dot{R},\mathrm{fs}} = 10(2) \times 10^4$ and $K_{\dot{R},\mathrm{ns}} = 4.5(4) \times 10^4$ in units of $\mathrm{m\,s^{-1}(mJ\,\mu m^{-3})^{-\gamma}}$. Although we find a good agreement using a single threshold value to fit both curves, more data points close to the threshold are needed to improve accuracy and validate the existence of a single common threshold for both pulse durations. However, since the expansion threshold measured here is essentially that of the formation of the inner cavitation bubble, such data can not be directly obtained by solely tracking the outer radius of the droplet $R(t)$. Since by conservation of volume $R(t)^3 = R_0^3 + R_\mathrm{b}(t)^3$ (when neglecting phase change), with $R_\mathrm{b}(t)$ the radius of the inner cavitation bubble, $\dot{R}(t)$ will disappear when $R_\mathrm{b}(t) << R_0$ for all t. Furthermore, perturbations will grow on a microsecond time scale and change the observed dynamics. This is clarified by the work presented in Ref. [81], where the expansion and collapse following cavitation was studied at low laser fluences. They found evidence of cavity formation down to $E_\mathrm{od}/R_0^3 \approx 1.7 \times 10^{-6}\,\mathrm{mJ\,\mu m^{-3}}$ which is in good agreement with the threshold value $A_{\dot{R}} = 2(1) \times 10^{-6}\,\mathrm{mJ\,\mu m^{-3}}$ obtained here.

The obtained scaling exponent $\gamma = 0.71(2)$ is in agreement with the value of 0.73 reported for $\tau_\mathrm{p} = 1\,\mathrm{ps}$ pulses in Ref. [82]($\lambda = 1550\,\mathrm{nm}$), which presents results from data obtained during experimental run F (see Table 3.1). In Ref [82] a decrease of the scaling exponent with increasing pulse duration down to approximately 0.64(4) for $\tau_\mathrm{p} = 10\,\mathrm{ps}$ pulses was observed. In Ref. [93] a scaling exponent of 0.46(2) was obtained for 15 ps pulses ($\lambda = 1064\,\mathrm{nm}$) which, although it agrees with the decrease for increasing τ_p, is significantly lower than expected. The common exponent of 0.71(2) for both 220 fs and 0.4 ns pulses as presented here, is not in agreement with a monotonic decrease for increasing τ_p. Although the step in τ_p made here is large, and it is possible that the complex changes in the ablation mechanism introduce a non-monotonic change in the scaling parameter γ, finding a similar value for this exponent is remarkable. Therefore, additional experiments are imperative to clarify this disparity between the values found in Refs. [82, 93].

The spall velocity u_s as shown in Fig. 3.5(e) seems to follow a similar shifted power law behavior, similarly, defined by

$$u_\mathrm{s} = K_\mathrm{s}(E_\mathrm{od}/R_0^3 - A_\mathrm{s})^\eta. \tag{3.2}$$

This time, we find that fitting with a shared threshold gives an unsatisfactory result and therefore fit with only a shared exponent η. From the fit we obtain, $\eta = 0.38(1)$, $A_{\mathrm{s,fs}} = 3.0(2) \times 10^{-5}\,\mathrm{mJ\,\mu m^{-3}}$, $A_{\mathrm{s,ns}} = 4.4(2) \times 10^{-5}\,\mathrm{mJ\,\mu m^{-3}}$, and proportionality constants $K_{\mathrm{s,fs}} = 17(2) \times 10^3$ and $K_{\mathrm{s,ns}} = 12.4(6) \times 10^3$ in units of $\mathrm{m\,s^{-1}(mJ\,\mu m^{-3})^{-\eta}}$. Although overall agreement is good, the present curvature is not completely described by Eq. (3.2), indicating a more complex threshold behavior. A possible explanation might lie in that u_s should logically converge to $\dot{R}_0$ at the spall formation threshold, which is not described by Eq. (3.2). Nevertheless, we can conclude that $A_\mathrm{s} > A_{\dot{R}}$, separated by approximately an order of magnitude, which sets the regime in which expansion without spall formation takes place. This

separation results from the distinct difference in the formation mechanisms of the central cavity and spall (see Fig. 3.1), where the central cavity is formed by the converging, high-peak-pressure shock wave at the droplet center, while the spall results from the spatially extended shock wave at the back surface. To properly verify if the obtained scaling exponent of $\eta = 0.38(1)$ also holds for the fs duration pulses measurements at higher E_{od}/R_0^3 are needed, further away from the spall formation threshold.

The physical origin of the scaling parameters γ and η is complex, and a full explanation requires extended knowledge of the ablation process as well as the equation of state of liquid tin (more specifically the thermodynamic relation between the pressure and material velocity [85] in the liquid). Although such further in-depth investigation is outside the scope of this work, the observation that $\gamma > \eta$ might be important from an application point of view. The E_{od}/R_0-dependence of the ratio $u_{\mathrm{s}}/\dot{R}_0$ (Fig. 3.5(c)), shows that u_{s} quickly grows to several times $\dot{R}_0$, exceeding $4\dot{R}_0$ at its peak for the ns data. Due to the relatively high velocity of the spall, the liquid tin contained in it is likely to escape interaction with the main-pulse, and end up as unwanted debris which negatively affects the lifetime of an EUV light source. Since $\gamma > \eta$ we can negate this possible issue by going to higher E_{od}/R_0, which of course requires higher laser energies or smaller droplets. More complex multi-pulse schemes might provide an alternative solution by slowing down the spall as elucidated in Chap. 5.

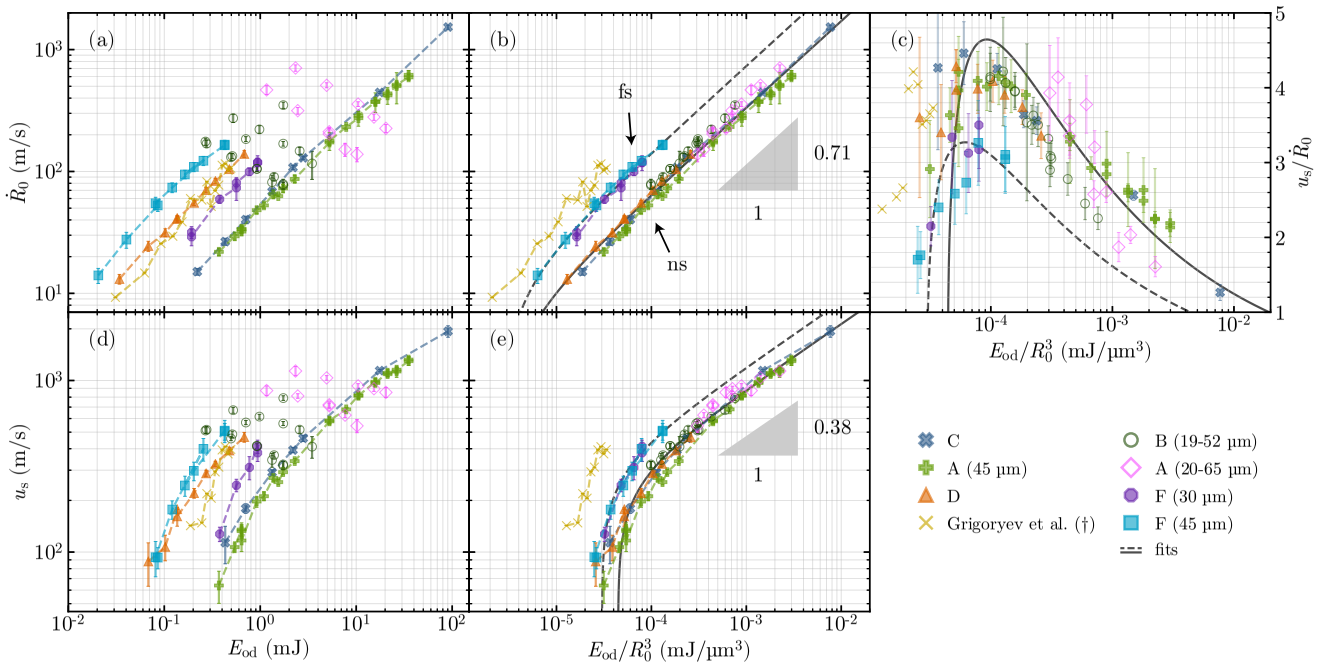

Figure 3.5: Initial expansion velocity $\dot{R}_0$ and spall-front velocity u_s of all measurement runs as function of E_{od} (a,d) and E_{od}/R_0^3 (b,e). (c) The ratio $u_s/\dot{R}_0$ as a function of E_{od}/R_0^3. The solid and dashed black lines in (b) and (e) are fits of Eqs. 3.1 and 3.2, respectively. For details of the fit parameters see the main text.

Chapter 4

The Transition From Short- to Long-Timescale Pre-pulses

We experimentally study the interaction of intense laser pulses with micron-sized metallic droplets and the resulting deformation. Two main droplet deformation regimes have previously been established: that of sheet-type expansion after impact of 'long' (typically >10 ns) pulses governed by incompressible flow, and that of spherical expansion by internal cavitation after impact of 'short' (typically <100 ps) pulses governed by shock waves, i.e. strongly compressible flow. In this chapter we study the transition between these regimes by scanning pulse durations from 0.5 to 7.5 ns. We qualitatively describe the observed deformation types and find scaling laws for the propulsion, expansion, and spall-debris velocities as a function of pulse duration and energy. We identify the ratio of the pulse duration to the acoustic timescale of the droplet as the critical parameter determining the type of deformation. Additionally, we study the influence of fast rise times by comparing square- and Gaussian-shape laser pulses. These findings extend our understanding of laser-droplet interaction, and enlarge the spectrum of controllable target shapes that can be made available for future EUV sources

4.1. Introduction

The interaction of intense laser pulses with micron-sized metallic droplets is a subject of specific importance for current generation nanolithography, utilizing extreme ultraviolet (EUV) light with a wavelength of 13.5 nm. The light is typically generated in a multi-pulse scheme where an initial *pre-pulse* is used to deform a spherical tin microdroplet into a larger target more suitable for a following main laser pulse. This main-pulse turns the target into a hot plasma emitting the desired light at a wavelength of 13.5 nm with several percent conversion efficiency [14]. The optimization of the droplet deformation process entails the formation of an optimum target for the generation of EUV light, and the minimization and mitigation of debris in the shape of high-energetic ions [17, 96–98] and neutral tin (spray) droplets. Understanding the deformation process and its dependence on laser pulse parameters is therefore of great value.

Several studies have been performed on the deformation after laser impact for 'short' laser pulses in the femtosecond and picosecond regime [36, 37, 39, 82, 83, 94, 98, 99] (see also Chap. 3), and for 'long' pulses with several ns duration [30, 32, 77, 93, 100]. The studies reveal the existence of two main types of deformation: A shock-wave-induced cavity expansion possibly accompanied by an ejected spall, resulting in a double-dome-like structure in the case of 'short' pulses, and deformation resulting from 'long' pulses, where the droplet is deformed into a thin, elongated sheet of only several tens of nanometers in thickness [33]. Aside from the identification of these two regimes, knowledge of the effects of pulse duration on laser-induced droplet deformation is limited.

In this chapter we study the transition between the two deformation regimes by using laser pulses with durations ranging from 0.5 ns to 7.5 ns. We qualitatively describe the wildly varying target shapes we observe in only this short range of pulse durations. This range clearly captures the transition from shock-wave-dominated deformation types to sheet-like expansion. Furthermore, we compare deformation resulting from Gaussian and square (constant intensity) shaped laser pulses. We quantify the deformation in terms of propulsion, expansion, and the velocity of ejected spall layers. The latter shows a laser intensity (instead of energy) dependency, which helps to understand the underlying mechanism that dictates the influence of pulse length and shape on laser-induced droplet deformation.

4.2. Experimental methods

Figure 4.1 shows a top-view schematic of the vacuum system and laser beam path. A tin droplet with a diameter of 45 µm is hit by a laser pulse with a wavelength of 1064 nm from an in-house build laser system with temporal pulse shaping capabilities [42] (see also Chap. 2). Gaussian-shaped pulses having durations τ_p of approximately 0.5, 1.3, 2, 3.5, 5, and 7.5 ns, and square (rectangular), i.e. flat intensity, pulses having durations of approximately 2, 3.5, 5 and 7.5 ns full width at half maximum (FWHM) are used in this study. The square pulses have rise and fall times of approximately 200 ps. The pulse shapes are measured with a photodiode

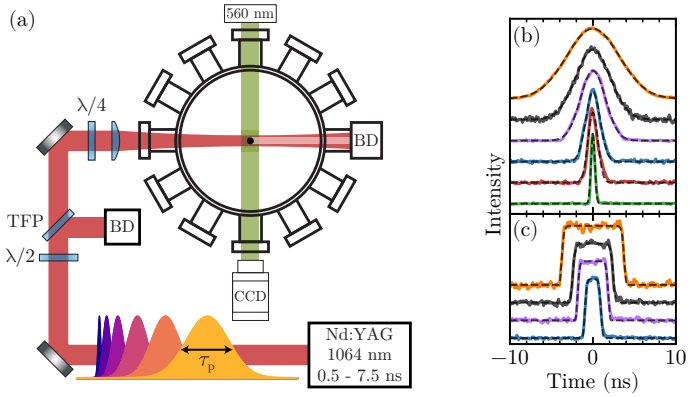

Figure 4.1: (a) Top view of the vacuum chamber with the droplet (stream) in its center. The laser energy is set using a half-waveplate and thin film polarizer (TFP) combination. The beam is dumped in a beam dump (BD). (b,c) Measured Gaussian and square pulse shapes and fits of first and higher-order Gaussians. The intensity scale of each shape is normalized to the peak intensity and offset by a fixed amount.

and oscilloscope, and an exact width is obtained by fitting first and higher-order Gaussian curves (see Fig. 4.1(b,c)). The exact widths are used in the analysis and the previously mentioned durations are used as labels throughout this work.

The energy of the laser beam is set by means of a waveplate-polarizer combination, after which the beam is focused down in the center of the chamber to a Gaussian spot with a FWHM diameter of approximately 45 µm. A quarter waveplate before the lens is used to modify the polarization of the laser beam into circular, preserving cylindrical symmetry in absorption on the droplet surface. From a camera recording of the focal spot and known droplet diameter (see Sec. 1.5), we find a geometric overlap factor of 0.44, which is used to determine the laser pulse energy fraction impinging on the droplet E_{od}.

The droplet deformation is recorded using *shadowgraphy*, in which the droplet is back-lit perpendicular to the laser propagation axis and imaged with a long-distance microscope with a resolution of approximately 5 µm. The back-lighting light source emits 560 nm wavelength pulses with a duration of approximately 5 ns, setting the temporal resolution obtainable. By delaying the back-lighting source with respect to the focused laser beam we record the deformation of the droplet after laser impact in a stroboscopic fashion. Further detail about the experimental setup can be found in Sec. 1.5.

4.3. Target Morphology

4.3.1. Influence of pulse duration

Figure 4.2 shows the deformation of the liquid tin droplet following laser-impact of Gaussian-shaped pulses with durations of 0.5 ns and 7.5 ns, and an E_{od} of 1.3 mJ.

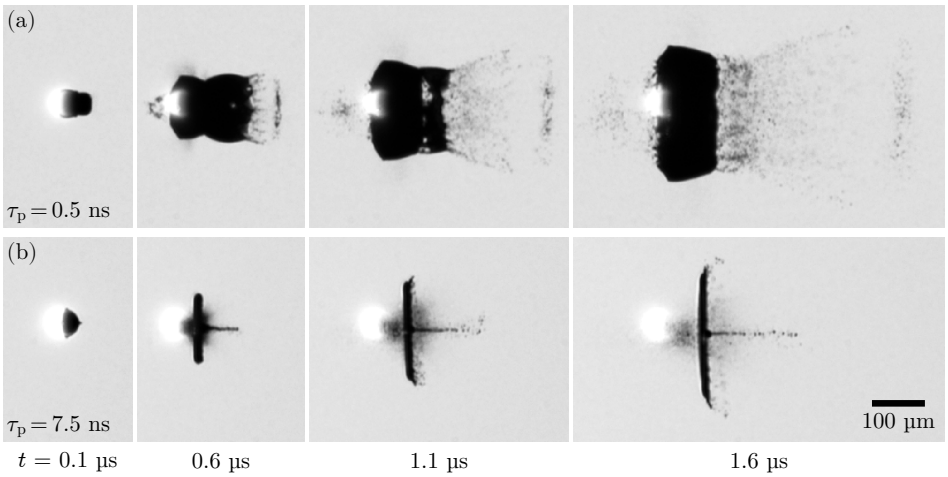

Figure 4.2: Deformation following laser impact of temporally Gaussian shaped pulses with FWHM durations of (a) 0.5 ns, and (b) 7.5 ns and an E_{od} of 1.3 mJ. Laser is incident from the left. The bright overexposed spot is light emitted from the plasma cloud. Due to the relatively long exposure time of the camera ($\sim$ ms) the light is visible in all frames, although present only for a duration similar in length to the laser pulse itself.

The two displayed deformation processes are clearly distinct. Impact of a 0.5 ns pulse results in a spherical, bubble-like expansion attributed to cavity formation in the center of the droplet [36, 37, 39, 81, 83, 98]. The laser impact excites a shock wave on the laser-facing surface which then propagates through the droplet. Due to the spherical shape of the droplet, the shock wave, and accompanying rarefaction wave, focus in the center of the droplet, resulting in internal cavitation. The shock wave subsequently reflects of the back side of the droplet and a spall layer is ejected [36, 37, 39, 83]. For a more detailed description of this process see Chap. 3 and Fig. 3.1.

The impact of a 7.5 ns pulse primarily leads to propulsion and cylindrical expansion into a thin sheet, a relatively well understood process [30, 32, 77, 93, 100]. The formation of a jet, is also clearly visible and was observed before in similar experiments [77, 98, 101]. Jet formation is commonly observed following cavity collapse [102–105]. This, along with the accompanying spray, is a possible indication that a cavity is also formed in this case, albeit smaller and expanding at a slower rate before collapsing. Further discussion on jetting can be found in Sec. 5.6.

Figure 4.3 illustrates the transition of deformation resulting from impact of temporally Gaussian shaped pulses when increasing the pulse duration from 0.5 ns to 7.5 ns. Two cases corresponding to E_{od} values of 0.4 mJ and 2.2 mJ are shown. A general trend from shock-wave-dominated deformation, exhibiting cavitation and spallation to flattening and propulsion is present with increasing pulse duration. During this transition we clearly observe a co-existence of both types of deformation.

The deformation after impact of a 0.5 ns pulse again exhibits strong spherical expansion due to shock-wave-induced cavitation in the interior of the droplet. Fur-

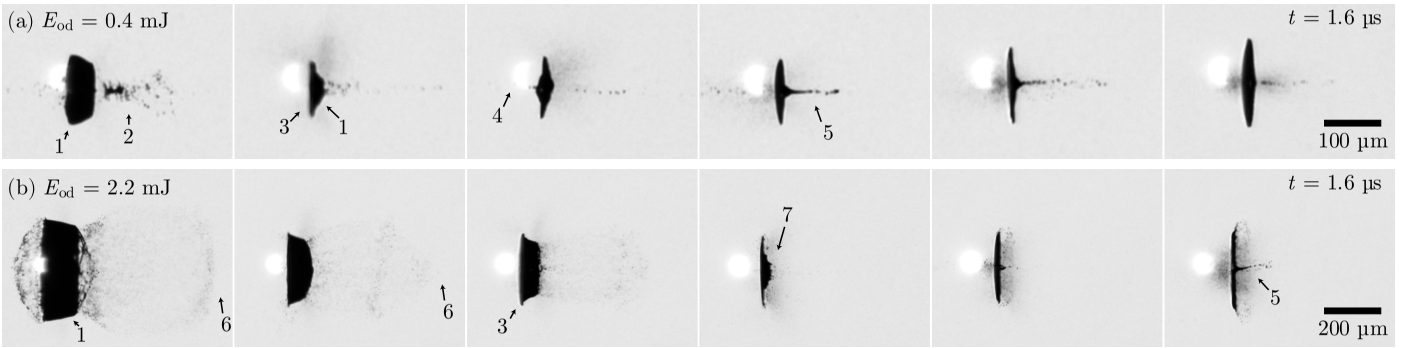

Figure 4.3: Shadowgrams of droplet deformation 1.6 µs after laser impact for the studied pulse durations and E_{od} values of (a) 0.4 mJ and (b) 2.2 mJ. Scale in (b) is twice that of (a). Laser is incident from the left. The pulse duration is indicated below each column. Several features are explicitly indicated in selected images by the following numbers: (1) central cavity, (2) collapsed spall, (3) edge flattening, (4) plasma emission, (5) jet, (6) spall front, (7) central cavity remains.

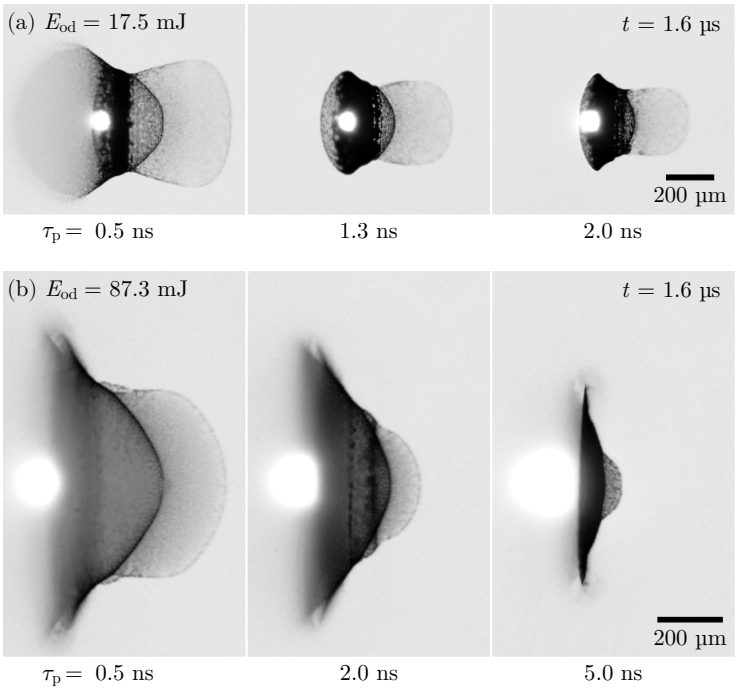

Figure 4.4: Side-view shapes at $t = 1.6\,\mu s$ after impact of temporally Gaussian-shaped pulses with E_{od} values of (a) 17.5 mJ and (b) 87.3 mJ and various pulse durations as indicated below each image.

thermore, a layer of liquid is spalled off and rapidly fragments as it expands. In Fig. 4.3(a) the remains of this spall are located on the laser axis due to its partial collapse while in Fig. 4.3(b) the spall is visible as a cloud of fragments. A jet is also present in some cases, possibly originating from the collapse of a central cavity or spall layer as mentioned previously. In Fig. 4.3(b) a shrinking of the spall cloud, indicating a decrease in its velocity, is clearly visible with increasing pulse duration and the spall is absent for longer pulse duration. Moreover, with increasing pulse duration, a flattening of the laser-facing surface becomes more apparent and spherical expansion decreases until eventually the observed shape becomes that of a flat sheet.

4.3.2. High-energy deformation features

Additional deformation effects appear when the incident energy is increased significantly. Figure 4.4 shows deformation for significantly higher values of E_{od}. Overall comparable trends are visible, with a flattening of the resulting shape with increasing pulse duration. A previously unobserved cloud, rapidly expanding radially and against the laser propagation direction, is now clearly present for the 0.5 ns pulse case. The exact origin of this cloud, which is absent for lower energies is unknown.

We speculate that a partial reflection of the rarefaction wave from the already forming cavity plays a role in the formation of this could, which is strongly flattened when the incident pulse duration increases.

In the highest energy cases studied (Fig. 4.4(b)), strong fragmentation of the droplet is observed. Although spherical expansion due to cavitation seems to still be present (the resulting curvature and the on-axis expansion of the target are still observable), no fragments moving against the laser propagation direction are visible as apposed to the lower-energy cases (Fig. 4.3(b) & Fig. 4.4(a) 0.5 ns). Significant amounts of hot and dense plasma are generated at these high energies, as also evidenced by the brighter and expanded plasma glow visible in the shadowgrams, which likely plays a role in the absence of these fragments.

4.3.3. Gaussian vs. square pulses

A significant difference in deformation following impact of temporal Gaussian or square intensity pulses is observed and highlighted in Fig. 4.5. For equal FWHM pulse widths the deformation after impact of a square pulse displays a larger spall, faster spall front, and stronger spherical expansion, whereas deformation in the Gaussian case displays more flattening of the laser-facing side. This trend indicates that the fast rise time and overall faster energy deposition of the square pulses leads to higher peak pressures of the shock wave(s) propagating in the droplet. Undoubtedly, the observation that impact of square-shaped laser pulses with a duration (of 7.5 ns) similar to the acoustic timescale $\tau_a \approx 9$ ns leads to spall formation, hints at the formation of a sharply-peaked pressure wave significantly narrower in width than $\tau_p c_0$. This conclusion is discussed further in Sec. 4.6

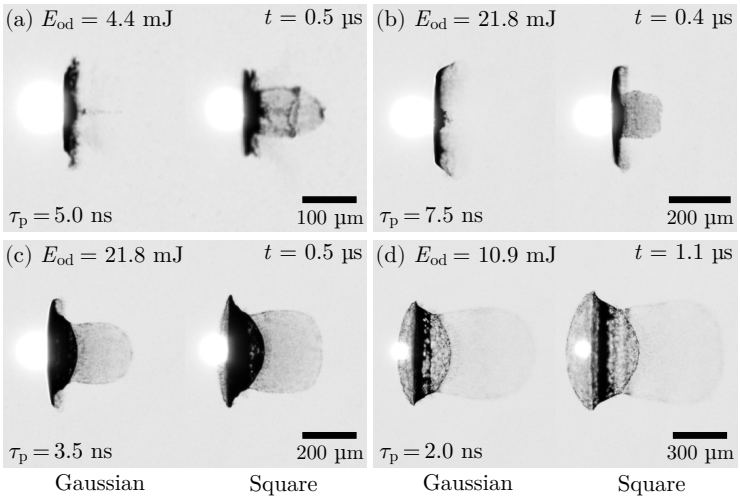

Figure 4.5: Shadowgrams comparing deformation using Gaussian and square temporal pulse shapes for various combinations of FWHM pulse duration τ_p and E_{od}. In general, a stronger contribution of shock-wave-induced deformation is present for square pulses. This is most clearly visible in the difference in size of the spall debris cloud ejected from the back side (right) of the droplet.

4.4. Laser-driven target propulsion

The propulsion U of a micrometer-sized tin droplet by laser impact has been studied in detail for the case of a Gaussian-shaped pulse with a FWHM duration of 10 ns [32, 93]. In these studies the laser-energy dependence of the on-axis propulsion was found to be accurately described by a power-law scaling with an exponent of 0.60(1) [93]. Furthermore, it was found that the energy impinging on the droplet E_{od} can be used instead of the total laser pulse energy to account for varying focal spot sizes, leading to the expression

$$U = K_U E_{od}^{0.6}. \tag{4.1}$$

Additionally, in Refs. [32, 93] an offset pulse energy $E_{od,0}$ was introduced to accurately describe the sudden loss of propulsion at low energies close to the ablation threshold (see Chap. 6). Since in this work we do not probe this low-energy regime, we omit this parameter for simplicity.

To obtain the propulsion U for the pulse durations studied in this work we apply an analogous analysis of the shadowgrams as in Refs. [32, 93]. Appropriate thresholds are applied to the shadowgrams and the center of mass (first moment) of the image is determined as a function of shadowgraphy delay time. The resulting (ballistic) displacement trajectories are fit with a linear function to obtain U.

Figure 4.6(a) shows U as a function of laser intensity E_{od}/τ_p for the various pulse durations, and both Gaussian and square temporal pulse shapes. The choice to plot U as a function of pulse intensity instead of energy is made firstly, because a deviation from the established trend is observed for high intensities (more clearly

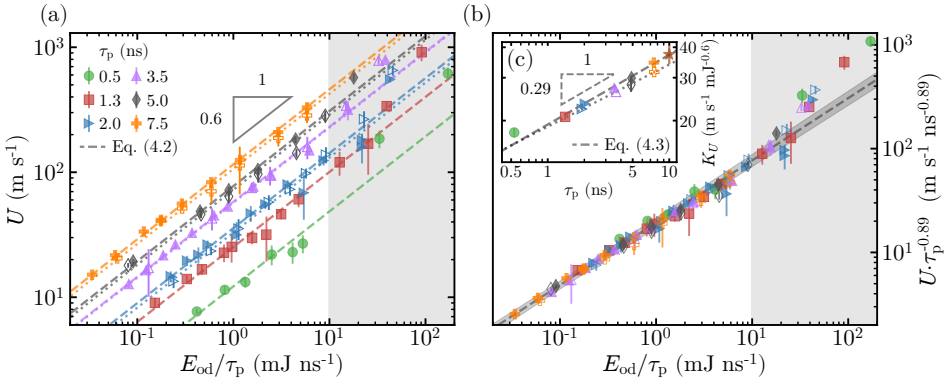

Figure 4.6: (a) Center-of-mass propulsion velocity U as function of E_{od}/τ_p for the Gaussian (filled markers) and square (open markers) pulse shapes. The vertical error bars indicate the fit parameter standard error from the linear fit to the center-of-mass displacement curve. For each combination of pulse duration and shape (Gaussian or square) the data is independently fit with Eq. (4.2). Data points in the grey region are excluded from these fits (see main text). The fit results are plot using a dashed or dotted line for the Gaussian and square pulse shapes, respectively. (b) Similar to (a) with scaled velocities $U\tau_p^{-0.89}$. (c) Proportionality constants K_U obtained from fits in (a) as a function of τ_p and fits of Eq. (4.3) for the Gaussian- and square-shaped pulses independently indicated by the dashed and dotted lines, respectively. The result for a 10 ns Gaussian-shaped pulse obtained in Ref. [93] is indicated in (b) and (c) by the dashed line (with the corresponding shaded region indicating the error) and the star-shaped data point, respectively. In (c) the star-shaped data point is not included in the fit of Eq. (4.3).

visible in Fig. 4.6(b) and discussed later), and secondly, because it separates the propulsion curves benefiting graphic clarity. We find that U increases with pulse duration and that U resulting from Gaussian and square pulses is comparable for equal E_{od}/τ_p. This indicates that the FWHM duration is an appropriate pulse-width measure when comparing U between Gaussian and square pulses in this duration regime. Note that with a FWHM definition of τ_p the Gaussian pulses have a similar (94%) peak intensity as square pulses at equal pulse energy.

Following the choice of x-axis we rewrite Eq. (4.1) into

$$U = K_{U,I} \left(\frac{E_{od}}{\tau_p} \right)^{0.6}, \tag{4.2}$$

from which follows $K_U = K_{U,I}\tau_p^{-0.6}$. We fit Eq. (4.2) to the data and find a good agreement for all pulse durations up to intensity values of 20 mJ ns^{-1}. Values above this range seem to deviate, therefore, with additional margin, we exclude values above 10 mJ ns^{-1} from the final fitting procedure of which the results are shown in Fig. 4.6(a). Note that in the propulsion studies reported on in Refs. [32, 93] the maximum laser intensity studied is below the regime were a deviation is observed, i.e. $E_{od}/\tau_p < 10$ mJ ns^{-1}.

The proportionality constants K_U obtained from the fits are plotted as a function of pulse duration in Fig. 4.6(c). A power-law scaling of K_U with τ_p is apparent, we

	β	L_U (m s^{-1} mJ$^{-0.6}$ ns$^{-\beta}$)
Gaussian	0.29(2)	19.3(5)
Square	0.26(1)	18.9(7)

Table 4.1: Results of fits of Eq. (4.3) to the data shown in Fig. 4.6(c). The given errors are the standard error of the fit parameter.

therefore write

$$K_U = L_U \tau_\mathrm{p}^\beta. \tag{4.3}$$

Fits of Eq. (4.3) to the data for Gaussian and square pulse shapes independently provide values for β and L_U. The results are shown in Table 4.1. We find no significant difference between L_U and β for the two different pulse shapes, again indicating that impact of Gaussian- or square-shaped pulses results in (close to) equal propulsion velocities when the FWHM definition is used for τ_p.

The obtained value(s) of β can be used to collapse all data onto a single curve using the appropriate scaling of $U\tau_\mathrm{p}^{0.6+\beta}$ as shown in Fig. 4.6(b). We have here used the result $\beta = 0.29$ obtained for Gaussian pulse shapes. After collapsing all data, the previously mentioned deviation at high intensities is clearly visible. For $E_\mathrm{od}/\tau_\mathrm{p} \gtrapprox 20\,\mathrm{mJ\,ns^{-1}}$ U increases at an approximately linear rate, faster than the established power of 0.6. The increased scaling possibly originates from a significant increase in the ablated mass fraction in this regime and could be investigated with dedicated simulations [40, 93]. It is also possible that a systematic overestimation of U arises during the shadowgraphy analysis due to the extreme deformation and fragmentation as shown in Fig. 4.4. In Fig. 4.6(b,c) we additionally plot the result from Ref. [93] and find an excellent agreement with the current dataset. Since in Ref. [93] the majority of the data was obtained using a droplet size of 47 µm a correction of K_U is applied to enable comparison with the droplet size of 45 µm used in this work. For this correction we apply a scaling of $K_U \propto R_0^{-2.2}$ with droplet radius R_0, as predicted in Ref. [93] and experimentally confirmed in Ref. [33].

In Ref. [93] a scaling of $K_U \propto \tau_\mathrm{p}^\beta$, with $\beta = 1 - 0.6 = 0.4$, was predicted, where the value of 0.6 follows from the exponent in Eq. (4.1). The values of β obtained here are not in full agreement with this prediction, which was made assuming that the exponent of 0.6 does not vary with τ_p. Although we find a good agreement with our measurements when applying this assumption, we cannot yet exclude minor deviations of the exponent in Eq. (4.1) for which a more extensive and more accurate dataset is needed. The discrepancy between the prediction and our measurement is possibly inherent to the pulse-duration regime studied here. It has been shown that a quasi-stationary ablation front forms when the pulse duration τ_p is significantly longer than the hydrodynamic timescale of the plasma τ_h, i.e. $\tau_\mathrm{p} \gg \tau_\mathrm{h}$ [40]. Since $\tau_\mathrm{h} \sim 1\,\mathrm{ns}$, the assumption $\tau_\mathrm{p} \gg \tau_\mathrm{h}$ does not hold for the full range of pulse durations and energies studied here, leading to a deviation from the predicted scaling. It is therefore possible that a determination of β for longer pulses will result in a different

value. Altogether, the extension of the behavior of U from previous studies [32, 93] to the pulse duration regime studied here is remarkable considering the wildly varying deformation types.

4.5. Target expansion dynamics

The expansion of liquid droplets following laser impact has previously been studied for both of the 'asymptotic' cases of the present work, that of expansion into a thin sheet [30, 32, 77, 93, 100] and that of spherical bubble-like expansion due to cavitation [37]. In both cases the observed late-time expansion trajectories can be well described using analytic fluid-mechanical models. In the pulse-duration transition regime measured here the observed shapes strongly depart from these two specific cases (of a stretching sheet and a bubble) and display strong non-trivial variations. As such, no analogous fluid-mechanical model would warrant a comparison with the current measured expansion trajectories. Furthermore, in the aforementioned fluid-mechanical models the initial rate of radial expansion immediately after laser impact $\dot{R}(t=0)$, hereafter referred to as $\dot{R}_0$, was shown to be the most relevant observable which sets the expansion trajectory until significant fragmentation occurs. Naturally, when the expansion rate is large enough, fragmentation occurs before any significant deceleration of the expanding liquid takes place, and the complete expansion trajectory becomes ballistic with a velocity $\dot{R}_0$. Motivated by the above we limit ourselves to an analysis of $\dot{R}_0$, which is obtained by a linear fit to an early time range of the expansion curve.

Due to the strongly varying shapes it is difficult to set a clear universal size measure. In general, the size of the target is determined at its widest point, excluding fragments detached from ligaments that sometimes form on the edge of the sheet-like targets and excluding the spall when present. For shapes exhibiting a spherical-like expansion that display a clear size difference between the widest overall point and the widest point of the expanding central cavity, the relevant width is taken to be that of the central cavity. This is for example the case in Fig. 4.4(a) at $\tau_\mathrm{p} = 0.5\,\mathrm{ns}$, where the widest point of the central cavity approximately corresponds to the "waist" of the total observed shape.

Figure 4.7(a) and (b) show $\dot{R}_0$ as a function of E_od for the Gaussian- and square-shaped pulses, respectively. It is clear that, analogous to U, $\dot{R}_0$ follows a power-law dependence with laser energy. We therefore write

$$\dot{R}_0 = K_{\dot{R}} E_\mathrm{od}^{\gamma}. \tag{4.4}$$

Although some variation between the different pulse durations is especially apparent for the Gaussian-shaped pulses, all data can be reasonably described by a single power-law curve. This correspondence to a single-power law is remarkable, given the very different overall target shapes observed for different pulse durations. A single fit of Eq. (4.4) to all data points in Fig. 4.7(a) and 4.7(b) combined results in $\gamma = 0.70(1)$ and[1] $K_{\dot{R}} = 42(2)\,\mathrm{m\,s^{-1}\,mJ^{-\gamma}}$ and is indicated by the black dashed line.

[1] Note that $K_{\dot{R}}$ here differs in units from the $K_{\dot{R}}$ stated in Sec. 3.6.

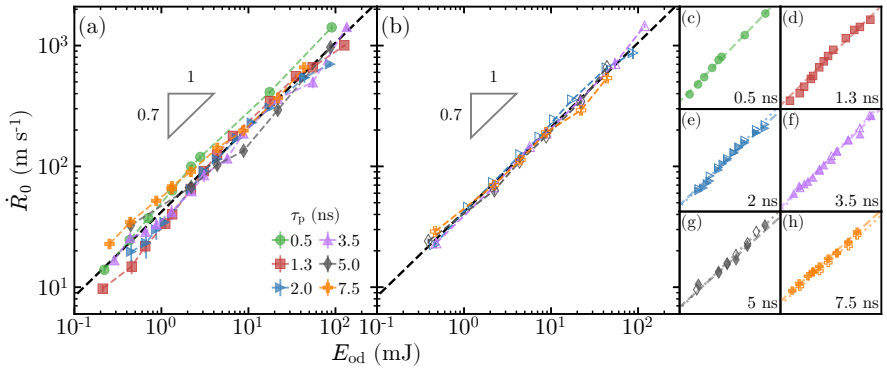

Figure 4.7: Initial expansion velocity $\dot{R}_0$ as function of E_{od} for all pulse durations and (a) Gaussian (filled markers) and (b) square (open markers) pulse shapes. (c-h) Individual plots of each pulse duration. Scale in (c-h) is equal to (a) and (b).

	Gaussian		Square	
τ (ns)	γ	$K_{\dot{R}}$	γ	$K_{\dot{R}}$
0.5	0.74(2)	51(2)	-	-
1.3	0.71(3)	38(3)	-	-
2	0.67(3)	41(3)	0.73(2)	42(2)
3.5	0.71(2)	39(2)	0.76(2)	37(2)
5	0.64(8)	39(8)	0.71(3)	41(4)
7.5	0.65(1)	56(1)	0.64(2)	44(2)
mean	**0.69(4)**	46(8)	**0.72(5)**	41(3)

Table 4.2: Results of fits of Eq. (4.4) to $\dot{R}_0$ curves shown in Fig. 4.7. Bottom row contains the mean of each column.

To investigate any changes with pulse duration and pulse shape, fits of Eq. (4.4) to each separate pulse duration and shape are also performed. The results are shown in Fig. 4.7(c-h) and listed in Table 4.2. Unsurprisingly, almost all values of γ are very similar and a more accurate determination is needed to confirm any overall trend with τ_p and pulse shape. However, for the Gaussian and square 7.5 ns pulses we find significant below-average values for γ of 0.65(1) and 0.64(2), respectively, whereas all other cases are consistent with $\gamma \geq 0.7$. Likewise, a clear trend in $K_{\dot{R}}$ is absent, although the values for the shortest and longest pulses (0.5 ns and 7.5 ns) show moderately larger values, indicating that radial expansion in the transition regime is possibly less efficient.

The physical origin of the scaling parameter γ is likely complex due to its sensitivity to the equation of state of the liquid, the specific spherical geometry, and the details of the laser-ablation process. For the short-pulse regime ($\tau_p \ll \tau_a$), when expansion is initiated by cavitation effects, a more detailed investigation of γ can be

found in Sec. 3.6 where $\gamma = 0.71(2)$ was obtained. This value is in good agreement with all but the $\tau_p = 7.5\,\text{ns}$ results obtained here. For the long-pulse regime the physical origin of γ is likewise complex. However, from the analogy with studies on the impact of water droplets on rigid pillars [106] we expect that $\dot{R}_0 \simeq U$ as follows from energy conservation arguments. Therefore, following Sec. 4.4 and by equating Eq. (4.1) with Eq. (4.4), we predict that for the case of sheet-like expansion, when $\tau_p \gtrsim \tau_a$, $\gamma \sim 0.6$. The decrease of γ from ≥ 0.7 to approximately 0.65 for the $\tau_p = 7.5\,\text{ns}$ pulses is in agreement with this expectation.

Expansion versus propulsion

Previous work [30] has shown that, dissimilar to the pillar-impact case [106], the ratio $\dot{R}_0/U$ for the laser-impact case of sheet expansion is influenced by the focal spot size relative to the droplet size. A relatively smaller laser focal spot leads to an increasingly focused pressure field which subsequently results in a larger $\dot{R}_0/U$ ratio. Furthermore, a scaling of the ratio $\dot{R}_0/U$ to laser pulse energy has been shown to exist [77]. This is due to the expansion dynamics of the plasma formed during the laser-droplet interaction process. During laser impact, a plasma cloud is formed that expands around the droplet and exerts the relevant pressure on the droplet surface. As a result of this plasma expansion the spatial pressure profile imparted on the droplet is broadened, and can in fact extend beyond the laser-facing side [93]. The extent to which the initial droplet-to-focal-spot size ratio influences $\dot{R}_0$ in the shock-wave-dominated regime is unclear, but likely dissimilar to its effect for longer pulses. Furthermore, it is straightforward to conclude that the above-mentioned plasma-expansion effects are absent when $\tau_p \lesssim \tau_h$. Accordingly, we cannot ignore these effects when comparing the expansion velocity between different pulse durations. For the 7.5 ns Gaussian pulse, which induces sheet-like deformation most comparable to that studied in Ref. [77], we observe $\dot{R}_0/U = 1.4(2)$ with no significant dependence on laser energy. The absence of such a dependence could be the result of the relatively tight focusing condition used here, which limits the growth of the plasma cloud. The presence of such a dependence would likely also cause a stronger deviation of γ from the predicted 0.6 and therefore negate the agreement ($\gamma \sim 0.6$) we have observed. In summary, changing the focusing conditions to a more tightly focused beam, or equivalently increasing the droplet size, might increase $\dot{R}_0/U$ such that long pulses will induce a faster expansion compared to short pulses at equal energy. Complementary, a more loosely focused laser beam, or smaller droplet, will only reduce expansion for long pulses, whereas expansion for short pulses is probably largely unaffected.

4.6. Spallation dynamics

The spall front velocity u_s is determined from the experiment (see Fig. 3.2) and shown in Fig 4.8. As expected and shown in Fig. 4.8(a,b), u_s increases with E_{od}. Moreover, a decrease with increasing τ_p is observed, and for the 7.5 ns Gaussian pulse no spallation was observed. Since the velocity of the spall will depend on the peak pressure of the shock wave, and the ablation pressure that excites the

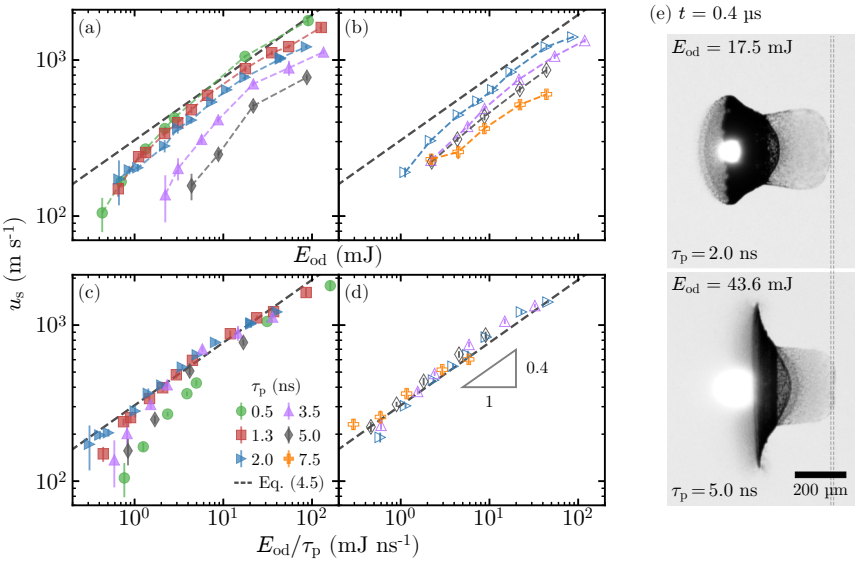

Figure 4.8: Spall-front velocity u_s as a function of E_{od} for (a) Gaussian and (b) square pulse shapes. u_s As a function of E_{od}/τ_p is shown in (c) and (d) for the Gaussian and square shapes, respectively. Note that data for the 7.5 ns Gaussian pulse is absent from the plot since there was no spall observed for this pulse. The grey dashed line indicates the fit of Eq. (4.5) to the data in (c,d) with exclusion of the 0.5 ns and 5 ns Gaussian pulses (see main text for details). For reference, the fit result is also plot in (a,b) taking $\tau_p = 1$. (e) Shadowgrams of two different pulse parameters with equal laser intensity, demonstrating the matching spall velocity.

shock wave is assumed to depend on the laser intensity, we expect a laser intensity-dependent trend for u_s. Indeed, a clear collapse is observed for u_s as a function of pulse intensity as shown in Fig. 4.8(c,d). However, a significant deviation of the curves for the 0.5 ns and 5 ns Gaussian pulses is present. These deviations - and at the same time - the remarkable overlap of all square pulses, suggests that a characteristic timescale τ_{ch} exists that dictates effective coupling of the laser pulse to the shock wave causing the spall. An upper limit for τ_{ch} is then set by the shortest square pulse, and a lower bound is set by the shortest, deviating Gaussian pulse, meaning $0.5\,\text{ns} < \tau_{ch} < 2\,\text{ns}$.

The continued presence of spallation for longer square pulses indicates the formation of a sharp-peaked shock wave following a fast rise time, even under the condition of continued loading by ablation pressure. In a one-dimensional geometry, hydrodynamic attenuation combined with a significant propagation distance allows for a conversion of an initial uniform shock wave into a peaked, triangular-shaped shock wave [86, 107]. However, this process takes place on a timescale significantly longer than the duration of the applied pressure pulse and therefore, since for the longest pulse durations applied here $\tau_p \sim \tau_a$, does not explain the formation of a peaked pressure pulse in our case. In Ref. [94], where a model for impact of continuous pressure pulses on droplets is developed, a separation of a leading narrow

pressure peak with a width on the order of $0.1R_0$ is observed during the laser pulse. Since in this case the details of the laser ablation process are not modeled but simply a temporally constant pressure is applied, it indicates that pure hydrodynamics and the spherical geometry play a deciding role in the formation of a leading shock wave under continuous loading. Accordingly, the shape and evolution of this shock follows a hydrodynamic similarity analogous to that presented in Ref. [39]. As the leading shock is considered responsible for the generation of the spall, the aforementioned characteristic timescale τ_{ch} should be directly related to the width of the shock wave and scale with the droplet radius R_0. In Ref. [39], where impact of femtosecond-duration pulses ($\tau_{\mathrm{p}} \ll \tau_{\mathrm{a}}$) on tin microdroplets is simulated using smoothed-particle hydrodynamics, the resulting shock wave attains a width on the order of $0.1R_0$, similar to that in Ref. [94]. We therefore expect $\tau_{\mathrm{ch}} \sim 0.1R_0/c_{\mathrm{s}}$ with c_{s} the propagation velocity of the shock wave. With the present droplet diameter of 45 µm, and approximating c_{s} by the speed of sound ($2500\,\mathrm{m\,s^{-1}}$), we obtain $\tau_{\mathrm{ch}} \sim 1\,\mathrm{ns}$. This is in agreement with the aforementioned upper and lower boundaries observed from experiment. As c_{s} increases with peak pressure, some variation in τ_{ch} is expected as function of laser intensity. Additionally, significant variation of τ_{ch} is expected to arise when the laser focal spot becomes significantly smaller than the droplet size, giving rise to an increasingly 'narrow' ablation pressure profile along the droplet surface. Evidently, this results in non-trivial changes of the internal pressure evolution.

For the spallation dynamics, again a power-law dependency is observed as a function of laser energy and intensity. Motivated by the demonstrated collapse we limit ourselves to an analysis considering laser intensity only and write

$$u_{\mathrm{s}} = K_{\mathrm{s}} \left(\frac{E_{\mathrm{od}}}{\tau_{\mathrm{p}}} \right)^{\eta}. \tag{4.5}$$

A fit to the data of Fig. 4.8(c,d) combined, excluding the most deviating curves of the 0.5 ns and 5 ns Gaussian pulses, gives $\eta = 0.40(1)$ and[2] $K_{\mathrm{s}} = 306(7)$ in units of $\mathrm{m\,s^{-1}\,ns^{\eta}\,mJ^{-\eta}}$. The value of $\eta = 0.40(1)$ is in good agreement with the value of $\eta = 0.38(1)$ obtained in Chap. 3, where a dataset consisting of data from 0.4 ns and fs-duration pulses was used, and a threshold value was incorporated in the power-law expression to partly explain the observed curvature in u_{s}.

4.7. Discussion & Conclusions

From the range of observations on the pulse duration dependence of target propulsion, expansion, and spallation, we find that the studied range of pulse durations between 0.5 and 7.5 ns truly forms the transition regime between the observed sheet-like expansion [32, 77, 100] and the cavitation-driven bubble-like expansion [36, 37, 39, 83] for the employed droplet diameter of 45 µm. The main reason for this transition seems to be the ratio of the pulse duration τ_{p} to the liquid acoustic timescale at which pressure waves propagate through the droplet $\tau_{\mathrm{a}} = R_0/c$.

[2] Note that K_{s} here differs in units from the K_{s} stated in Sec. 3.6.

Evidently, no hard separation between the regimes exists. Sheet-type expansion, which has previously been explained by assuming incompressibility and considering only the time-averaged pressure fields, follows when $\tau_p \gtrsim \tau_a$. Yet, when $\tau_p \sim \tau_a$ minor indirect signs of cavitation remain in the form of spray and jetting. When $\tau_p \lesssim \tau_a$, compressible flow becomes significant and the time-dynamics of the internal pressure profiles, i.e. shock waves, will increasingly dominate the deformation by inducing cavitation and spallation.

Furthermore, we have extended the knowledge on laser-driven-propulsion to the explored pulse duration regime and find a reasonable agreement to previously determined scalings of propulsion with laser energy and pulse duration. We find that propulsion resulting from impact of square- and Gaussian-shaped pulses is comparable when taking the full-width-at-half-maximum pulse-width definition at which a similar peak intensity is reached at equal pulse energy.

The radial expansion velocities were found to show a remarkable insensitivity to the pulse duration and shape, and depends almost solely on the laser pulse energy. The scaling of the expansion velocity with the laser pulse energy was found to be in agreement with expectations and previously obtained results, although we stress that these observations cannot be considered independent of the droplet and focal spot sizes.

Lastly, we have also shown that when using fast-rise-time square pulses with a sufficient intensity, a spall is always formed, even for longer pulses when $\tau_p \sim \tau_a$ and the main expansion dynamics are sheet-like. This is the result of the geometry-specific non-trivial formation of a peaked shock wave with a width on the order of $0.1R_0$ traversing the droplet. This observation suggests that, to prevent the formation of a leading peaked shock wave and spall, or a trailing rarefaction wave and central cavity, not the pulse duration itself, but respectively the rise and fall times of the laser pulse need to be similar to τ_a. Evidently, for Gaussian pulses this is by definition the case.

From this research, a comprehensive picture of the overall effect of pulse duration and shape on laser-induced droplet deformation is retrieved. This work may therefore contribute to a better understanding of laser-driven target shaping, which is an important aspect of efficient tin-based laser-produced plasma sources for next-generation EUV lithography.

Chapter 5

Spall Velocity Reduction in Double-Pulse Impact on Tin Microdroplets

We explore the deformation of tin microdroplets of various diameters induced by two consecutive laser pulses having pulse durations of 0.4 ns. Impact of laser pulses with this duration mainly leads to shock-wave-induced cavitation and spallation in the presence of a significant plasma pressure. The main result obtained in this work is the observation of a strong reduction of the spall velocity which depends on the time delay between the two pulses. This reduction reveals a complex interplay between the aforementioned plasma recoil pressure and shock-wave-driven deformation, and enables an estimation of the moment of spall formation and the average shock-wave propagation velocity. We find that the shock wave traverses the droplet with an average velocity ranging from 1.2 to 1.6 times the speed of sound. We study the effects of the energy of the second pulse on the deformation and qualitatively discuss the formation of microjets. Crucially, we demonstrate the ability to manipulate the microdroplet expansion and spallation with double-pulse sequences, thereby increasing the portfolio of obtainable target shapes for droplet-based extreme ultraviolet light sources.

Parts of this chapter have been published in Physical Review Applied **16**, 024026 (2021) [108].

5.1. Introduction

The interaction of laser pulses with metallic, and specifically tin, microdroplets and the resulting deformation has been a significant field of interest since the introduction of the *pre-pulse* in current-day extreme ultraviolet (EUV) sources for nanolithography [14, 29]. The purpose of the pre-pulse is to initiate a hydrodynamic expansion of the droplet. This deformation process is crucial, as it leads to a tin target with a more beneficial mass distribution for interaction with a following more energetic laser pulse, whose purpose is to create the optimum plasma conditions enabling EUV light generation [62].

Two main types of target are accessible using a conventional single laser pulse. Deformation into a thin liquid sheet can be initiated by impact of a laser pulse with a duration of several to tens of nanoseconds [32, 100]. For metallic droplets, this type of deformation is initiated by a recoil pressure from the expanding plasma generated by the laser pulse [93], and the resulting propulsion, expansion, fragmentation, and overall target morphology are well understood [30, 32, 33, 77, 93, 100, 109]. As elaborated in Chap. 3, impact of intense pulses of shorter duration ($\lesssim 1\,\mathrm{ns}$) launches a shock wave into the droplet. Because of the spherical geometry, the shock wave converges towards the center of the droplet which leads to cavitation if a sufficiently low negative pressure is reached [36, 37, 39, 76, 79, 81, 83, 110]. The formed vapor cavity can then rapidly expand, turning the initial droplet into a thin shell. Additionally, albeit with a laser energy threshold significantly higher than that of the central cavitation, spall will be ejected upon reflection of the shock wave from the opposing droplet surface [36, 37, 39, 76, 83, 88, 111]. Cavitation with or without spallation will lead to a single- or double-domed target morphology, respectively. Although these two types of deformation are predominantly separated into regimes by origin of the laser pulse duration, there is significant overlap and both types will often coexist (see Chap. 4). Partly due to this coexistence, a broad diversity of obtainable deformation types exists which remains largely unexplored.

Industrially relevant EUV sources typically operate with tin targets of a few hundred micrometers in diameter, formed within a few microseconds after pre-pulse laser impact [34, 35, 79, 112]. When operating in the shock-wave-dominated deformation regime using 'short', subnanosecond pulses, the expansion velocities needed to reach such diameters can only be produced by pressure waves that exceed the spallation threshold [36, 37, 39]. The spall itself can however be considered unwanted, as tin fragments are propelled away at typical velocities several times the expansion velocity of the main central shell [39]. These fragments can possibly escape interaction with the main pulse, adding to debris, or alternatively, any EUV light generated from this extended part of the target will be lost if it exceeds the etendue of the collection optics. The ability to generate expanded targets without fast spallation debris [98] could therefore be a valuable tool and favor the applicability of shock-wave-induced deformation.

In this work, we study tin microdroplet deformation induced by impact of two laser pulses having durations of 0.4 ns delayed by several to tens of nanoseconds. Impact of a single pulse with a duration of 0.4 ns predominantly leads to shock-

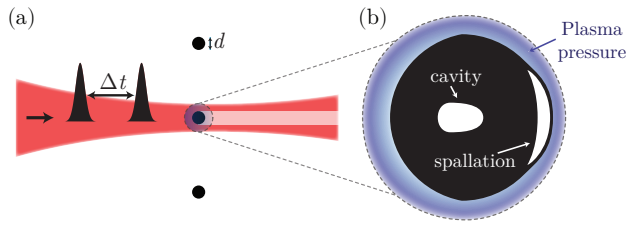

Figure 5.1: (a) Illustration of the two laser pulses spaced by a time delay Δt incident on a tin microdroplet with diameter d. (b) Illustration of the central cavity and spall formation after first laser impact and the plasma pressure surrounding the droplet as a result of the second pulse impact.

wave-dominated deformation, comprising cavity and spall formation as illustrated in Fig. 5.1(b). In the following, we demonstrate how the addition of a second pulse alters the observed deformation by excitation of a second shock-wave and added plasma recoil pressure applied by an expanding plasma. We discuss the increased complexity in observed deformation, and as a main observation find that the spall-front velocity—i.e. the velocity of the furthest reaching part of the detached layer, which we from hereon refer to as simply the spall velocity—displays a sharp reduction as a function of interpulse spacing. We attribute this reduction to the presence of plasma pressure induced by the second pulse, which slows down the spall layer near the moment of release (see Fig. 5.1(b)). We perform radiation-hydrodynamics simulations to gain a better understanding of the proposed spall-velocity-reduction mechanism and have investigated the influence of the energy of the second pulse.

5.2. Experiment & Methods

In the experiment, a stream of liquid tin is expelled from a nozzle mounted vertically on top of a vacuum chamber ($\simeq 10^{-7}$ mbar). A modulation applied to the nozzle leads to a controlled breakup of the tin stream into equal-sized droplets traveling downward at approximately 10 m/s. By varying the frequency of the modulation we tune the droplet diameter d from 19 to 52 µm. The droplets then pass a light sheet prepared above the center of the vacuum vessel and scatter some of the light. This scattered light is detected by a photomultiplier tube and is used to trigger the drive laser and data acquisition at a 10 Hz repetition rate.

Two temporally Gaussian-shaped laser pulses with a full width at half maximum (FWHM) duration of 0.4 ns, wavelength $\lambda = 1064$ nm, and energies E_1 and E_2 of 20 mJ per pulse ($E_1 = E_2$) are incident on the droplet as illustrated in Fig. 5.1(a). The pulse pair generation is automated using the arbitrary pulse shaping capability of the drive laser presented in Chap. 2 [42]. Combined with a straightforward feedback algorithm it allows for a convenient, accurate, and fully electronic tuning of the pulse amplitudes and spacing. The spacing between the two pulses Δt is scanned up to 100 ns with a minimum possible step size of 0.4 ns. The laser beam,

with a circular polarization, is focused to a Gaussian spot of approximately 125 µm FWHM at the position of the droplet.

The droplet is backlit using an incoherent laser pulse with $\lambda \approx 560$ nm and the shadow created by the droplet is imaged onto a camera using a long distance microscope. The spatial and temporal resolution of this *shadowgraphy* setup positioned perpendicularly to the laser propagation axis are approximately 5 µm and 5 ns, respectively. A recording of the droplet deformation is obtained by repeating the experiment while scanning the back-lighting laser pulse in time with respect to the drive laser in steps of 50 ns. For more about the experimental setup see Sec. 1.5.

5.3. Target morphology

An extensive overview of the observed deformation is given in Fig. 5.2. For each droplet diameter d (ranging from 19 to 52 µm) a selection of Δt is made to best illustrate the trends in deformation in the relevant range. First, looking at the single-pulse images for increasing d (Fig. 5.2, top row), the most notable effect is a change in the ratio between the size of the main cavitation bubble and the spall. For this shock-wave deformation regime an asymptotic hydrodynamic similarity (of the internal pressure evolution) is shown to exist when the total deposited energy (Q_{tot}) per droplet volume Q_{tot}/d^3 is kept constant [39]. This similarity is supported by the observed collapse of the radial expansion velocities of the main central cavitation bubble presented in Refs. [37, 82]. Since, in this work, the laser focal spot size and laser energy are kept constant throughout the experiment, both the energy impinging on the droplet E_{od} as well as the droplet volume vary significantly when changing d. Therefore, assuming that $Q_{\mathrm{tot}} \propto E_{\mathrm{od}}$, similarity (as presented in Ref. [39]) does not hold in our case. Since E_{od}/d^3 decreases with increasing d we see in Fig. 5.2 a corresponding decrease in the size of the central cavitation bubble and spall.

5.3.1. The effects of interpulse spacing Δt

With the introduction of a second laser pulse we observe several changes in the target morphology that strongly depend on Δt. First, we see a flattening of the laser facing surface due to the second pressure kick. An increase in the size of the visible plasma cloud suggests that this pressure is partly supplied by a reheating of the plasma initially generated by the first pulse. Remarkably, effects of the second pressure kick on the transverse (vertical) size of the main expanding body, and hence the expansion velocity, are minor. In other words, although with the addition of a second pulse extensive flattening is present leading to a considerably different shape, the radial size is similar to the single pulse case (see, for example Fig. 5.2(a), $\Delta t = 11.8$ ns). Second, a strong jetting behavior is observed, most clearly visible in Fig. 5.2(a). The origin of the microjets and the observed trends are qualitatively discussed in Sec. 5.6. Finally, clear changes in the spall are apparent. From Fig. 5.2 it is already clear that for all droplet sizes, an initial increase in the spall velocity with increasing Δt is followed by a strong decrease. Furthermore, for the largest

two droplet sizes we observe a second spall-like front following the initial spall. The increased droplet size reduces Q_{tot}/d^3 and results in a reduced amplitude of the shock wave and trailing rarefaction wave. This in turn means that the region where the maximum negative pressure exceeds the tensile strength of the liquid is reduced, and therefore the region of vapor void formation, i.e. the central cavity, will be smaller and expands at a reduced rate. A relatively small cavity size at early times and its reduced expansion rate can allow for a second shock wave to pass, enabling it to generate the second spall front in a similar manner to the generation of the first. The observation of this second spall event is considered evidence of the existence of a second shock wave launched by the impact event of the second pulse. A larger cavity size, which is attained at large Δt, or by decreasing d (and thus increasing Q_{tot}/d^3), likely blocks passage of the second shock wave and prevents a second spall from being formed. Indeed, for the smaller droplet sizes, the second spall is absent.

At small Δt the close proximity of the two shock waves can lead to more complicated dynamics and we presume an exceedingly complex pressure wave evolution is likely hidden inside the droplet interior. Even at $\Delta t = 1\,\mathrm{ns}$ we find that the resulting deformation is profoundly different from the case of a single pulse with a combined energy. We can identify several deformation features that suggest a joint influence of both shock waves on the central cavitation and spall formation. These include the increased radial extent of the central cavity clearly visible in Fig. 5.2(a) at $\Delta t = 1.0\,\mathrm{ns}$ and $1.4\,\mathrm{ns}$ and in Figs. 5.2(b,c) at $\Delta t = 1.0\,\mathrm{ns}$. Further indications are the notable changes in spall morphology and an increase of the spall velocity for all d in the first few Δt. As will be shown later, the impact of the second pulse leads to a significant plasma pressure even at the back side of the droplet. This will generate counterpropagating shock waves in the droplet that may interfere with the shock wave initiated by the first pulse, thereby complicating the internal pressure distributions and the spall formation further. A full explanation of all observations presented in Fig. 5.2 is beyond the scope of the current work and would require complex dedicated simulations incorporating both accurate fluid and plasma modeling with improved knowledge of the equation of state and spall strength of liquid tin [83, 87, 113].

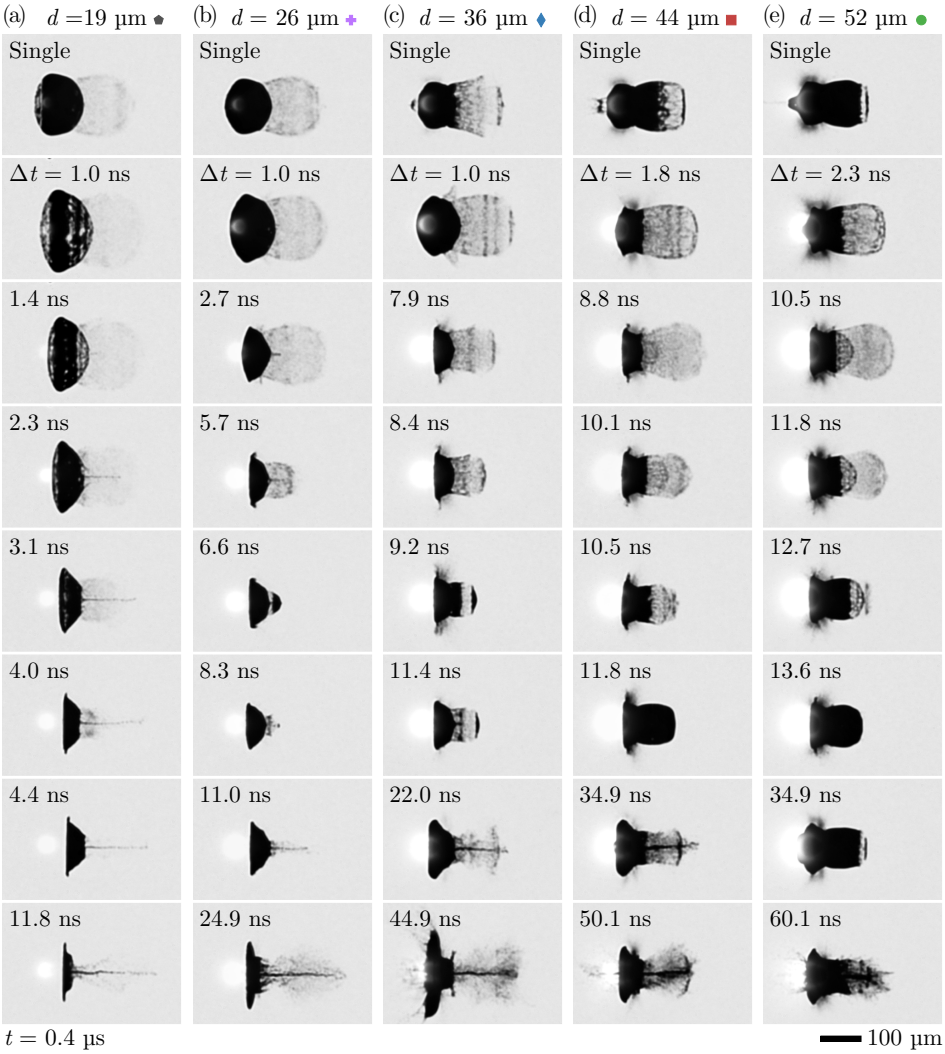

Figure 5.2: Side-view shadowgram overview of the observed deformation. Two laser pulses, each with a duration of 0.4 ns, and energy of 20 mJ, are incident from the left, focused down to a Gaussian spot with a full width at half maximum of 125 µm, and spaced by a time delay Δt. All shadowgrams are recorded $t = 0.4$ µs after impact of the first laser pulse. From left to right, columns (a-e) show the different droplet sizes (with diameter d). The rows show increasing values of Δt, independently chosen per droplet size to best illustrate the observed trends in deformation. The bright spot is plasma emission, which, although it has a duration similar to the laser pulse ($\sim$ ns), is visible due to the long exposure time of the CCD camera ($\sim$ ms).

5.4. The spall velocity

By tracking the spall front throughout the side-view shadowgraphy image sequence we obtain its trajectory (see also Fig. 3.2). At the laser energies used we find the spall-front trajectories (before and after fragmentation) to be fully ballistic and not significantly hampered by surface tension. The spall velocity, which we denote u_s, is therefore straightforwardly obtained using a linear fit and a presentation of the spall-front position as a function of shadowgraphy time delay is omitted. The obtained u_s for different droplet diameters as a function of the interpulse delay Δt is shown in Fig. 5.3.

The obtained spall velocities for single pulses range from approximately 300 to 600 m/s and can be used to estimate the peak pressure of the shock wave when it arrives at the back side of the droplet, i.e. during spall formation. This is done using the velocity doubling rule, which states $u_f = 2u_m$ [114], where u_f is the velocity of the free surface (the droplet surface) and u_m is the material velocity (for a brief derivation, see also the supplementary information of Ref. [84]). The material velocity u_m is related to the pressure P by $P = u_m \rho_0 c_s$ [84, 114], with $\rho_0 = 7 \times 10^3\,\mathrm{kg\,m^{-3}}$ the density of liquid tin [115], and c_s the shock velocity. When approximating c_s by the speed of sound in liquid tin ($2.5\,\mathrm{km\,s^{-1}}$ [116]) we find that the pressure of the wave when reaching the back side of the droplet ranges from approximately 2 to 5 GPa in our experiment. Similar peak pressures at the back side of the droplet and more detailed analyses of the shock wave pressure evolution through its propagation have been reported in Refs. [36, 39, 83].

In the above estimate of the shock pressure we have to consider that, due to our limited temporal and spatial resolution, we are unable to resolve the early-time (< 10 ns) dynamics of the free surface [84, 111, 117] that, in a rather simplified picture, result from reflections between the spall plane (the ruptured region) and said free surface. The spall 'release' velocity u_s as measured is lower than the relevant free surface velocity u_f at first arrival of the shock wave, but approaches u_f for higher u_s [84]. For this reason an estimate of P obtained from the spall velocity u_s might be more accurate for the larger velocities. Nevertheless, following the above, and since $c_s > c$, the deduced pressure should be considered a lower bound estimate.

5.4.1. The effects of interpulse spacing Δt

For all droplet sizes we can identify a clear, rather sudden reduction in u_s when increasing Δt as shown in Fig. 5.3. This reduction shifts to earlier times with decreasing d. The behavior of the spall velocity before and after this reduction differs slightly per droplet size. For $d = 19\,\mu$m, a reduction in u_s is observed after a short plateau. Due to the strong jetting behavior the spall velocity cannot be tracked beyond $\Delta t = 4$ ns. For $d = 26\,\mu$m, we observe a similar general trend, but since the jet velocity is reduced, we can track u_s until a plateau is reached, completing a transition before tracking of the spall is impeded. For $d = 36, 44$, and $52\,\mu$m the reduction is preceded by a minor increase, and after the reduction a recovery to the original single-pulse spall velocity is present. For $d = 36\,\mu$m, the recovery happens

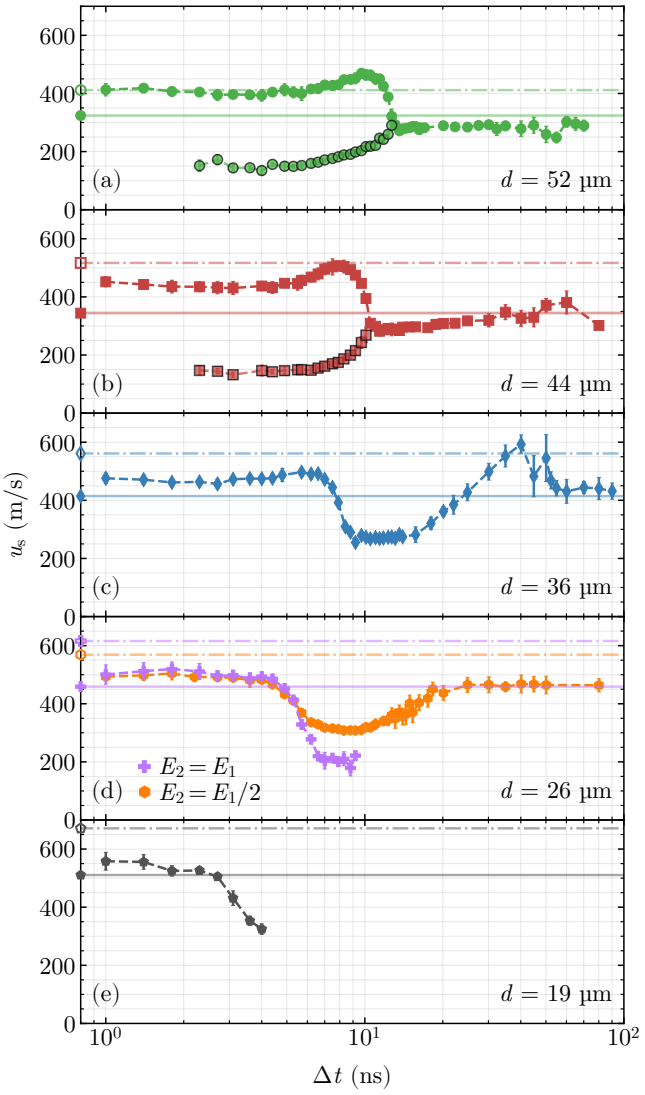

Figure 5.3: Spall velocities u_s for all droplet sizes as a function of interpulse delay Δt. The solid line corresponds to the spall velocity observed following impact of a single pulse with an energy equal to only the first pulse (E_1). The dash-dot line corresponds to the spall velocity after impact of a single pulse with the combined energy ($E_1 + E_2$). The markers with a black outline in (a) and (b) are the velocities of the second (inner) spall.

after an increase, possibly due to plasma propulsion of the spall front as the plasma expands behind it. From Fig. 5.2, it is also clear that at these relatively large Δt the original spall front is strongly disrupted and the tracking accuracy is compromised. Finally, for $d = 44$ and $52\,\mu\text{m}$, we observe a second spall front whose velocity is indicated by the dark edged markers in Fig. 5.3. The velocity of this inner spall starts low and increases towards the transition point at which it 'merges' with the outer spall.

To exclude a strong dependence of the observed transition time on E_2 an extra measurement is performed for $d = 26\,\mu\text{m}$ in which $E_2 = E_1/2$ instead of $E_2 = E_1$ (see Fig. 5.3(d)). Comparing the two cases we see that the moment of transition shows no significant shift. Furthermore, reducing E_2 leads to a less-prominent reduction in u_s (down to $300\,\text{m/s}$ instead of $200\,\text{m/s}$), and to a less prominent jetting behavior. As a result of the lower jet velocities we can completely track the recovery of u_s to the single pulse value.

5.4.2. Spall-velocity-reduction mechanism

An interference of the two shock waves might initially be suspected as the cause of the observed behavior in u_s. However, two main experimental observations make this explanation highly unlikely.

First, the spall plane, i.e. the location at which fracture of the liquid takes place, is expected to be positioned relatively close to the droplet surface. Although its exact location is unknown in our experiment and changes with d, based on available simulation work [39, 83] we expect it to form at a typical depth $\sim d/20$. The early fragmentation of the spall layer during its expansion as observed in the experiment also hints at a similar initial thickness range. This "shallow" depth of the spall fracture plane combined with the relevant times obtained from the experiment, would imply extremely high velocities of the second shock wave to be able to have it "catch up" and interfere with the first. For example, for the $52\,\mu\text{m}$-diameter droplet the observed decrease of u_s happens at $\Delta t \approx 12\,\text{ns}$. If we take conservative values and assume a spall fracture plane depth of $d/10$ and approximate the first shock-wave velocity with the speed of sound c of $2500\,\text{m}\,\text{s}^{-1}$, then for the second shock wave to reach the spall plane before or at the moment it is formed, its velocity would have to be $\geq 1.72c$. If we take a propagation velocity of the first shock wave of $1.2c$, then the the velocity of the second shock wave would need to be $\geq 2.65c$. Such differences in velocity between the two shock waves cannot be explained.

Second, for the $36\,\mu\text{m}$ and $26\,\mu\text{m}$-diameter droplets the reduction of the spall velocity remains low for approximately $10\,\text{ns}$ after its initial drop. If a direct interference of the two shock waves would be the cause, we would expect it to not last longer than any possible overlap of the waves. An estimate of the width of the shock waves can be obtained from simulation. In Ref. [39] the shock waves have a typical width of no more than $0.2d$. For $d = 36\,\mu\text{m}$ the duration of overlap of two counterpropagating waves with such a width, again approximating their propagation velocity by c, would last only $0.2 \times 36\,\mu\text{m} \,/\, 2c \approx 1.4\,\text{ns}$. Considering the above we therefore turn to finding an explanation in the plasma dynamics following second pulse impact.

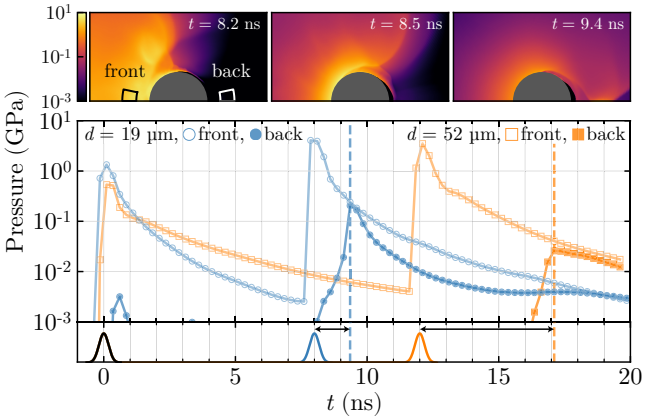

Figure 5.4: Plasma pressure evolution during double-pulse illumination as simulated using the RALEF-2D radiation-hydrodynamics code for $d = 19\,\mu m$ and $52\,\mu m$. The top hemisphere of the droplet ($d = 19\,\mu m$) is shown (top) for three selected time frames to illustrate the 'wrapping around' of the plasma pressure after impact of the second pulse. Two regions of interest, one at the front and one at the back of the droplet, are chosen. The average pressure inside both regions is plotted as a function of time t (bottom). The corresponding laser pulse sequences are shown in the attached bottom most panel, with the first pulse (black) common to both droplet sizes. For $d = 19\,\mu m$ the second pulse is incident at $t = 8\,ns$ (blue) and for $d = 52\,\mu m$ the second pulse is incident at $t = 12\,ns$ (orange).

5

5.4.3. Simulation of the plasma pressure evolution.

To gain insight into the observed spall velocity reduction mechanism, we have performed radiation-hydrodynamics simulations using the RALEF-2D code [118–120]. In recent years, this code has been employed in numerous EUV source-plasma related topics, ranging from droplet propulsion studies [93] to plasma modelling [40, 62, 121]. In our simulations, the pressure evolution within the (neutral) liquid tin droplet and the resulting deformation strongly depend on the choice of the equation-of-state model [83], and have therefore not been investigated. Instead, our main purpose is to examine the plasma dynamics resulting from the impact of the second laser pulse.

The simulations have been performed with pulse energies and an illumination geometry equivalent to the experiments for two configurations: $d = 19\,\mu m$ (with $\Delta t = 8\,ns$) and $d = 52\,\mu m$ (with $\Delta t = 12\,ns$). The results, presented in Fig. 5.4, show that after impact of the second pulse the expanding plasma 'wraps' around the droplet and a significant plasma pressure develops at the back side of the droplet (where the spall forms). It is this pressure that we attribute the reduction in u_s to when it coincides with the moment of spall formation, i.e. when the shock wave from the first pulse reaches the back side of the droplet. The plasma flow around the droplet, which results in the accumulation of a relatively dense and hot cloud on the laser axis, has previously been reported on for the case of single 10 ns duration pulses and was found to exert a noticeable backward pressure [93].

For a comprehensive verification of the proposed spall-velocity-reduction mechanism a full analysis of the pressure impulse delivered by the plasma onto the expanding spall has to be performed. The spall-fracture event itself has to be accurately modeled as well to obtain credible density and velocity distributions of the expanding spall layer. As previously mentioned, the latter is still very challenging within the current RALEF-2D code. We therefore omit such an analysis, but can however use the obtained plasma pressures to perform some 'back of the envelope' estimates. We assume that at the moment the plasma pressure forms on the back side of the droplet the spall has fully formed and consists of a single detached layer with a density equal to the original density of the droplet. Then, the problem becomes that of a simple momentum balance of a layer with a thickness Δz traveling at several 100 m/s and the pressure impulse applied by the plasma onto this layer. The magnitude of the pressure at the back side of the droplet peaks at approximately 0.2 GPa for the 19 µm droplet. A spall velocity reduction of 300 m/s due to a pressure impulse of 0.2 GPa × 0.4 ns leads to $\Delta z \approx 50$ nm, which is a plausible value given the observations.

The rapid decay of the plasma pressure (see Fig. 5.4) implies that if the second pulse is 'early', i.e. it impacts before the shock wave from the first pulse reaches the back side of the droplet, no slowing down of the spall should be present. If the second pulse is 'late', i.e. it impacts at a later moment at which the spall has already expanded significantly, the plasma is forced to expand over a larger distance and will decrease in density. This is likely to decrease the recoil pressure it exerts on the spall and allow for a recovery of u_s. Both arguments are in agreement with our observations.

Crucially, this knowledge allows us to relate the moment of spall release to the impact time of the second pulse by the observed reduction of u_s, which will be further detailed in the following section. Evidently, we need to take into account the delay between the moment of pulse impact and the pressure peak. From the simulations we observe an approximate delay of 1.4 ns and 5.1 ns for $d = 19$ µm and $d = 52$ µm respectively, and linearly interpolate this plasma expansion delay with d.

5.4.4. The shock-wave velocity

The instantaneous shock-wave velocity varies significantly during propagation from the front to the back side of the droplet due to its dependence on the shock pressure. The initial width of the shock wave directly after the ablation event is on the order of the thickness of the heated surface layer (~ 100 nm) and quickly broadens during propagation [39]. This initial broadening of the shock wave leads to a decrease of the peak pressure, followed by an increase and subsequent decrease due to the respective converging and diverging trajectories of the shock wave. Although in our experiment we certainly do not have access to the instantaneous velocity, we can determine an average shock-wave velocity from the spall release moment, assuming that the spall formation time is small compared to the total propagation time of the shock wave.

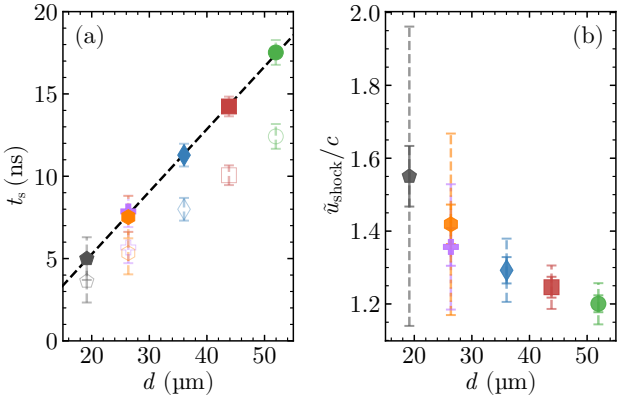

Figure 5.5: (a) Spall release moment t_s (filled markers) as a function of droplet size d. Open markers correspond to the moment of reduction of u_s, as determined by an error-function fit to the data presented in Fig. 5.3, without the added plasma-delay correction. Error bars indicate the 1σ width of the error function fit and are used as weights in the presented fit of a linear curve. The fit parameter standard errors of t_s are smaller than the markers. (b) The average shock-wave velocity $\tilde{u}_{shock} = d/t_s$ normalized to the speed of sound c. The outer (dashed) error bars correspond to the propagated error shown in (a). The inner (solid) error bars correspond to the propagated fit standard error. The error in droplet diameter is estimated to be $\pm 1\,\mu m$.

5

To obtain the spall release moments t_s, we first determine the half-way position of the transition, i.e. the reduction in u_s, and its width by locally fitting an error function to the data shown in Fig. 5.3. The results of these fits are indicated in Fig. 5.5(a) by the open markers. For $d = 19\,\mu m$, where the transition is not complete, a broad estimated range for the value of the plateau after the reduction is taken from 100 to 300 m/s for the fitting. The corresponding spread in the obtained value of t_s is reflected in the error bar. The 'real' spall release moment t_s is subsequently determined by adding the previously-mentioned plasma pressure delay time and is plotted in Fig. 5.5(a) using filled markers. We find a linear dependence of t_s, and by a least-squares fit to the data obtain a slope of 0.38(1) ns/µm and an intercept of $-2.3(2)$ ns.

The linear dependence $t_s \propto d$ suggests a single common average shock-wave velocity for all d. However, because E_{od}/d^3 varies with droplet size, the aforementioned hydrodynamic similarity [39] does not hold and we expect a dependency of the average shock-wave velocity on d. The observed offset of the fit is also not in agreement with a single velocity, since in that case we do not expect an offset, i.e. $\lim_{d\to 0}(t_s \to 0)$. We therefore rationalize that the obtained slope should approach the asymptotic velocity of the pressure wave, i.e. the speed of sound c, and obtain a velocity $u_a = 1/0.38(1) = 2.63(4)$ km/s, which, taking $c = 2.47$ km/s [116], indeed corresponds to $u_a/c = 1.07(2) > 1$.

Since we expect a different shock velocity for each droplet size, it is sensible to treat them independently and obtain an average shock velocity $\tilde{u}_{shock} = d/t_s$ per droplet size as shown in Fig. 5.5(b). The negative intercept in Fig. 5.5(a) entails an increasing $\tilde{u}_{shock}$ with decreasing d as expected by the increasing Q_{tot}/d^3.

The obtained values for $\tilde{u}_{\mathrm{shock}}$, ranging from approximately $1.6c$ to $1.2c$ for the smallest and largest droplet, respectively, are comparable to the $1.25c$ we deduce from Ref. [39]. In Fig. 5.5(b) two error bars are plotted for each data point. The inner (solid) error bar corresponds to the propagated combined standard error of the relevant fit parameter and the estimated error in the droplet size of $\pm 1\,\mu\mathrm{m}$. In Fig. 5.5(a), this error is smaller than the marker size. For the larger (dashed) error bars the 1σ width of the error function fit representing the transition width (which is the error bar shown in Fig. 5.5(a)) is included. The inclusion of this error displays the relevance of the choice of t_{s} which we set here at the half-way (50%) point. Figure 5.5(b) shows that the accuracy with which $\tilde{u}_{\mathrm{shock}}$ can be retrieved using this method is inherently limited for smaller droplet sizes without additional assumptions or modeling to motivate a better choice of t_{s} along the u_{s} curve. Also, for small d, the one-way propagation time of the shock wave (estimated by t_{s}) approaches the pulse duration (0.4 ns) and the hydrodynamic timescale of the plasma expansion, and possibly also the spall formation duration. Nevertheless, the error in $\tilde{u}_{\mathrm{shock}}$ for the 44 and 52 µm droplets is below 10%. Therefore, the observed $\tilde{u}_{\mathrm{shock}}$ may serve as a validation of the equation of state (and the shock parameter therein) as used in detailed simulations [39, 83].

5.5. The effects of the second pulse energy

For the case $d = 26\,\mu\mathrm{m}$, we perform two measurement series in which E_2 is varied at a fixed Δt. One Δt value is chosen on either side of the spall velocity transition, specifically at 3.6 and 7.6 ns. The results are shown in Fig. 5.6. At $\Delta t = 3.6\,\mathrm{ns}$, before the transition, the spall velocity (top) undergoes a gradual minor increase. Inversely, in agreement with the proposed spall velocity reduction mechanism, u_{s} displays a strong decrease with increasing E_2 at $\Delta t = 7.9\,\mathrm{ns}$.

When increasing E_2 beyond E_1 we observe a strong difference in the transverse expansion velocities, quantified at early times and plotted in Fig. 5.6(a, bottom). Up to $E_2 = E_1$ the initial expansion velocity $\dot{R}(t = 0)$ is rather flat and equal for both values of Δt. When $E_2 > E_1$ a separation of the two cases takes place, most notably driven by an increase of expansion when $\Delta t = 3.6\,\mathrm{ns}$. From the accompanying shadowgrams (see Fig. 5.6(b)), it appears that this increased expansion is driven by additional cavitation induced by the second pulse.

Although a full picture of the pressure evolution in the droplet interior is likely needed to reveal the origin of this increased expansion, we speculate that when $E_2 > E_1$, the shock wave induced by the second pulse can be larger in amplitude than the first and will lead to cavitation at a slightly earlier point during its converging trajectory towards the droplet center. Additionally, at $\Delta t = 3.6\,\mathrm{ns}$ the cavity induced by the first pulse is either very small or still in the formation phase [39, 84]. It is therefore possible that two cavitation regions are formed independently which merge at an early time during their expansion. In line with this reasoning we see that no jet is formed in this case. Furthermore, since no strong increase in u_{s} is present, we have gained access to a target shape (see Fig. 5.6(b)(*)) distinct from any single pulse case in its ratio between radial expansion and spall velocities. Compared to

$\Delta t = 3.6\,\text{ns}$, with $\Delta t = 7.9\,\text{ns}$, no such increase in the initial expansion velocity due to additional cavitation (spherical expansion) is observed when $E_2 > E_1$. Instead, increasing E_2 leads to increased flattening and jetting. An advanced growth of the cavity from the first pulse at $\Delta t = 7.9\,\text{ns}$ compared to $\Delta t = 3.6\,\text{ns}$ will impede any additional cavitation by the second pulse as the shock wave will simply impact the cavity. This again allows for the formation of a jet and flattening assisted by the additional plasma pressure.

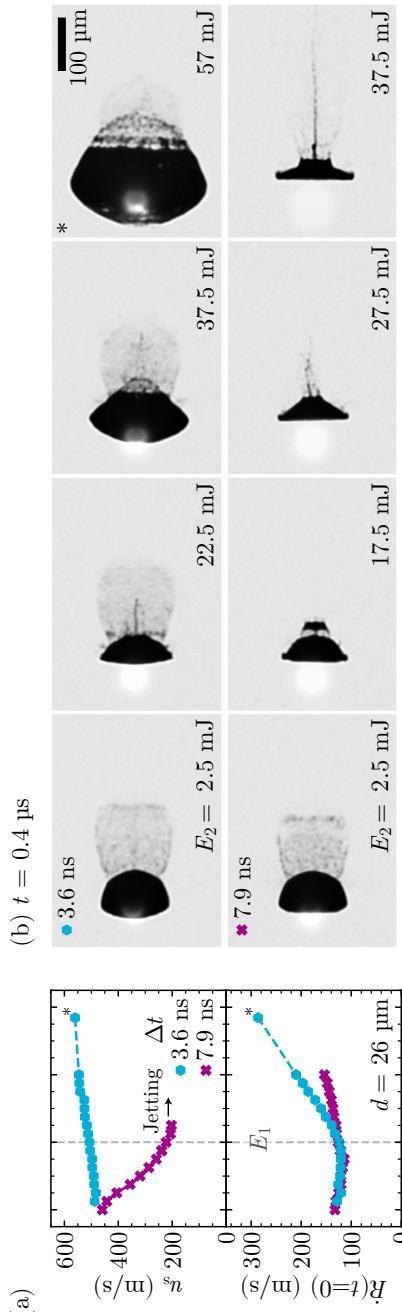

Figure 5.6: (a) Effect of E_2 on the spall velocity u_s and initial expansion velocity $\dot{R}(t = 0)$ for interpulse delay (Δt) values of 3.6 and 7.9 ns. (b) Shadowgrams accompanying data in (a), with the top and bottom rows showing images for $\Delta t = 3.6$ ns and $\Delta t = 7.9$ ns, respectively. Columns show increasing E_2 from left to right with values chosen such that the deformation trend for each case of Δt is demonstrated best. The images are recorded 0.4 µs after laser impact. Data points and shadowgram of a particular target of interest, as mentioned in the main text, are indicated by the symbol *.

5.6. Jetting

Jet formation is a prevalent phenomenon resulting from the non-spherical collapse of an embedded cavity [102, 105, 122–124]. Besides an already present asymmetry in the cavity surroundings, e.g. a hard surface, or a free surface, a passing pressure field or shock wave can induce a similar type of jetting [103, 104, 125–132]. In the case of laser impact on microdroplets the formation of a jet on the principal symmetry axis (i.e. the laser propagation axis) has been observed in multiple studies [77, 98, 100, 101, 133] and has in most cases been attributed to the collapse of an internal cavity. We can say in all likelihood, that the jets we observe in Fig. 5.2 and Fig. 5.6(b) originate from a (partial) collapse of the cavity formed by the first pulse. Here, the shock wave generated by the second pulse is likely responsible for initiating the jetting when it impacts the cavity, possibly in a way very similar to the mechanism of shaped charges [101, 134]. The presence of jets in single pulse cases with pulse durations similar to the acoustic timescale (R_0/c) [77] (see also Chap. 4) suggests that the pressure field and deformation resulting from impact of longer pulses can function similarly.

Although a detailed quantification of the jetting dynamics is outside the scope of this work, a clear dependence of the jet velocity with pulse spacing Δt is present (see Fig. 5.2(a)). It has been shown that the velocity of a jet formed by shock-wave impact on a cavity depends on the initial size of the cavity and the phase of the bubble oscillation [103, 125, 132, 135]. It is therefore straightforward to conclude that the jet velocity increases with Δt due to the cavity expansion dynamics. The magnitude of the pressure wave inducing the collapse of the cavity and the accompanying jetting is also likely to play a role in the jet velocity, as supported by the increase in jet length visible in Fig. 5.6(b)(7.9 ns). Since the absorbed laser energy fraction may also exhibit a (positive) Δt dependence due to the expansion of the plasma cloud, separating the effects of laser pulse energy and Δt on the jet velocity remains challenging.

Accurate tracking of the jet velocity in the current experiments is, in many cases, hampered by the presence of the spall. It either blocks the jet optically, making it impossible to visualize, or it physically blocks the jet in its path when the jet overtakes the spall causing a disruption of the jet. Therefore, a further study with an in-depth quantification would benefit from different experimental conditions and is left for future work. Considerations for a follow-up study could comprise a lower E_1/d^3 value, below the spallation but above the cavitation threshold [37, 39, 81], which would prevent spallation from occurring. Another possibility is having a higher E_1/d^3, which would increase the spall velocity and decrease the spall fragmentation time, and thereby improve visibility of the jet. An increased E_1/d^3 can possibly be combined with a lowered E_2 value to decrease the jet velocity and prevent interaction between the jet and (faster) spall.

5.7. Conclusions

In conclusion, we have studied the deformation of tin microdroplets after irradiation by a pulse pair with pulses of 0.4 ns in duration with varying interpulse time delay. As in the single pulse case, we observe the formation of an expanding central cavity and a spall layer, both induced by a shock wave and the accompanying rarefaction wave traversing the droplet. The addition of a second pulse predominantly leads to flattening, jetting, and changes in the spall velocity, all dependent on the interpulse spacing. More specifically, we find a sharp reduction in the spall velocity at a specific droplet-size-dependent pulse spacing. We attribute this reduction to a deceleration of the spall by the plasma pressure resulting from the impact of the second pulse.

Simulations performed with the radiation-hydrodynamics code RALEF-2D confirm that a significant plasma pressure is able to develop at the surface undergoing spallation. By combining the results from experiment and simulation we are able to estimate the moment of spall formation, i.e. the arrival time of the shock wave at the back side of the droplet. We find average shock-wave propagation velocities ranging 1.2 to 1.6 times the speed of sound.

We have discussed the effects of the relative energy of the second pulse at two fixed pulse delays on the various processes involved. We find that when the energy of the second pulse exceeds the first, the central cavity formation is altered, enhancing the transverse expansion of the final target without increasing the spall velocity.

Lastly, we observe microjets originating from the droplet center induced by the impact of the second pulse and find that the jet velocity increases with both an increase in interpulse spacing as well as the energy of the second pulse. The observed jetting and cavitation phenomena show strong resemblance to many cavitation and jetting studies in available literature on transparent liquids, and provide an outlook to study the jet formation and behavior resulting from the interaction of in-droplet-embedded vapor cavities with pressure waves.

Combined, our findings provide valuable insights into the complex processes resulting from laser impact on liquid tin microdroplets, enabling, e.g. a manipulation of the target expansion and spall characteristics using a double-pulse sequence. The present work further benefits the design of more advanced target-shaping pulse sequences in next-generation droplet-based extreme ultraviolet sources.

Chapter 6

Laser Ablation Threshold of Liquid Tin Microdroplets

The laser ablation threshold is an important parameter that governs the response of materials to intense laser irradiation. Here we study the laser ablation threshold of liquid tin by irradiation of microdroplets with temporally flat laser pulses of nanosecond duration at 1064 nm wavelength. The main observable is the temporally resolved reflection from the droplet surface. The reflection exhibits a sharp and strong decrease in magnitude at a specific moment dependent on the laser intensity. This moment marks the generation of a plasma that strongly absorbs the following incident laser light, rapidly expands, and thereby sets in motion the remainder of the liquid droplet. We find an inverse-square dependence of this plasma-onset time as a function of laser intensity and attribute this scaling to the presence of one-dimensional heat diffusion during irradiation. This scaling and its one-dimensional thermal origin has been strongly established in literature and follows from a square-root scaling of the thermal diffusion depth with time. Our experiment unambiguously shows that this scaling law holds for our specific case of laser impact on tin microdroplets. The results presented in this chapter are of particular interest to target preparation and metrology in extreme-ultraviolet sources utilizing tin microdroplet targets.

6.1. Introduction

Pulsed laser ablation of metals using laser pulses with durations in the nanosecond regime is of interest to a wide range of applications such as micromachining [136], pulsed laser deposition (PLD) [137], optical material design [138], and laser-induced breakdown spectroscopy (LIBS) [139]. A detailed understanding of laser ablation is also of value within the context of extreme-ultraviolet (EUV) light sources used in state-of-the-art nanolithography devices. Such EUV sources make use of mass-limited tin-droplet targets in a multi-pulse scheme [14].

Although the ablation of liquid tin microdroplets is well understood in a steady-state regime above the plasma formation threshold, accurate modeling appears challenging close to the threshold [93], indicative of a lack of understanding of this highly transient ablation regime. Experimental investigations into the ablation threshold and ablation mechanics may therefore be of value to advance our understanding of laser-droplet interaction, and be of significant benefit to EUV source development in the context of droplet deformation, debris mitigation, and metrology. Furthermore, accurate knowledge of ablation thresholds and an understanding of the possibility of phase explosion is valuable in the context of advanced target preparation, where laser vaporization of the liquid tin below the plasma formation threshold can possibly be used to generate low-density vapor targets as shown in Chapter 7.

In this chapter we therefore study the laser ablation (breakdown) threshold of liquid tin microdroplets by making use of time-resolved measurements of the surface reflection. A strong abrupt decrease in the reflection from square (constant intensity) laser pulses indicates a moment of plasma onset and the coinciding inception of inverse bremsstrahlung. We study the plasma-onset time as a function of laser pulse duration and energy, and correlate the reflection signal with target deformation recorded using shadowgraphy imaging.

6.2. Experiment & Methods

A schematic illustration of the experiment is depicted in Fig. 6.1(a). We irradiate the tin microdroplets (99.995% purity), 30 µm in diameter, in a vacuum environment with pulses from an Nd:YAG-nanosecond-laser system. The laser system (see Chap. 2)[42], operating at 1064 nm wavelength, is programmed to output flat-intensity pulses with a duration ranging from 100 ns to 400 ns and rise times of approximately 200 ps. The Gaussian focal spot has a full width at half maximum (FWHM) of 84 µm at the location of the droplet. A photodiode (PD) (Thorlabs DET08) is mounted on the vacuum chamber at a 21.1° angle with respect to the principal laser axis and detects the laser light reflected from the droplet. To increase the signal on the PD V_{PD} and block any broadband emission from the plasma, a lens and laser-line filter are mounted ahead of the PD, respectively. Since V_{PD} ranges from approximately 100 µV to a few mV, 720 pulses are recorded and averaged to improve the signal-to-noise ratio.

The droplets are imaged using a shadowgraphy system aligned perpendicularly to the principal laser axis, providing a side view. The system consists of a CCD

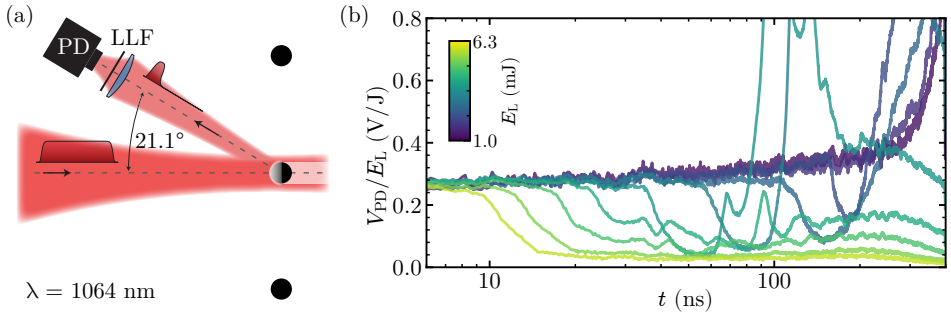

Figure 6.1: (a) Illustration of the experiment. A flat-intensity pulse is incident on the tin droplet and the reflection is detected by a photodiode (PD)(Thorlabs DET08) at 21.1° with respect to the principal laser axis. Upstream from the photodiode a lens is used to increase the total light collection, and a 1064 nm laser-line filter (LLF) blocks the broadband plasma emission. (b) Reflection signal as a function of time t from a 400-ns-flat-intensity pulse of varying laser pulse energy E_L incident on the droplet. The output voltage of the photodiode V_{PD} is normalized by E_L.

camera coupled to a long-distance microscope, and makes use of incoherent-pulsed backlighting with a wavelength of 560 nm. We obtain a spatial and temporal resolution of approximately 5 µm and 5 ns respectively. More information on the experimental setup can be found in Sec. 1.5 and Refs. [32, 93].

6.3. Time-resolved reflection and its correlation with deformation

Figure 6.1(b) shows the time-resolved reflection signals obtained for the case of a 400 ns laser pulse with energies E_L ranging from 1 mJ to 6.3 mJ. For all energies, the reflection from the droplet initially accurately follows the flat input pulse. At a certain point in time the reflection deviates, displaying a strong decrease for all values of E_L except the lowest two, for which only a gradual increase in reflected light is observed. We attribute the decrease in reflectivity to the generation of a plasma layer that efficiently absorbs the incident laser light [140] and therefore label the moment at which this occurs as the plasma onset time t_{on}. Studies on the reflection of metals at varying laser fluence [141–143], in agreement with our observations shown in Fig. 6.1(b), show no significant change in reflectivity before the plasma-formation threshold is reached and a strong decrease after.

After the initial decrease ($t > t_{on}$) the majority of the measurements show an increase in reflection. This increase appears to be caused by a hydrodynamic deformation of the droplet initiated by the rapidly expanding plasma [32]. In Fig. 6.2, shadowgrams of the droplet are compared to the reflection signal for the case of a 200 ns pulse. We observe a clear correlation between the decrease in reflection intensity and the first observable deformation which reproducibly originates from the droplet pole. This deformation is significant during the remainder of the laser pulse and influences the observed reflection signal. When plasma generation is minimal it

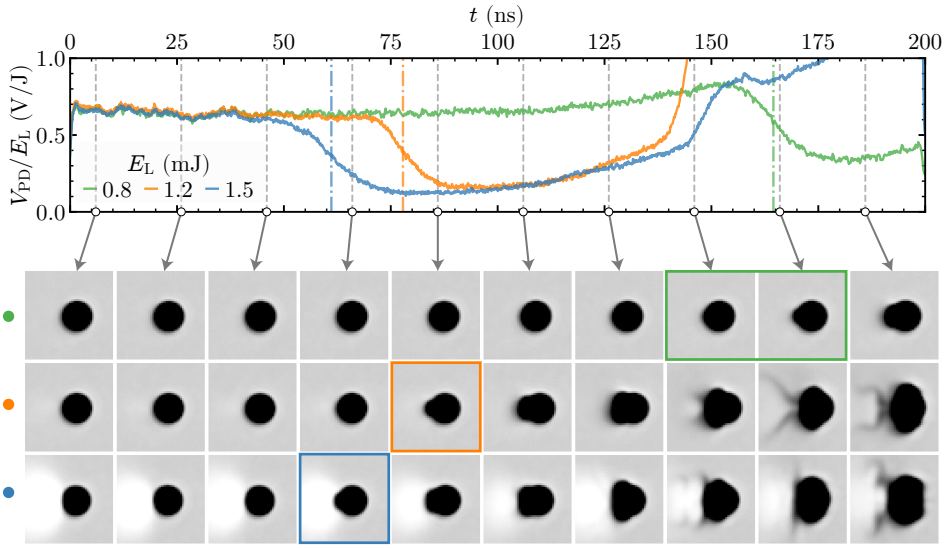

Figure 6.2: Comparison between the obtained reflection signal (top) and the side-view shadowgraphy images (bottom) for three cases. The rows of shadowgraphy images are ordered with increasing energy from top to bottom. The first observable deformation for each row is indicated by the outlined image(s). The determined t_{on} (at 50% of the decrease in V_{PD}/E_L) is indicated by the vertical dash-dotted lines. For the 2.2 mJ case (bottom row) clear overexposure of the camera by emission from the plasma cloud is visible. Due to the relatively long exposure time of the camera (on the order of milliseconds) this emission is recorded in all frames and thus not temporally resolved. The laser pulse is incident from the left and the droplet diameter is 30 µm.

is very likely that the deformed surface will occasionally, with a significant shot-to-shot deviation, direct additional light towards the photodiode. We also observe that the increased reflection at times $t > t_{on}$ is highly irregular, (see Fig. 6.1(b)) which also hints at it originating from the somewhat volatile deformation. When E_L is increased the increase in reflection following t_{on} is suppressed and reflection remains low (for example in Fig. 6.1(b), 6.3 mJ). In these cases, plasma emission also largely or fully obscures local deformation on the shadowgraphy images (not shown). Both observations hint towards a full shielding of the droplet surface by the plasma. In Appx. 6.A we present a brief quantification of the reduction in reflectivity in the full plasma shielding case alongside extra detail of the chaotic behavior of the reflection in the non-fully shielded case.

6.4. Dependence of the plasma-onset time on laser intensity

The plasma-onset time t_{on} is quantified by fitting a Gaussian distribution to the gradient of the reflection drop (as visible in Fig. 6.1(b) and Fig. 6.2). This provides an accurate center value of t_{on} as well as a standard-deviation width which we take to represent the absolute error. Since the observed deformation following plasma

onset originates on the droplet pole, we take as the relevant laser intensity I the peak value on the droplet pole. We determine I using a camera recording of the focal spot and the laser pulse energy E_{L}. The resulting dependency of t_{on} on I is presented in Fig. 6.3(a) for all pulse durations studied in this work. We observe a clear inverse-square dependence and therefore write

$$t_{\mathrm{on}} = K_{\mathrm{I}} I^{-2}. \tag{6.1}$$

A least-squares fit of Eq. (6.1) to the full dataset, with the error in t_{on} taken as weights, results in $K_{\mathrm{I}} = 3.40(5) \times 10^8\,\mathrm{s\,W^2/cm^4}$. To obtain an absolute accuracy we need to include the typical 5% calibration error in the laser intensity measurement (indicated by the horizontal error bars) resulting in $K_{\mathrm{I}} = 3.4(4) \times 10^8\,\mathrm{s\,W^2/cm^4}$. Note that three extra data points, recorded with a larger droplet size of 40 µm, are in full agreement with the data taken with 30 µm droplets. This agreement indicates no significant contribution of the droplet size on the observed intensity dependence (Eq. (6.1)).

The two pulses with the lowest intensities studied in this work are the lowest energy cases with a 400 ns duration. For those two cases, we only observe a gradual increase in reflection at the end of the pulse, and no decrease as shown in Fig. 6.1. Regardless of the precise details of the ablation process in this regime and the existence of an equivalent t_{on}, since we observe no decrease we cannot determine a value for t_{on} in a similar fashion. Therefore, we have indicated the bounds of this regime in Fig. 6.3 with the grey shaded regions, and consider it out of reach with our current method.

Early work [144] on the heating and evaporation of strongly absorbing media by laser irradiation predicted the scaling relation given by Eq. (6.1). Since the pulse duration is much longer than the electron-ion relaxation time, i.e. $\tau_{\mathrm{p}} \gg \tau_{\mathrm{e\text{-}i}}$, the electrons and ions in the liquid are in thermodynamic equilibrium and we can consider a gradual surface heating of the material by the incident laser pulse [145]. Assuming one-dimensional heat diffusion, the energy deposited through absorption of laser radiation AIt, with A the absorption coefficient, is distributed in a layer of thickness l, which grows following [146]

$$l \propto \sqrt{\kappa t}, \tag{6.2}$$

with κ the thermal diffusivity. Any threshold related to exceeding a certain specific internal energy in the material, given by AIt_{th}/l, is therefore reached at a time $t_{\mathrm{th}} \propto I^{-2}$ [147]. The observed scaling of t_{on} with I (Eq. (6.1)) is therefore directly explained by the above.

Since we are not dealing with a planar target but a spherical droplet, the assumption of one-dimensional heat diffusion only holds if the thermal penetration depth remains significantly smaller than the droplet size. Indeed, for the longest pulse duration of 400 ns and a thermal diffusivity of $16.4\,\mathrm{mm^2/s}$ [148], we estimate a thermal penetration depth of $l_{400} = \sqrt{\kappa \times 400\,\mathrm{ns}} \approx 2.6\,\mu\mathrm{m} \ll 30\,\mu\mathrm{m}$. This also explains why we observe equal values of t_{on} for the two droplet sizes of 30 and 40 µm.

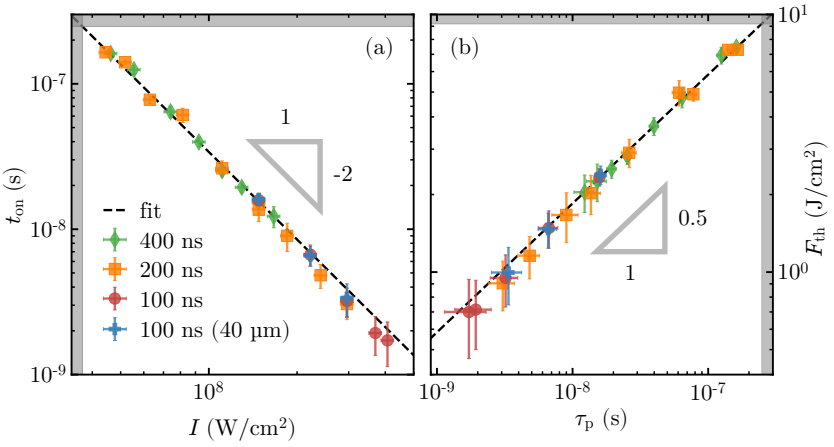

Figure 6.3: (a) Plasma-onset time t_{on} as function of laser intensity I. Dashed line is a fit of Eq. (6.1) to the concatenated data. (b) Ablation fluence threshold F_{th} as function of synthetic pulse duration $\tau_p = t_{on}$. Here, the dashed line follows Eq. (6.4) with K_I obtained from the fit of Eq. (6.1) as shown in (a). Several data points were taken at an alternate droplet size of 40 µm and are labeled as such in the legend. The grey shaded regions indicate the edge of the parameter space in reach with our current reflection-based method (see main text).

6.5. Fluence ablation threshold scaling with pulse duration

The observed scaling of $t_{on} \propto I^{-2}$ is essentially equivalent to a more commonly studied scaling of the fluence damage threshold F_{th} with pulse duration τ_p. Since $F_{th} = It_{on}$ for a pulse with a duration equal to the plasma-onset time, i.e. $\tau_p = t_{on}$, we obtain

$$F_{th} = \sqrt{K_I \tau_p}. \tag{6.3}$$

This relation is applied to the data and previous fit result, and plotted in Fig. 6.3(b). With $K_I = 3.4(4) \times 10^8\,\mathrm{s\,W^2/cm^4}$ obtained previously, the corresponding proportionality constant has a value of $\sqrt{K_I} = 1.84(10) \times 10^4\,\mathrm{J\,cm^{-2}\,s^{-1/2}}$.

The square-root dependence of the threshold fluence on the pulse duration (Eq. (6.3)) again directly follows from an equal dependence of the thermal penetration depth (Eq. (6.2)). For the case of laser-induced damage in dielectrics the square-root scaling is also well established and confirmed to hold for pulse durations down to approximately 10 ps [149–153].

A value for F_{th} is commonly estimated by considering a threshold of strong evaporation. Such a threshold can be expected to be passed when the deposited energy per unit mass ε exceeds the latent heat of evaporation $\varepsilon > \Delta H$. The fluence threshold can then be written as [147, 154, 155]

$$F_{th} = A^{-1} \rho_0 \Delta H \sqrt{\kappa \tau_p}, \tag{6.4}$$

with absorption coefficient A, density ρ_0, latent heat of vaporisation ΔH, and thermal diffusivity κ. In Ref. [32] a value of $F_{\mathrm{th},10} = 2.4(8)\,\mathrm{J\,cm^{-2}}$ was obtained from the droplet propulsion threshold for the impact of a 10 ns FWHM Gaussian pulse. An estimate using Eq. (6.4) results in $F_{\mathrm{th},10} \approx 5\,\mathrm{J\,cm^{-2}}$ [32], which, although this simple estimate comes remarkably close, does not fully agree with the threshold obtained from propulsion. For a square-shaped 10 ns pulse we here obtain $F_{\mathrm{th},10} = \sqrt{K_\mathrm{I} 10^{-8}} = 1.85(2)\,\mathrm{J\,cm^{-2}}$, which is in good agreement with the threshold obtained from propulsion. More generally we can use Eq. (6.4) to estimate K_I. Before the onset of plasma formation, absorption through inverse bremsstrahlung is negligible and we can estimate the absorption of liquid tin given its optical constants [95] and obtain $A = 0.16$ for the relevant wavelength of 1064 nm. With $\rho_0 = 7 \times 10^3\,\mathrm{kg\,m^{-3}}$ [115], $\Delta H = 2.5 \times 10^6\,\mathrm{J\,kg^{-1}}$ [156], and $\kappa = 16.4\,\mathrm{mm^2/s}$, we obtain $A^{-1}\rho_0 \Delta H \sqrt{\kappa} = 4.4\,\mathrm{J\,cm^{-2}\,s^{-1/2}}$. This value is significantly larger than what we obtain for $\sqrt{K_\mathrm{I}}$ from the fit to the data, indicating that either Eq. (6.4) does not fully accurately describe the ablation process and the observed threshold in our experiment, or that one or multiple of the constants (ρ_0, κ, ΔH, and the refractive index) available in literature are inaccurate.

6.6. Outlook

6.6.1. On the presence of phase explosion

The deformation as shown in Fig. 6.2 shows the peculiar formation of an expanding bubble-like feature on the droplet pole. The bubble grows over time and eventually appears to burst, followed by low-contrast 'streaks' indicative of a plume containing particles with sizes far below the imaging resolution of 5 µm. These observations hint at a (sub-surface) phase explosion (PE) taking place as a result of a superheating of the liquid metal to a temperature approaching the critical temperature [157–160]. In the lowest energy case of 0.8 mJ shown in Fig. 6.2 we observe a slight gradual increase in reflection and a significant bulging of the droplet surface before t_on. This suggests that PE might take place at a threshold time slightly preceding the onset of plasma formation t_on and the subsequent absorption of laser light due to inverse bremsstrahlung. An opposite order of the thresholds is unlikely as a plasma shielding effect [91, 92, 158, 161] will decrease the rate at which the droplet surface is heated by the laser pulse, thereby preventing PE from occurring. Further investigation into the presence of PE in our experiment and a possible PE threshold separate from that of plasma formation is outside the scope of this work. Such investigations would likely require additional measurements using shadowgraphy with an increased spatial resolution, possibly assisted by shadowgraphy at shorter (UV) wavelengths to improve vapor contrast, (time-of-flight) ion diagnostics [97], and time-resolved recordings and spectroscopic investigation of the plasma emission [63, 162]. Future work could confirm the possibility of applying PE as a distinct new way of initiating droplet deformation.

6.6.2. Modeling of nanosecond laser ablation

The modeling of nanosecond laser ablation [157, 163] is a considerable field of research relevant for many applications [136–139]. Dedicated models have been developed [164] to explain and predict the ablation of metals, including the ablation thresholds and mass removal rates. Such models incorporate many of the different phenomena or stages of the process which include the heating of the surface, equilibrium evaporation, phase explosion, ionization and plasma formation, and subsequent plasma shielding. Since the metal is often heated up to critical temperatures some have postulated that the temperature dependence of material properties has to be included as well [165]. The results presented in this chapter can possibly be of value to such efforts aimed at obtaining a more detailed understanding and accurate predictability of the laser ablation process of metals in the nanosecond regime. Our highly controlled experiment has the potential to serve as a model experiment, benefiting from the target's initial pure and homogeneous liquid state, its spatially contained spherical geometry, and the well-controlled flat temporal shape of the laser pulse.

6.6.3. Ablation of liquid-tin thin films

By making use of a pre-pulse to deform a droplet into a thin sheet [32], studying the ablation of liquid-metal thin films is within experimental reach as shown in Chapter 7. As shown, the inverse-square scaling of the ablation threshold with laser intensity as presented in Sec. 6.4 arises from the presence of one-dimensional thermal diffusion. In the thin-film limit such thermal diffusion is absent, entering a regime of thermal confinement accompanied by changes in ablation thresholds [164]. The current work could be extended by measuring the transition between bulk and thin-film ablation regimes, utilizing the sheet thinning over time resulting from pre-pulse impact [33]. Figure A.15 shows how during evaporation of a liquid tin sheet a plasma threshold is exceeded at the thick center part, but not on the thinner periphery of the sheet which is fully vaporized. Such plasma shielding is likely undesired in an advanced EUV-source vapor-target preparation scheme as it prevents vaporization of part of the liquid mass and possibly disturbs the formation of a uniform cloud target. By measuring the plasma onset thresholds for the case of thin sheets we can therefore identify a parameter range possibly beneficial to target preparation for droplet-based EUV sources.

Appendix

6.A. Brief analysis of reflection following plasma onset

Extra characterization of the reflection after the plasma onset threshold is passed is presented in Fig. 6.A.1. We simplify the observed behaviour into two cases, partial and full plasma shielding of the droplet. In the partially shielded case, averaging of the reflection signal obtained from many laser shots obscures the original chaotic behavior. Therefore, in Fig. 6.A.1(a) several single acquisitions are compared to the average of all 720 measurements. All traces coincide up until, and also slightly after, the drop in reflection attributed to the plasma generation. At later times, the plasma recoil pressure initializes deformation and a disorganized reflection signal consisting of many randomized peaks strongly differs from shot to shot.

In Figure 6.A.1(b) we show a quantification of the decrease of reflection when the droplet is fully shielded by the plasma cloud. A background signal is taken by misaligning the droplet to laser timing such that the droplet is missed. By subtraction of this background signal we find a remaining reflection of only 0.3% with a signal-to-noise ratio of 1.7.

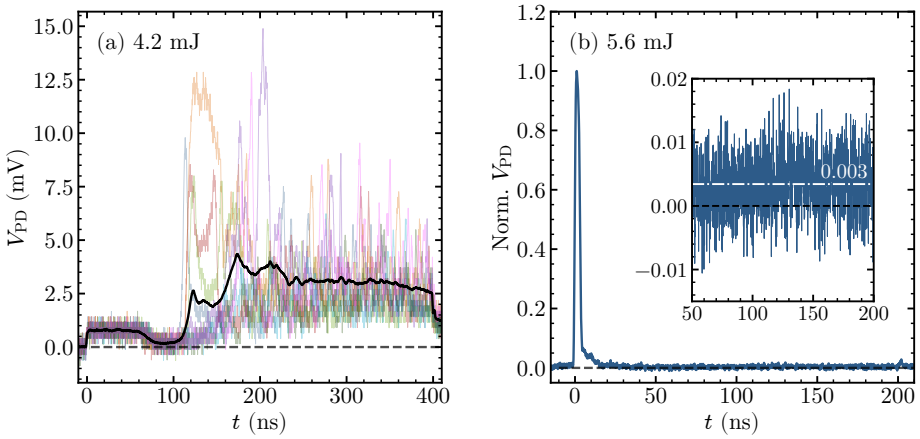

Figure 6.A.1: (a) Average (black) of 720 events overlaid on a selection (n=7) of single events illustrates the chaotic behavior of the reflection following plasma formation. (b) Reflection of a 5.6 mJ, 200 ns pulse for which the plasma fully shields the droplet.

Chapter 7

Laser-induced Vaporization of a Stretching Sheet of Liquid Tin

We experimentally study the mass distribution of a sheet of liquid tin formed by impact of a ns-laser pulse on a spherical microdroplet. The mass distribution is obtained using a low-intensity, second ns-laser pulse which induces vaporization of the stretching thin tin sheet. This careful vaporization enables the investigation of the thickness profile of the sheet, and its mass, at early times after laser pulse impact on droplet which have remained inaccessible by the methods used in recent work [B. Liu, et al., Phys. Rev. Applied **13**, 024035 (2020)]. The vaporization method moreover allows the visualization of the thick rim that bounds the thin sheet. Our results unambiguously demonstrate that increasing the energy of the ns-laser pulse incident on the droplet, which enables reaching a predetermined target radius more quickly, results in a larger mass fraction remaining in the sheet. Specifically, our studies show a doubling of the sheet mass fraction by reducing the required expansion time. As a corollary, less tin will end up in other channels of the mass distribution, such as fragments surrounding the sheet. Accordingly, more mass would be available in the target sheet for interaction with the more energetic, main laser pulse that is used in the industry to produce a hot and dense plasma from tin sheet targets in order to create extreme ultraviolet light for nanolithography.

Parts of this chapter have been published in Journal of Applied Physics **129**, 053302 (2021) [166].

7.1. Introduction

State-of-the-art nanolithography machines make use of extreme ultraviolet (EUV) light which enables the continued miniaturization of semiconductor devices [16, 21, 29, 38, 167, 168]. In order to generate the EUV radiation, liquid tin microdroplets are used as mass-limited targets in a dual-laser-pulse irradiation sequence. First, a nanosecond laser pulse, termed *pre-pulse* (PP), irradiates the tin microdroplet, causing it to deform into a liquid sheet within a few microseconds [30, 32, 33, 77, 93]. The sheet typically has a diameter of several hundreds of micrometers and thickness of several tens of nanometers [33, 77]. As the sheet expands, a bounding rim is formed at the edge of the sheet [33]. From this rim, a myriad of small fragments is propelled outwards along the radial direction [32, 33, 77, 93]. When the sheet has reached a specified diameter, a second, more energetic *main-pulse* is used to generate a dense and hot tin plasma that emits the relevant EUV radiation [62].

Recently our group reported on the hydrodynamic mechanisms that govern the thickness profile of nanosecond laser-induced sheets of liquid tin [33]. The experimental observations were used to benchmark a physical model that predicts the instantaneous sheet thickness and, from that, the mass of the sheet. Building on previous works [30, 100, 106, 169, 170], our research further confirmed a continuous loss of mass from the sheet over time. Remarkably, less than half of the initial amount of tin was found to remain in the sheet under currently relevant industrial conditions [33, 35, 112]. This finding is particularly pertinent in the context of EUV source lifetime which is adversely impacted by tin debris. Our results further indicated that using a relatively more energetic PP could be beneficial: increasing the PP energy leads to a faster initial expansion rate of the target sheet, and thus, any desired sheet size is reached earlier in the expansion trajectory, when more tin is carried by the sheet. To validate this proposition, knowledge of the sheet morphology at earlier times is needed. Since, inherently, the two methods previously used in Ref. [33] to determine the thickness profile are limited to mid- and late-time delays, we here employ an alternate method that is based on laser-induced vaporization. In this case, the sheets to be investigated will be irradiated by an auxiliary laser pulse, termed *vaporization pulse* (VP). This VP induces vaporization which gradually thins, or rarefies, the sheet into a mist comprising nanoparticles and, possibly, atomic tin. By measuring the time required to locally vaporize the sheet we can infer its thickness profile at early time delays unattainable by the previously used methods. The obtained sheet thickness profile finally yields the fraction of the initial volume (or, equivalently, mass) still contained in the sheet.

In this chapter, we investigate the tin mass distribution during laser-induced droplet deformation by introducing a method that allows us to obtain thickness profiles from careful laser-induced vaporization. Three targets sheets are selected, representing the mass distributions formed using various PP energies and at different stages of the expansion process. All these targets share an industrially relevant common sheet radius $R_{\text{sheet}} \approx 210\,\mu\text{m}$ [35, 112] (referred to as $R^\star$ hereafter) when we probe their thickness profile and mass content using the auxiliary VP. More specifically, we use two different PP laser energies to demonstrate a higher mass

content to be contained within the sheet when employing a higher PP energy. Additionally, we investigate two targets resulting from a constant PP energy yet at different moments during the expansion trajectory. We discuss the results, stressing the importance of the time delay after the PP impact on the droplet as the key parameter that ultimately determines the mass distribution of the target.

7.2. Experiment & Methods

In the experiments, a droplet generator dispenses a vertically aligned microdroplet train of liquid tin (temperature 260 °C, density $\rho = 6968\,\mathrm{kg/m^3}$ and surface tension $\sigma = 0.55\,\mathrm{N/m}$), with a droplet diameter of $D_0 = 2R_0 \approx 29\,\mu\mathrm{m}$ (where R_0 is the droplet radius that is established with an uncertainty of $\pm 0.5\,\mu\mathrm{m}$) into a vacuum environment (10^{-7} mbar). Two circularly polarized laser beams from independent Nd:YAG systems operating at 1064 nm wavelength are collinearly aligned onto the droplet. The timing sequence of the laser pulses from these two systems is illustrated in Fig. 7.1(a). The PP, with a Gaussian 10 ns (full width at half maximum, FWHM) temporal shape, is focused down to a Gaussian spot with a size of 55 µm (FWHM) at the location of the droplet. The VP, delayed by a time interval Δt, is produced by an in-house built system with arbitrary pulse shaping capabilities [42]. The system is programmed to output a temporally square 50 ns pulse, and its top-hat spatial profile is imaged onto the target with a beam diameter of $\approx 950\,\mu\mathrm{m}$. Therefore, the VP has a constant intensity distribution [denoted as I_{VP} ($\mathrm{W/m^2}$)], both spatially and temporally.

The dynamics of the irradiated targets are captured by stroboscopic shadowgraphy imaging systems [32, 33]. These systems combine incoherent pulsed backlight-illumination at 560 nm with CCD cameras coupled to long-distance microscopes, yielding a spatial resolution of approximately 5 µm. A dye laser provides the backlighting shadowgraphy pulses (SP) with a spectral bandwidth of 12 nm (FWHM) and a pulse duration of 5 ns (FWHM). As depicted in Fig. 7.1(a), the shadowgraphy systems simultaneously provide front- and side-view images of the tin targets, with 30° and 90° angles with respect to the Nd:YAG laser beam propagation direction, respectively.

Figure 7.1(a) illustrates the typical response of a droplet to the impact of a PP [30, 32, 33, 77, 93]. The droplet is rapidly propelled to a center-of-mass velocity U on the order of 100 m/s along the propagation direction of the laser [32, 93]. Furthermore, the droplet deforms into an axisymmetric sheet that radially expands to a size R_{sheet} over *time* (indicated as t hereafter, where $t = 0$ marks the arrival of the PP). These orthogonal motions, characterized by U and the initial expansion rate immediately after laser pulse impact $\dot{R}(t = 0)$ (referred to as $\dot{R}_0$ hereafter), are driven by plasma pressure [32, 77, 93]. Typically, $\dot{R}_0 \sim U$ as in the analogous case of droplet-pillar impact studied in Ref. [106]. The time scale of the acceleration is similar to the laser pulse length ($\tau_{\mathrm{p}} \sim$ ns), vastly shorter than the time scale of the ensuing fluid-dynamic deformation ($\tau_{\mathrm{c}} \sim$ µs) [30, 38]. The sheet is irradiated by the VP when it acquires a radius of $R^{\star}$. This onset moment of the VP is referred to as $t_{\mathrm{VP}} = 0$.

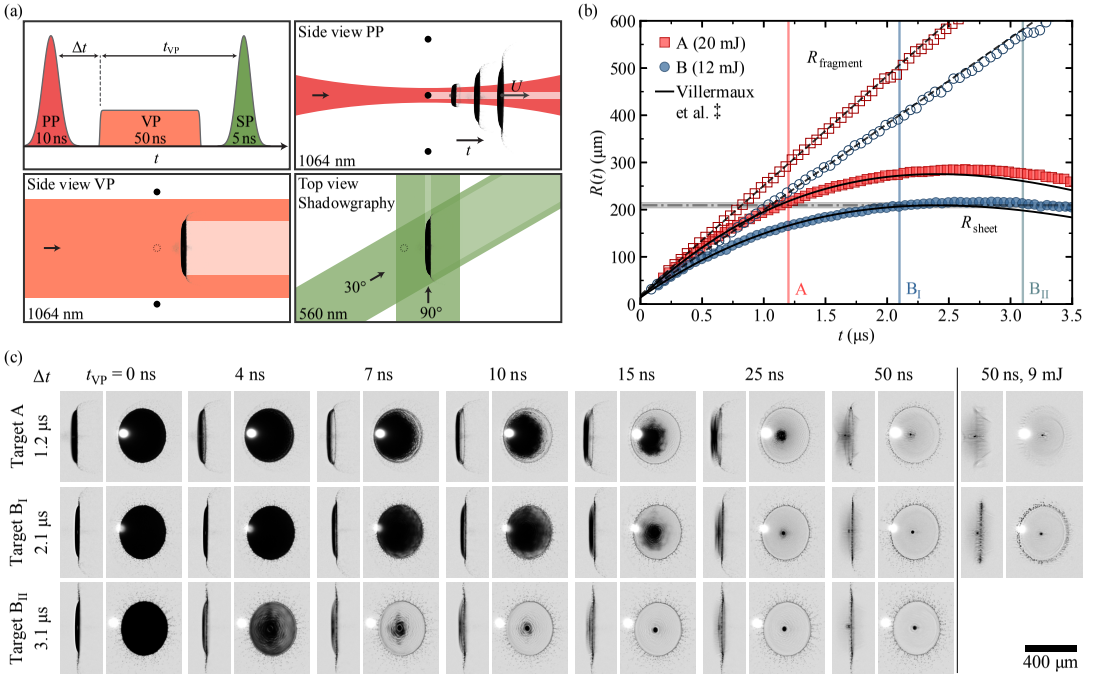

Figure 7.1: (a) Illustration of the laser pulse sequence and the respective irradiation geometries. Upper-left: timing of the irradiation scheme, starting with the pre-pulse (PP), followed by the vaporization pulse (VP) after a time interval Δt. To visualize the dynamics of the tin target, the shadowgraphy illumination pulse (SP) is scanned through time t, where $t = 0$ marks the onset of the PP. The start of the VP is indicated by time delay $t_{\mathrm{VP}} = 0$. Upper-right & lower-left: side-view schematics of the irradiation conditions during PP and VP, respectively. Lower-right: top-view of 30° and 90° shadowgraphy backlighting. (b) Sheet expansion radius R_{sheet} and farthest fragments distance-to-center R_{fragment} as a function of time t for two PP energies (20 mJ and 12 mJ). The horizontal dash-dotted line (along with a shaded area to indicate the uncertainty) is at a constant 210 µm radius (i.e., $R^{\star}$). This line intersects the R_{sheet} curves at $t = 1.2$, 2.1 and 3.1 µs (as indicated by the vertical lines), at which moments the sheets are referred to as target A, $\mathrm{B_I}$ and $\mathrm{B_{II}}$, respectively. The solid lines (‡) following R_{sheet} are fits of the model from Ref. [106] to the data up to 2 µs. The dashed lines along R_{fragment} result from a linear fit to the data up to 1.5 µs. (c) Series of side-view (left) and front-view (right) shadowgraphy images of the three targets during illumination by the VP for different time delays. The VP energy $E_{\mathrm{VP}} = 5$ mJ excluding the last column, where $E_{\mathrm{VP}} = 9$ mJ. At $t_{\mathrm{VP}} = 0$ all three targets share a common sheet size $R^{\star}$ (i.e. $R_{\mathrm{sheet}} \approx 210$ µm).

7.3. Target selection & vaporization

To determine the moments at which the sheet reaches $R^\star$ for the chosen PP energies of $E_{\text{PP}} = 12\,\text{mJ}$ and 20 mJ, we first investigate the sheet size evolution $R_{\text{sheet}}(t)$ presented in Fig. 7.1(b). After PP impact, the sheet expands with an initial rate $\dot{R}_0$. With a higher PP energy, $\dot{R}_0$ is larger, and hence less time is required to reach $R^\star$. For the case of $E_{\text{PP}} = 20\,\text{mJ}$, the sheet attains this specific size at $t = 1.2\,\mu\text{s}$. We refer to this target as target A. For the lower energy case of $E_{\text{PP}} = 12\,\text{mJ}$, $R^\star$ is first reached at $t = 2.1\,\mu\text{s}$. We refer to this target as target B_I. After passing the apex of its expansion trajectory, the sheet retracts due to the surface tension exerted at the sheet edge [30, 33, 77], and again acquires $R^\star$ at $t = 3.1\,\mu\text{s}$, which we refer to as target B_II. We find that $R_{\text{sheet}}(t)$ agrees well with the analytical model developed by Villermaux et al. [106] for the analogous case of droplet impact onto a pillar. Such an agreement has been previously reported in Ref. [77]. By fitting this model to the data, we obtain the initial expansion rate $\dot{R}_0$ (for $E_{\text{PP}} = 20$ and 12 mJ, $\dot{R}_0 = 244$ and 182 m/s, respectively) with it being the only free fit parameter. Figure 7.1(b) also presents the radial position of the furthest fragments as a function of time $R_{\text{fragment}}(t)$. We find that these fragments follow an expected ballistic trajectory [171], the slope of which matches the initial expansion rate of the sheet $\dot{R}_0$. We note the significant difference in the distance between the outermost fragments and the sheet edge for the three targets. Each of these three targets, with the common sheet size of $R^\star$, is irradiated by the VP to infer the thickness profile $h(r)$ and mass content of the sheet.

Figure 7.1(c) presents the front- and side-view shadowgraphy images of the targets through the duration of the VP with an energy of $E_{\text{VP}} = 5\,\text{mJ}$. At the beginning of the VP (i.e., $t_{\text{VP}} = 0$), the images show that the main features of these targets include a sheet of liquid tin that is surrounded by small fragments. During VP illumination, we observe a gradual mass removal from the sheet as it becomes transparent to the background illumination light. The vaporized material does not significantly impede the shorter-wavelength shadowgraphy light and, thus, is not expected to influence the vaporization pulse. Over time, this transparency is seen to move from the periphery inward towards the center of the sheet, leaving a retreating inner sheet with a radius R_{inner}. Given the fact that the VP has a uniform intensity across the beam profile, we reasonably assume that more time is needed to vaporize a sheet that contains more tin and, as a result of the common sheet-size $R^\star$, is also thicker. Among the three targets, target A requires the longest time for its sheet to be completely vaporized, followed by targets B_I and B_II. We infer that the respective global sheet thicknesses and volumes follow the same order. As a side note, we find that the periphery of target A starts to show transmission prior to that of target B_I ($t_{\text{VP}} = 7\,\text{ns}$). When the periphery of the sheet is removed, a bounding rim appears (see, e.g., front-view images at $t_{\text{VP}} = 25\,\text{ns}$). Such a bounding rim has been widely reported in various scenarios of droplet impact on a solid [106, 169, 170, 172–174]. For the case of laser-droplet impact, the thickness and mass of this rim has been analytically estimated in our previous work [33] and now is visualized. Note that for target B_II, the sheet as a whole appears to become transparent almost

simultaneously (see Fig.7.1(c) at $t_{\mathrm{VP}} = 4\,\mathrm{ns}$) instead of gradually retreating inward. This is due to the vaporization taking place on a timescale similar to the duration ($\approx 5\,\mathrm{ns}$) of the shadowgraphy illumination pulse.

By the end of the VP ($t_{\mathrm{VP}} = 50\,\mathrm{ns}$) the sheet is completely removed for all targets. In contrast, the rim and many of the fragments are still present, indicating that the sheet is much thinner than the rim and fragments, confirming our observation in Ref. [33]. Although the rim and most of the fragments are not fully resolved by our imaging system, from the observed contrast [175] we do infer that target A has a thinner rim and finer fragments compared to the other targets. In fact, target A has such small-sized fragments that a VP of 5 mJ is capable of vaporizing a significant fraction of them by the end of the VP. With a higher VP energy of 9 mJ all the fragments and the rim of target A are completely vaporized [see the rightmost column in Fig. 7.1(c)]. In contrast, for targets $\mathrm{B_I}$ and $\mathrm{B_{II}}$ no clear vaporization of fragments is observed for a 5 mJ VP, and even with the 9 mJ VP some fragments and leftovers of the rim remain for target $\mathrm{B_I}$. Besides the rim and fragments, a remnant of tin resides at the center of the sheet ($t_{\mathrm{VP}} = 50\,\mathrm{ns}$). Its presence after VP irradiation indicates that also its thickness is significantly larger than that of the sheet. The existence of this center mass is also consistent with our previous observations in Ref. [33].

In Fig. 7.2(a), we present the radius of the inner sheet $R_{\mathrm{inner}}(t_{\mathrm{VP}})$ as it evolves throughout the VP duration. The radii have been retrieved from shadowgraphy images such as those shown in Fig. 7.1(c). Again, in Fig. 7.2(a) we identify that R_{inner} reduces over time for all targets, amongst which that of target A and $\mathrm{B_{II}}$ decreases at the slowest and the fastest rate, respectively. In the experiment, we found that at a given location r on the sheet, the local time $\tilde{t}_{\mathrm{VP}}(r)$ required for the VP to vaporize the local thickness $h(r)$ is inversely proportional to I_{VP}. This has been systematically observed in a scan for various VP pulse energies (ranging from 2 to 9 mJ). The linear proportionality $\tilde{t}_{\mathrm{VP}}(r) \propto I_{\mathrm{VP}}^{-1}$ indicates that the thickness $h(r)$ is proportional to the VP energy locally deposited in the sheet, i.e. $h(r) \propto I_{\mathrm{VP}} \tilde{t}_{\mathrm{VP}}(r)$. With a constant VP intensity I_{VP}, we can thus conclude $h(r) = \tilde{t}_{\mathrm{VP}}(r)\dot{h} \sim \tilde{t}_{\mathrm{VP}}(r)$, where $\dot{h}$ refers to a time-average vaporization rate. We make the ansatz that $\dot{h}$ is independent of the local thickness. Thus, the thickness profile of the sheet can be directly obtained from Fig. 7.2(a) by exchanging its x- and y-axes and using a single overall scaling factor $\dot{h}$.

7.4. Thickness & mass content of the targets

In Ref. [33] a partial transparency of the sheet to the shadowgraphy backlighting was used to determine the sheet thickness profile. A significant transmission signal can only be obtained if the sheet is sufficiently thin. We find that this transmission method can be applied to the thinnest target, $\mathrm{B_{II}}$, and we determine its sheet thickness before VP impact ($t_{\mathrm{VP}} = 0$). Subsequently, we are able to determine the scaling factor $\dot{h}$ from a fit such that $h(r) = \tilde{t}_{\mathrm{VP}}(r)\dot{h}$ for target $\mathrm{B_{II}}$ matches its thickness as acquired from the transmission method in absolute terms, as presented in the inset of Fig. 7.2(b). The fit shows excellent agreement between the two methods

regarding the shape of the sheet thickness. This fit yields $\dot{h} = 4.4(4)$ m/s, with the systematic uncertainty in brackets originating from uncertainties in the background correction related to, e.g., dark noise or plasma glare [33, 175]. The obtained $\dot{h}$ lies in the range of values obtained in other studies of the ablation of metals under similar irradiation conditions (here the VP fluence is $\approx 0.7\,\mathrm{J/cm^2}$) [176, 177]. With the known value of $\dot{h}$, we are able to plot the thickness profiles for target A and $\mathrm{B_I}$.

Figure 7.2(b) presents the sheet thickness $h(r) = \tilde{t}_{\mathrm{VP}}(r)\dot{h}$ as a function of the radial position r for all targets. Moreover, we plot the semi-empirical thickness model [33]

$$h(r,t) = \frac{D_0^3}{1.65\,(\dot{R}_0\,t)^2 + 6.9\,t\,r\dot{R}_0 - 2.4\,r^2}. \tag{7.1}$$

It is shown in Fig. 7.2(b) and its inset that Eq. (7.1) agrees well with the current thickness profiles, both obtained from $h(r) = \tilde{t}_{\mathrm{VP}}(r)\dot{h}$ and, for target $\mathrm{B_{II}}$, also from the independent measurement from the transmission method. Here, we employ the initial expansion rate $\dot{R}_0$ as the characteristic velocity in Eq. (7.1) instead of the center-of-mass speed U as originally used in Ref. [33]. This substitution is motivated by a relatively strong deviation from the $\dot{R}_0 \sim U$ similarity [106, 169] for targets $\mathrm{B_I}$, $\mathrm{B_{II}}$, arising from the tight focusing condition of the PP used here. As elucidated in Ref. [30], the spatial distribution of the pressure field exerted by the expanding plasma on the droplet surface influences the ratio $\dot{R}_0/U$. A loosely focused beam (i.e. 105 µm at FWHM in Ref. [33]) and also an increasing PP energy [77] effectively results in a spreading pressure distribution that yields $\dot{R}_0/U \approx 1$. In contrast, an increasingly focused pressure field, which, for example, can be achieved by employing a tightly focused beam (i.e. 55 µm at FWHM for the present study), results in a larger fraction of the kinetic energy partitioned to expand the droplet rather than to propel it, and thus $\dot{R}_0/U > 1$. Our analysis indeed shows $\dot{R}_0/U = 1.26$ for targets $\mathrm{B_I}$ and $\mathrm{B_{II}}$, and $\dot{R}_0/U = 1.09$ for target A, justifying choosing $\dot{R}_0$ as the relevant velocity describing the deformation dynamics.

The thickness data $h(r)$ shown in Fig. 7.2(b) enables the determination of the sheet volume by integrating $2\pi r h(r)\delta r$ along the radial coordinate, starting from R_0 to the edge of the sheet [33, 106]. The region $r < R_0$ is thus excluded from the integration (cf. Refs. [33, 106]) and with it the center mass remnant (see Fig 7.1(c)) that has a different physical origin [33]. Figure 7.2(c) presents the obtained volume ratio of the sheet to the initial droplet V_{sheet}/V_0 as a function of the non-dimensional time t/τ_c, with capillary time $\tau_c = \sqrt{\rho R_0^3/\sigma} = 6.6\,\mu\mathrm{s}$. The data indicate a monotonic decrease of the fraction of tin contained in the sheet over time. At the moment of $t/\tau_c = 0.19$ (i.e., target A), the sheet carries close to 60% of the initial amount of tin. For comparison, the data of V_{sheet}/V_0 from Ref. [33] are also shown in panel (c). Despite the differences in the experimental conditions (regarding R_0, E_{PP}, and the focal spot size of the beam) between the present study and Ref. [33], these two data sets agree well with each other. Additionally, in panel (c) we plot the model

$$\frac{V_{\mathrm{sheet}}}{V_0} = \left(1 - \frac{\sqrt{3}}{2}\frac{t}{\tau_c}\right)^2, \tag{7.2}$$

which was derived in Ref. [33] using the analytical expression of the thickness profile and the radius of the sheet from Ref. [106]. Equation (7.2) was found in Ref. [33] to be able to describe the sheet volume for the laser-droplet impact case. Figure 7.2(c) shows that in the present study, Eq. (7.2) is consistent with the experimental findings also in the early time regime. Further experimental data would benefit the detailed study of the full evolution of the sheet thickness and its volume, and is needed to attest to the general validity of Eq. (7.2), in particular at the early times that have now become accessible employing the laser-induced vaporization method. In short, our results show a good agreement with the prediction from Eq. (7.2), and match well with our previous study in Ref. [33] in the late-time overlap region. We thus unambiguously demonstrate that increasing the energy of the laser pre-pulse which, crucially, enables the sheet to reach a specified target size more quickly, results in a significantly larger mass fraction contained in the sheet.

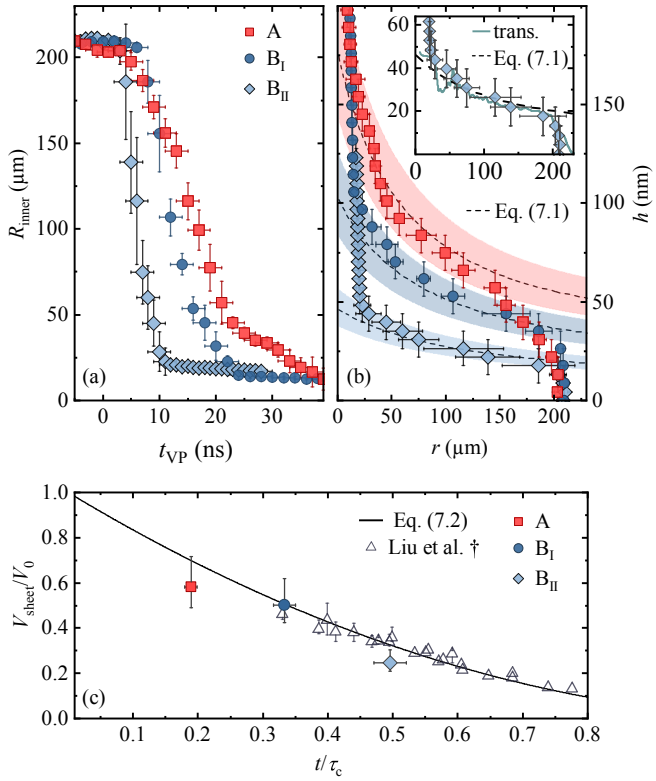

Figure 7.2: (a) Radius of the inner sheet R_{inner} as a function of t_{VP} during VP-induced vaporization. (b) Sheet thickness h, obtained by $h(r) = \tilde{t}_{\text{VP}}(r)\dot{h}$, as a function of radial position r. The time-averaged vaporization rate $\dot{h}$ is obtained by fitting the thickness of target B_{II} obtained from the transmission method to the corresponding data of $t_{\text{VP}}(R_{\text{inner}})$, see the main text. The result of this fit is presented in the inset. The thickness model given by Eq. (7.1) is presented by the dashed line, with the shaded region indicating the uncertainty propagated from $R_0 \pm 0.5\,\mu\text{m}$ and $\dot{R}_0 \pm 5\%$.(c) Volume ratio of the sheet to the initial droplet V_{sheet}/V_0 as a function of the scaled time t/τ_c, where $\tau_c = 6.6\,\mu\text{s}$, with values $0.58^{+0.13}_{-0.09}$, $0.50^{+0.12}_{-0.08}$, and $0.25^{+0.06}_{-0.04}$ for targets A, B_{I}, and B_{II}, respectively. Previously reported data (open triangles) from Ref. [33] (†) are presented alongside the new results. The solid line depicts Eq. (7.2).

7.5. Conclusion

In this chapter, we experimentally investigated the mass content of expanding sheets of liquid tin, formed upon nanosecond pre-pulse laser impact on tin microdroplets. An auxiliary vaporization laser pulse was used to gradually remove mass from the liquid sheet, thereby exposing the sheet's thickness profile and mass content. Furthermore, the removal of the sheet revealed and confirmed the presence of a sheet bounding rim and center mass. Three targets, generated by using two different PP energies, were selected at different times during their expansion trajectories such that they all shared a common sheet size $R^\star = 210\,\mu\text{m}$. The thickness of the thinnest target has been independently determined by an optical method that has been validated in Ref. [33]. The resulting thickness enabled a conversion of the local time of vaporization of the other two targets by the auxiliary pulse to the thickness profiles of the sheets. We have further shown that the thickness for each target agrees well with the model developed in Ref. [33]. The spatial integration of the obtained thickness profile yielded the volume fraction of the sheet for each target, for which we found a good agreement with previously reported models. The results confirmed how using a more energetic PP is a favorable strategy for achieving a specified sheet size while minimizing mass loss from the sheet to the bounding rim and fragments. For the target with the highest PP energy studied here, we found that approximately 60% of the mass was still present in the sheet, more than doubling the mass fraction that may be expected to be contained in targets reported in available literature relevant for the nanolithography industry [35, 112]. Investigations of the thickness profile and target mass at even earlier times after laser pulse impact are accessible by the laser-vaporization method. Our findings and method can serve a crucial role in the optimization of PP parameters, maximizing the tin mass available for the production of EUV light in tin-droplet-based plasma sources for nanolithography.

Appendix A

Shadowgram Gallery

The amount of observable deformation types and features resulting from laser impact on the tin microdroplets seem endless. Often, experimenting with the laser pulse parameters, i.e., energy, duration, temporal shape, focal spot size, etc., or using multiple pulses, led to new and exciting observations. This gallery, which shows a selection of shadowgrams that did not make it into any of the main chapters, aims at illustrating the breadth of possible outcomes following the interaction between laser pulses[1] and droplets and the complex physical processes involved in it.

[1] The laser pulse is incident from the left and has a wavelength of 1064 nm

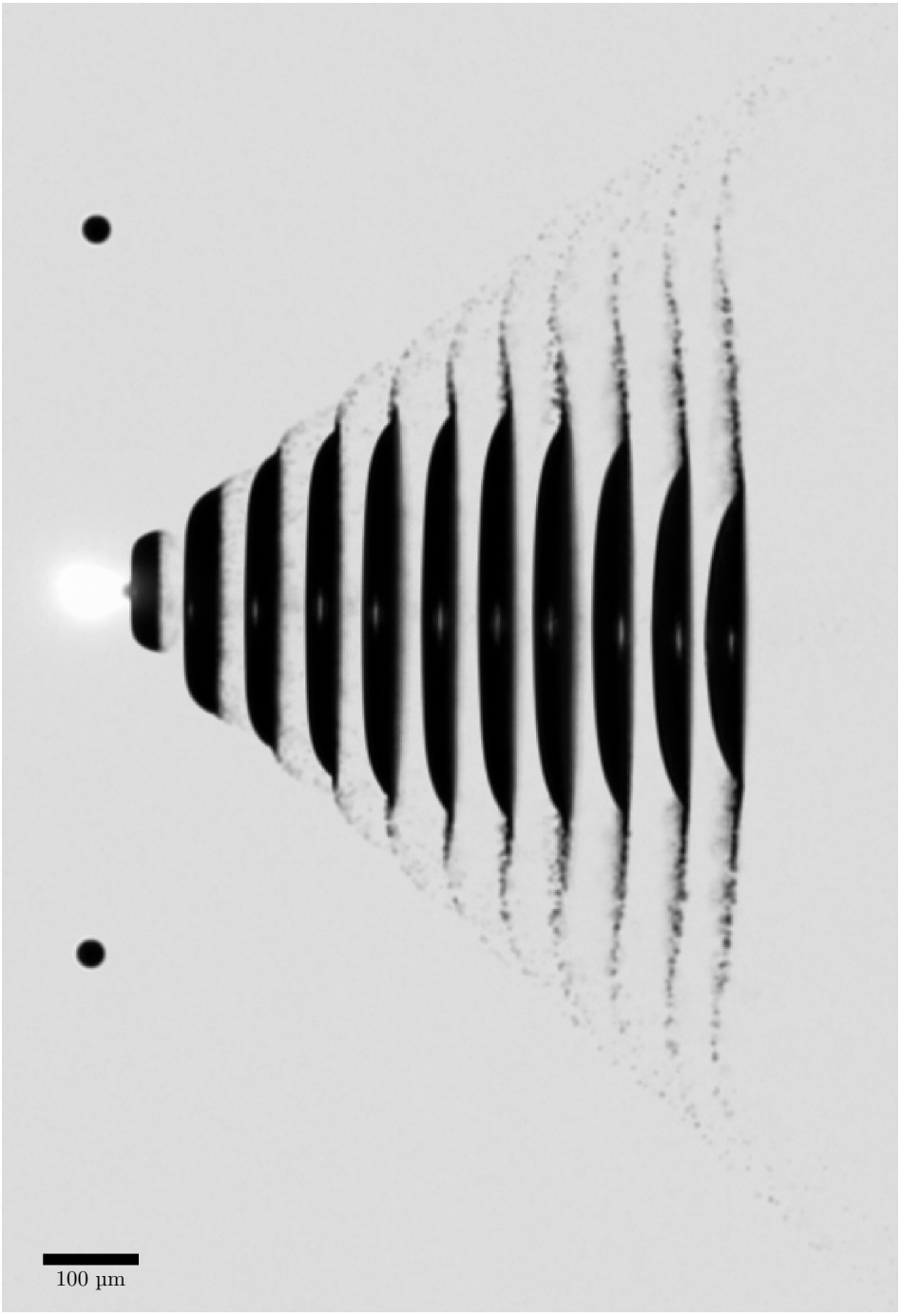

Figure A.1: Overlaid side-view shadowgrams of deformation corresponding to target B from Chap. 7. The first, most left shape corresponds to $t = 260\,\mathrm{ns}$, with each successive shape spaced by 200 ns. The last, most right shape is recorded at $t = 4.26\,\mu\mathrm{s}$. In one image, we here capture the target morphology, propulsion U, the expansion and retraction behavior of the central sheet $R(t)$, and the linear trajectory of the outer most fragments which travel at a velocity similar to $\dot{R}_0$.

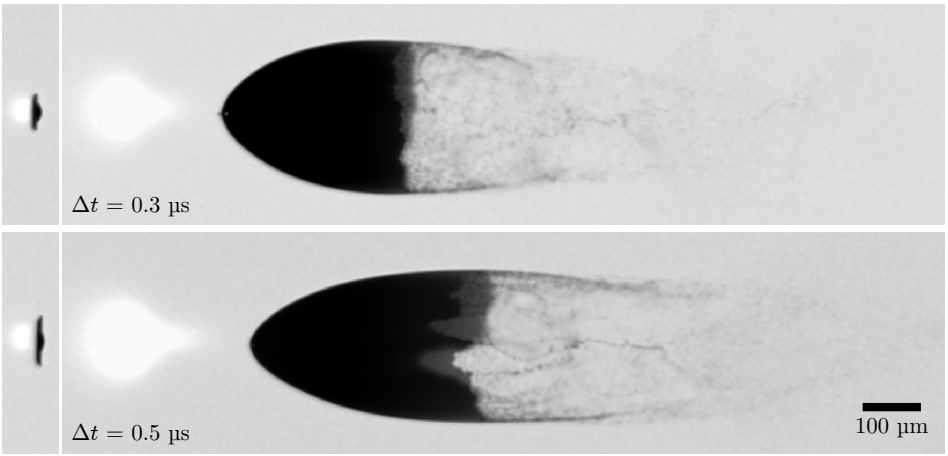

Figure A.2: Zeppelin-like shapes following impact of a 10 ns and 5 ns Gaussian pulse pair spaced by a time Δt. The first pulse (0.6 mJ, 60 µm FWHM) initiates the deformation of the droplet ($d \approx 30$ µm) which starts expanding at a relatively low rate ($\dot{R}_0 \sim U \approx 25\,\mathrm{m\,s^{-1}}$). The second pulse (16 mJ, 80 µm FWHM) impacts the deforming target within the inertial timescale $\tau_\mathrm{i} \sim d/U \approx 1.2$ µs. The target impacted by the second pulse is shown in the left column. The two cases shown are for (top) $\Delta t = 0.3$ µs and (bottom) $\Delta t = 0.5$ µs. The targets after second-pulse impact shown in the right column are recorded 0.9 µs after impact of the second pulse

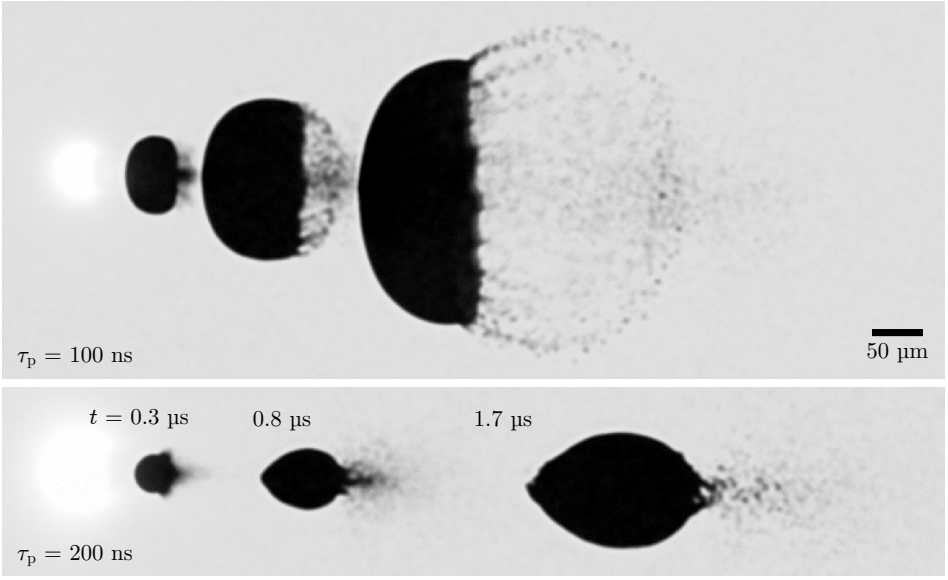

Figure A.3: Deformation following impact of (top) a 100 ns square pulse and (bottom) a 200 ns square pulse. Three different shadowgraphy time delays of 0.3, 0.8, and 1.7 µs are overlaid. The relatively long duration of the incident laser pulse and the duration of the accompanying prolonged plasma push are similar to or larger than the inertial timescale, i.e. $\tau_\mathrm{p} \gtrsim \tau_\mathrm{i}$. As a result the expanding sheet is strongly curved and the expansion rate reduced compared to shorter pulses when $\tau_\mathrm{p} \ll \tau_\mathrm{i}$ (see Fig. A.1).

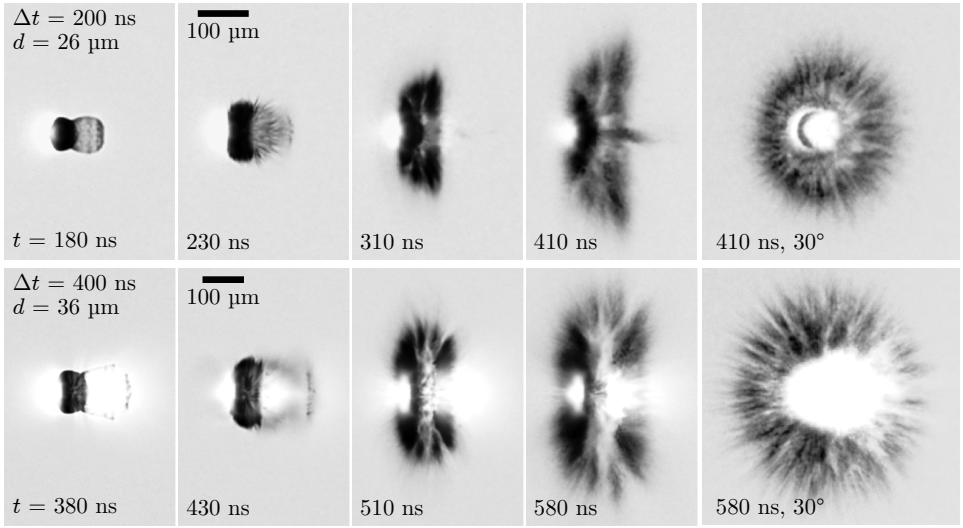

Figure A.4: Explosive fragmentation following impact of a 0.4 ns pulse pair spaced by (top) 200 ns and (bottom) 400 ns. First four columns show side-view shadowgrams with increasing shadowgraphy delay time from left to right. The last column shows a 30° front view at the same delay time as the last side view. These measurements were taken during the experiment presented on in Chapter 5 (see Fig. 5.2), where additional information can be found. The streaks indicate that the particles travel several to tens of micrometers during the 5 ns shadowgraphy backlighting pulse and therefore are moving at speeds on the order of $\mathrm{km\,s^{-1}}$.

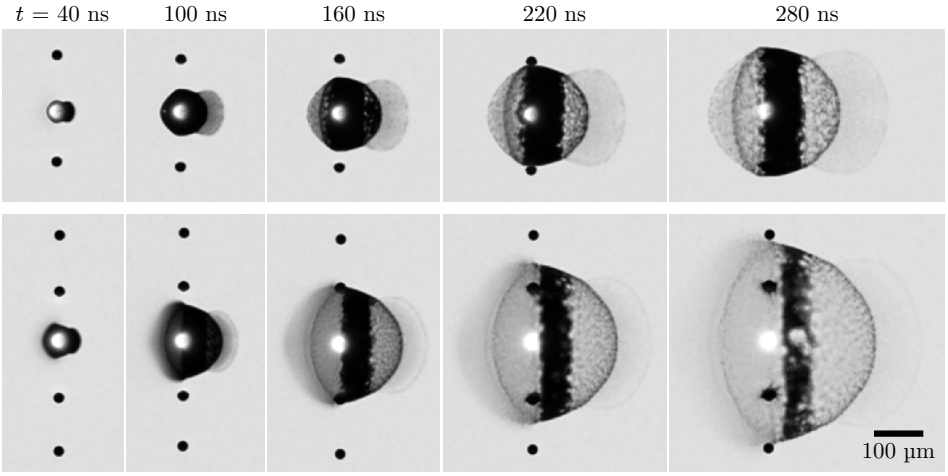

Figure A.5: Side view recording of deformation following 0.4 ns pulse impact for relatively high E_{od}/R_0^3 values (see Chap. 3). This data was recorded during experiment A listed in table 3.1 with a droplet size of $d = 20\,\mu\mathrm{m}$ and pulse energies of (top) 30 mJ and (bottom) 60 mJ.

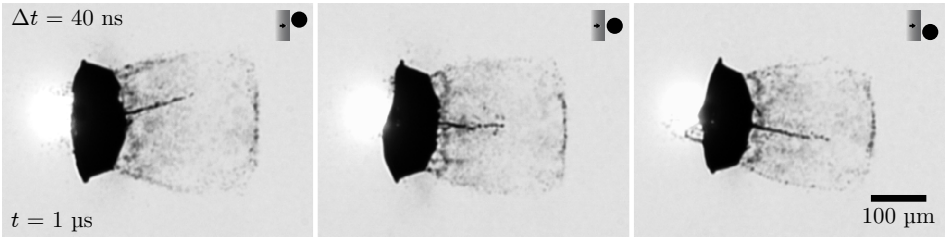

Figure A.6: Jet direction for three different cases of laser-to-droplet alignment using a pulse pair with two 0.4 ns pulses and a flat-top beam profile. The jetting, as discussed in more detail in Sec. 5.6, is the result of the impact of two 'short' pulses spaced on a nanosecond timescale (here, $\Delta t = 40$ ns). Since in this case the spatial beam profile has a flat intensity its relative alignment with respect to the droplet is not relevant for the first pulse, as long as the droplet hemisphere is fully illuminated. The second pulse impacts an already slightly deformed target surrounded by an expanding plasma cloud, and therefore a target which is effectively larger. As a result, a laser-to-droplet misalignment has a significant effect on the generation of the jet-inducing shock wave launched by impact of the second pulse. These two effects combined lead to the following observation: When we move the beam across the droplet, the spall caused by impact of the first pulse is stationary, but the direction of the jet changes [125]. Laser-to-droplet alignment is illustrated in the upper right corner of each frame. This data was recorded during experiment A listed in table 3.1.

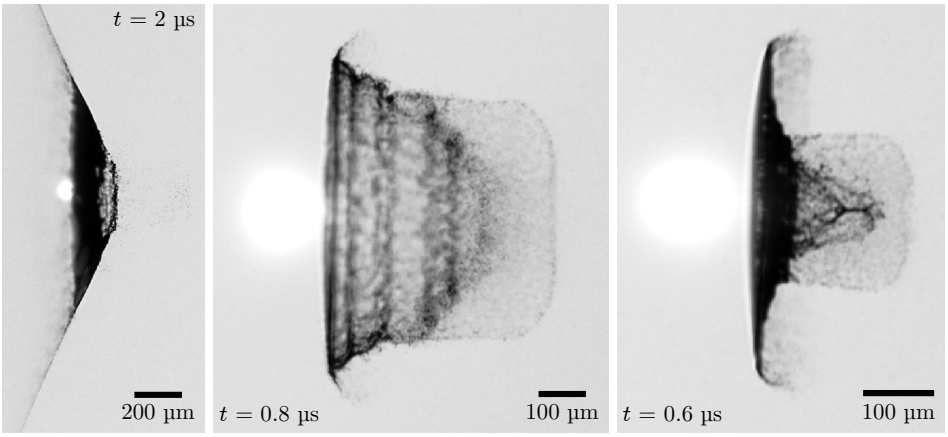

Figure A.7: (left) A tightly focused beam with a full width at half maximum spot size of approximately 6 µm gives rise to this concave cone shape (side view), which is most similar to shapes observed in Ref. [99]. The exact laser energy and pulse duration are unknown, but are in the order of 100 mJ and a few ns. Note that spall fragments are visible. (center) Side view of a shape resulting of impact of a pulse sequence (ﻝﺱ) consisting of three 0.4 ns pulses with consecutive spacings of 7.8 ns and 1.3 ns and a total energy of 60 mJ. (right) A scooped square shape (ﻡ) with a peak-to-peak duration of 7 ns and energy of 50 mJ. The data shown center and right was recorded during experiment C listed in table 3.1 with both a droplet diameter and focal spot FWHM of 45 µm.

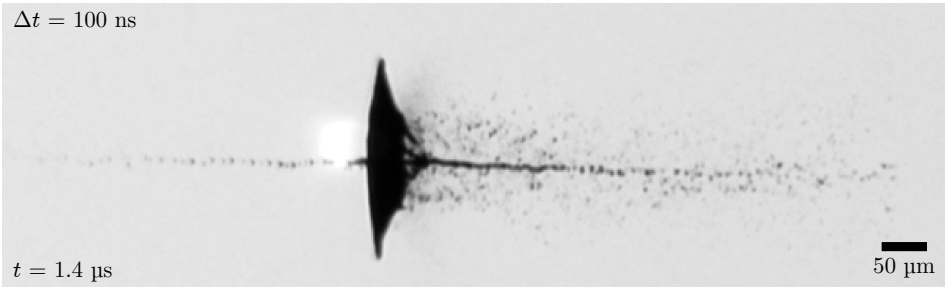

Figure A.8: Side view of strong bi-directional jetting originating from the droplet following impact of a pulse pair consisting of 0.4 ns pulses spaced by $\Delta t = 100$ ns with a total energy of 2.5 mJ. This data was recorded during experiment C listed in table 3.1 with a droplet diameter of $d = 19$ µm. The jetting, discussed in more detail in Sec. 5.6, in this case strongly resembles the mechanism observed in laser-induced forward transfer [178, 179].

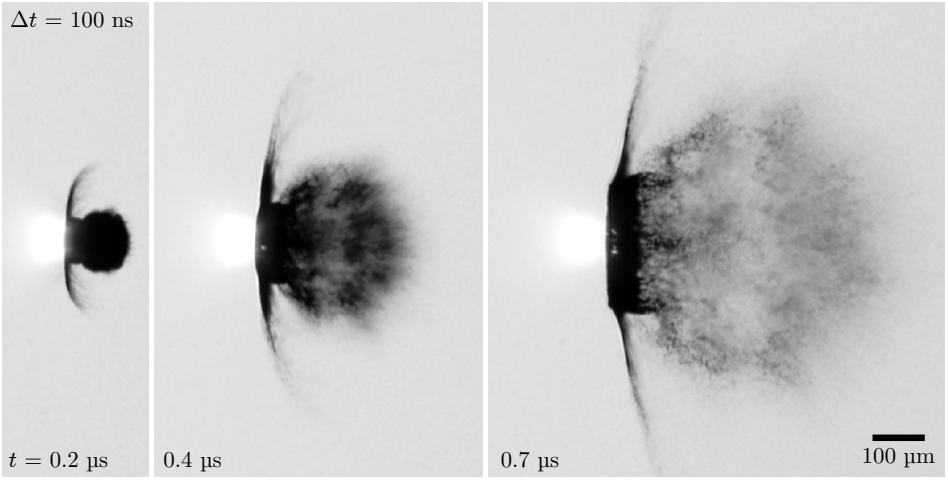

Figure A.9: Side view of strong spall fragmentation from the droplet following impact of a pulse pair consisting of 0.4 ns pulses spaced by $\Delta t = 100$ ns with a total energy of 12.5 mJ (higher energy case of Fig. A.8). This data was recorded during experiment C listed in table 3.1 with a droplet diameter of $d = 19$ µm.

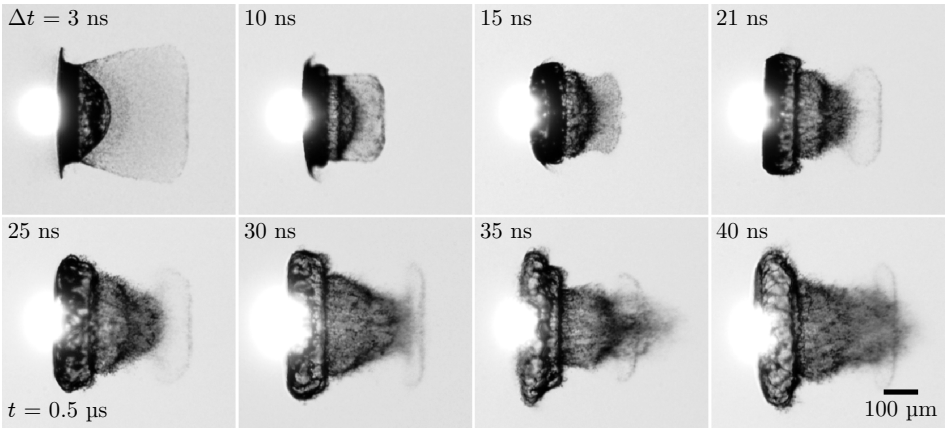

Figure A.10: Side-view deformation following impact of a 0.4 ns pulse pair with varying spacing Δt. This data is similar to that presented in Chap. 5, also with a 40 mJ combined pulse energy, but with a significantly higher fluence. A spall-debris-velocity reduction (or possibly a squeezing of the debris cloud) seems to also be present here, but the data was taken with too large Δt steps to see a clear trend. These images were recorded during experiment C listed in table 3.1 with both a droplet diameter and focal spot FWHM of 45 µm. In the image at $\Delta t = 15$ ns the target is slightly tilted in the viewing plane.

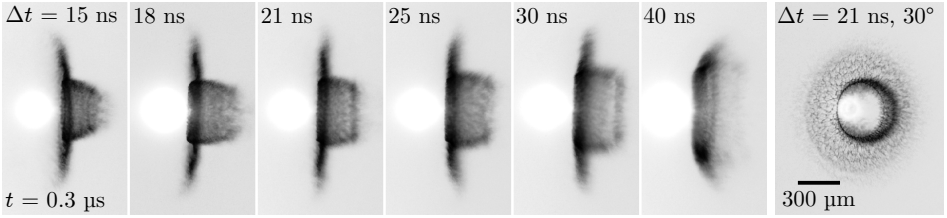

Figure A.11: Side-view deformation following impact of a 0.4 ns pulse pair with varying spacing Δt. This data is similar to that presented in Fig. A.10, but with 170 mJ combined pulse energy. The liquid is completely fragmented and traces out a hollow hat-like shape. With increasing Δt the angles of both the vertical en horizontally aligned features of the shape follow a particular trend. These images were recorded during experiment C listed in table 3.1 with both a droplet diameter and focal spot FWHM of 45 µm.

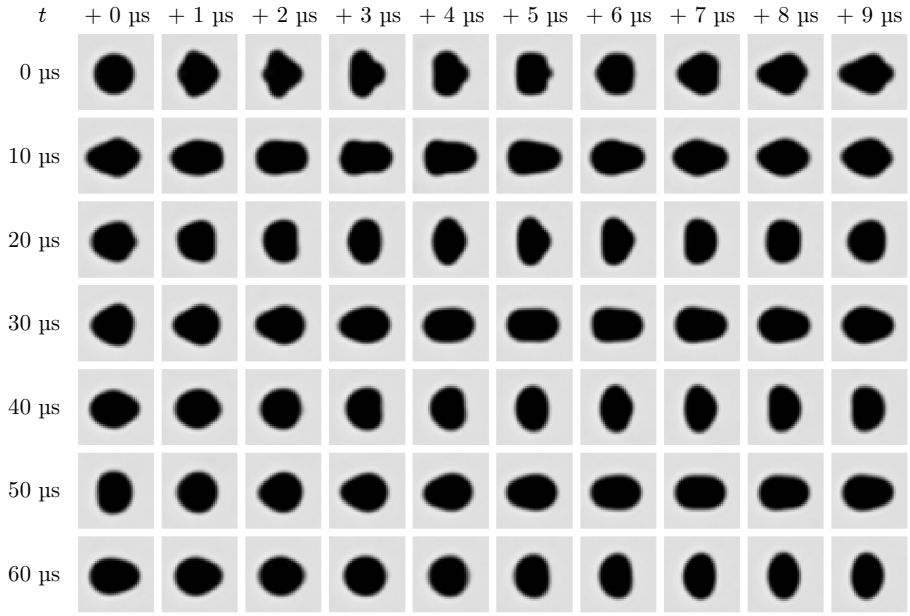

Figure A.12: Side-view recording of the oscillation of an approximately 40 µm diameter droplet following impact of a low-energy 0.4 ns Gaussian pulse with a fluence of approximately $3\,\mathrm{J\,cm^{-2}}$ ($E_{\mathrm{od}}/R_0^3 \approx 5 \times 10^{-6}\,\mathrm{mJ\,\mu m^{-3}}$). Each image is the average of 10 frames centered at the center of mass. The shadowgraphy delay time increases by 10 µs for each row and 1 µs for each column.

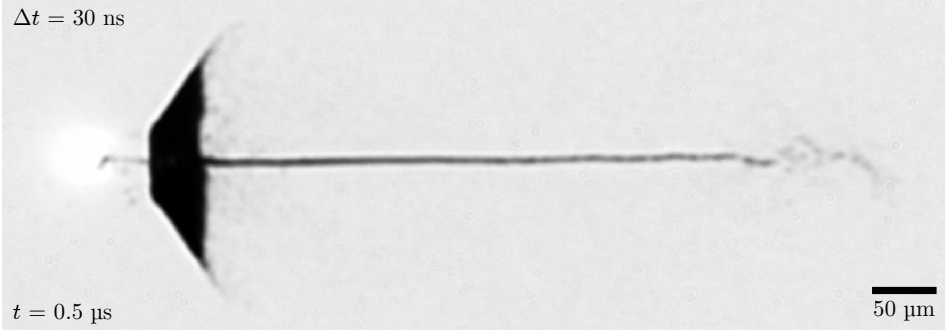

Figure A.13: Side view of a long, several micrometer thick, microjet originating from the droplet following impact of a pulse pair consisting of a 0.4 ns pulse followed by an approximately 10 ns pulse after a delay of $\Delta t = 30$ ns. This data was recorded during experiment B listed in table 3.1 with a droplet diameter of $d = 19$ µm. The jetting phenomena is discussed in more detail in Sec. 5.6.

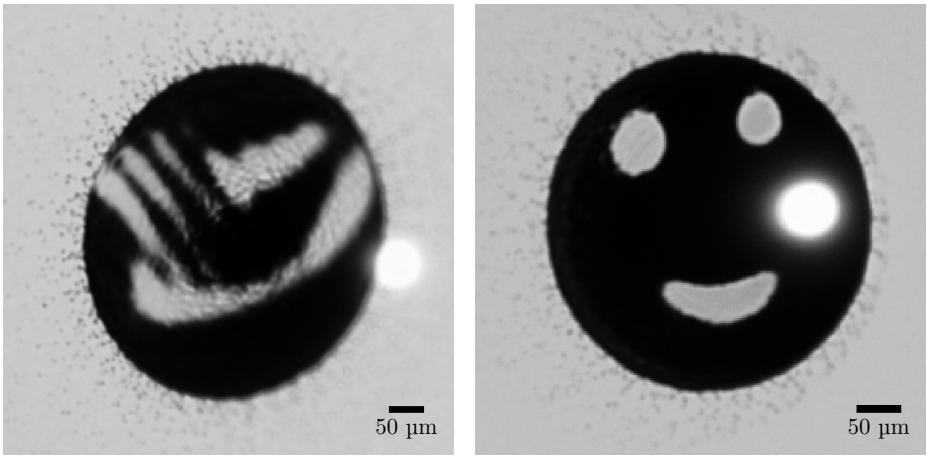

Figure A.14: Front views of (left) the ARCNL logo and (right) a smiley face vaporized from the liquid tin sheet by a 50 ns vaporization pulse as elaborated in Chap. 7. Laser-milled brass binary masks of both shapes, courtesy of Nik Noest and Henk-Jan Boluijt, were positioned in the image plane of the flat-top beam and imaged onto the expanding sheets with a demagnification of approximately 5.

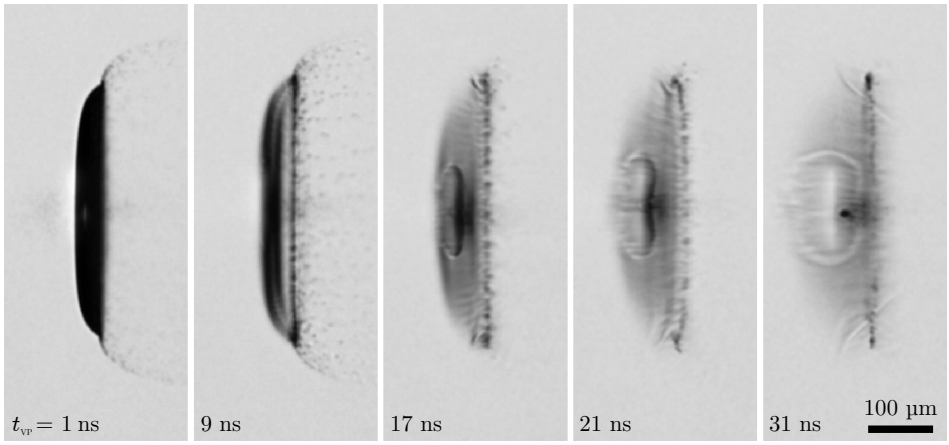

Figure A.15: Vaporization of a sheet target (corresponding to target A from Chap. 7) with a relatively high-intensity, temporally Gaussian-shaped vaporization pulse ($\tau_p = 10\,\text{ns}$, $E = 9\,\text{mJ}$). Vaporization of the thicker [33], central region of the sheet seems to be initially inhibited as is visible when comparing $t_{VP} = 17\,\text{ns}$ with 21 ns. The bright feature most clearly visible at $t_{VP} = 31\,\text{ns}$ appears to be plasma emission, indicating the presence of a significantly absorbing plasma that leads to a local plasma shielding of the sheet. The eventual "disappearance" of the central part of the sheet might be, not due to "direct" evaporation, but due to a propulsion and fragmentation by the expansion of the generated plasma.

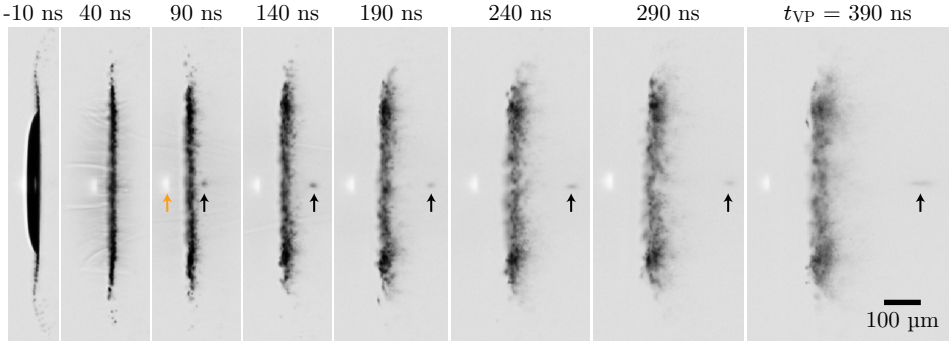

Figure A.16: Vaporization of a sheet target (corresponding to target B_{II} from Chap. 7) with a relatively high-intensity, temporally Gaussian-shaped vaporization pulse ($\tau_p = 10\,ns$, $E = 10\,mJ$). The center mass remnant, also discussed in Chap. 7, is propelled relative to the sheet target after a plasma forms on its surface. The rest of the sheet vaporizes before reaching the plasma threshold. The orange arrow indicates the emission from this plasma in one frame only, and the black arrow indicates the propelled center mass. Images are cropped in a frame co-moving with the target. Time label above each column is t_{VP}, the time relative to the onset of the VP.

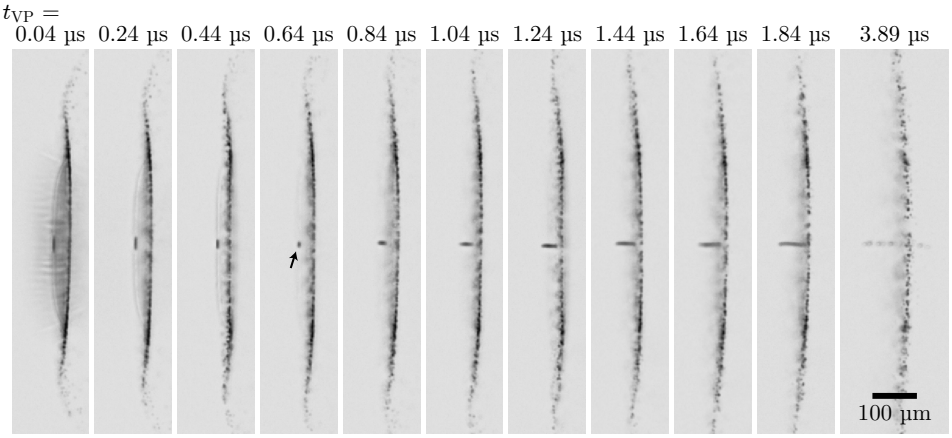

Figure A.17: Vaporization of a sheet target (corresponding to target B_{II} from Chap. 7) with a temporally square-shaped vaporization pulse ($\tau_p = 50\,ns$, $E = 3\,mJ$). As the thin sheet is vaporized, the oblate-shaped center mass remnant becomes detached and starts contracting. After approximately 640 ns the remnant appears to be close to spherical in shape (indicated by the arrow). It continues to deform into a prolate shape and later breaks up in a series of smaller fragments. Images are cropped in a frame co-moving with the target. The time label above each column is t_{VP}, the time relative to the onset of the VP.

Bibliography

[1] Theoi Greek Mythology, *Prometheus,* https://www.theoi.com/Titan/TitanPrometheus.html, accessed: 2021-01-14.

[2] S. Fry, *Mythos*, Vol. 1 (Chronicle Books, 2019).

[3] DOMO, *Data Never Sleeps 8.0,* https://www.domo.com/learn/data-never-sleeps-8 (2020), accessed: 2021-01-13.

[4] P. Van Zant, *Microchip fabrication* (McGraw-Hill Education, 2014).

[5] E. Abbe, *Beiträge zur Theorie des Mikroskops und der mikroskopischen Wahrnehmung,* Archiv für mikroskopische Anatomie **9**, 413 (1873).

[6] B. Wu and A. Kumar, *Extreme ultraviolet lithography: A review,* Journal of Vacuum Science & Technology B: Microelectronics and Nanometer Structures **25**, 1743 (2007).

[7] V. Bakshi, *EUV sources for lithography*, Vol. 149 (SPIE press, 2006).

[8] H. Kinoshita and O. Wood, *EUV lithography: An Historical Perspective,* in *EUV Lithography*, edited by V. Bakshi (SPIE press, 2018) 2nd ed., Chap. 1, pp. 1–55.

[9] T. W. Barbee, S. Mrowka, and M. C. Hettrick, *Molybdenum-silicon multilayer mirrors for the extreme ultraviolet,* Applied Optics **24**, 883 (1985).

[10] R. P. Seisyan, *Nanolithography in microelectronics: A review,* Technical Physics **56**, 1061 (2011).

[11] C. Wagner and N. Harned, *EUV lithography: Lithography gets extreme,* Nature Photonics **4**, 24 (2010).

[12] M. A. van de Kerkhof, H. Jasper, L. Levasier, R. Peeters, R. van Es, J.-W. Bosker, A. Zdravkov, E. Lenderink, F. Evangelista, P. Broman, B. Bilski, and T. Last, *Enabling sub-10nm node lithography: presenting the NXE:3400B EUV scanner,* Extreme Ultraviolet (EUV) Lithography VIII **10143**, 101430D (2017).

[13] I. V. Fomenkov, D. C. Brandt, A. I. Ershov, A. A. Schafgans, Y. Tao, and G. O. Vaschenko, *EUV Sources for High-Volume Manufacturing,* in *EUV Lithography*, edited by V. Bakshi (2018) 2nd ed., Chap. 3A, pp. 109–156.

[14] I. V. Fomenkov, A. A. Schafgans, and D. C. Brandt, *Laser-Produced Plasma Sources for High-Volume-Manufacturing EUV Lithography,* Synchrotron Radiation News **32**, 3 (2019).

[15] M. M. van Herpen, D. J. Klunder, W. A. Soer, R. Moors, and V. Banine, *Sn etching with hydrogen radicals to clean EUV optics,* Chemical Physics Letters **484**, 197 (2010).

[16] I. V. Fomenkov, D. C. Brandt, A. I. Ershov, A. A. Schafgans, Y. Tao, G. O. Vaschenko, S. I. Rokitski, M. Kats, M. Vargas, M. A. Purvis, R. J. Rafac, B. La Fontaine, S. De Dea, A. LaForge, J. Stewart, S. Chang, M. Graham, D. J. Riggs, T. Taylor, M. Abraham, and D. Brown, *Light sources for high-volume manufacturing EUV lithography: Technology, performance, and power scaling,* Advanced Optical Technologies **6**, 173 (2017).

[17] S. S. Harilal, B. O'Shay, Y. Tao, and M. S. Tillack, *Ion debris mitigation from tin plasma using ambient gas, magnetic field and combined effects,* Applied Physics B: Lasers and Optics **86**, 547 (2007).

[18] T. Saito, Y. Ueno, T. Yabu, D. Kurilovich, S. Nagai, T. Yanagida, T. Hori, Y. Kawasuji, T. Abe, T. Kodama, H. Nakarai, T. Yamazaki, and H. Mizoguchi, *LPP-EUV light source for HVM lithography,* in *Proceedings of SPIE*, Vol. 10254, edited by D. Schuoecker, R. Majer, and J. Brunnbauer (2017) pp. 102541A–3.

[19] D. Kurilovich, *Laser-induced dynamics of liquid tin microdroplets*, Ph.D. thesis, Vrije Universiteit Amsterdam (2019).

[20] H. Tanaka, A. Matsumoto, K. Akinaga, A. Takahashi, and T. Okada, *Comparative study on emission characteristics of extreme ultraviolet radiation from CO 2 and Nd:YAG laser-produced tin plasmas,* Applied Physics Letters **87**, 041503 (2005).

[21] V. Banine, K. N. Koshelev, and P. M. Swinkels, *Physical processes in EUV sources for microlithography,* J. Phys. D: Appl. Phys. **44**, 253001 (2011).

[22] R. Schupp, F. Torretti, R. A. Meijer, M. Bayraktar, J. Scheers, D. Kurilovich, A. Bayerle, K. S. E. Eikema, S. Witte, W. Ubachs, R. Hoekstra, and O. O. Versolato, *Efficient Generation of Extreme Ultraviolet Light From Nd:YAG-Driven Microdroplet-Tin Plasma,* Physical Review Applied **12**, 014010 (2019).

[23] G. Niimi, S. Nagai, T. Hori, Y. Ueno, T. Yamazaki, K. Miyao, H. Hayashi, Y. Watanabe, T. Abe, H. Nakarai, T. Saito, and H. Mizoguchi, *Update of development progress of the high power LPP EUV light source using a magnetic field,* Journal of Photopolymer Science and Technology Volume **33**, 37 (2020).

[24] R. Kodama, T. Mochizuki, K. A. Tanaka, and C. Yamanaka, *Enhancement of keV x-ray emission in laser-produced plasmas by a weak prepulse laser,* Applied Physics Letters **50**, 720 (1987).

[25] R. Weber and J. E. Balmer, *Soft x-ray emission from double-pulse laser-produced plasma,* Journal of Applied Physics **65**, 1880 (1989).

[26] M. Berglund, L. Rymell, and H. M. Hertz, *Ultraviolet prepulse for enhanced x-ray emission and brightness from droplet-target laser plasmas,* Applied Physics Letters **69**, 1683 (1996).

[27] S. Düsterer, H. Schwoerer, W. Ziegler, D. Salzmann, and R. Sauerbrey, *Effects of a prepulse on laser-induced EUV radiation conversion efficiency,* Applied Physics B: Lasers and Optics **76**, 17 (2003).

[28] J. R. Freeman, S. S. Harilal, and A. Hassanein, *Enhancements of extreme ultraviolet emission using prepulsed Sn laser-produced plasmas for advanced lithography applications,* Journal of Applied Physics **110**, 083303 (2011).

[29] S. Fujioka, M. Shimomura, Y. Shimada, S. Maeda, H. Sakaguchi, Y. Nakai, T. Aota, H. Nishimura, N. Ozaki, A. Sunahara, K. Nishihara, N. Miyanaga, Y. Izawa, and K. Mima, *Pure-tin microdroplets irradiated with double laser pulses for efficient and minimum-mass extreme-ultraviolet light source production,* Applied Physics Letters **92**, 241502 (2008).

[30] H. Gelderblom, H. Lhuissier, A. L. Klein, W. Bouwhuis, D. Lohse, E. Villermaux, and J. H. Snoeijer, *Drop deformation by laser-pulse impact,* Journal of Fluid Mechanics **794**, 676 (2016).

[31] K. Nishihara, A. Sunahara, A. Sasaki, M. Nunami, H. Tanuma, S. Fujioka, Y. Shimada, K. Fujima, H. Furukawa, T. Kato, F. Koike, R. More, M. Murakami, T. Nishikawa, V. Zhakhovskii, K. Gamata, A. Takata, H. Ueda, H. Nishimura, Y. Izawa, N. Miyanaga, and K. Mima, *Plasma physics and radiation hydrodynamics in developing an extreme ultraviolet light source of lithography,* Physics of Plasmas **15**, 056708 (2008).

[32] D. Kurilovich, A. L. Klein, F. Torretti, A. Lassise, R. Hoekstra, W. Ubachs, H. Gelderblom, and O. O. Versolato, *Plasma Propulsion of a Metallic Microdroplet and its Deformation upon Laser Impact,* Physical Review Applied **6**, 014018 (2016), arXiv:1604.00214 .

[33] B. Liu, D. Kurilovich, H. Gelderblom, and O. O. Versolato, *Mass Loss from a Stretching Semitransparent Sheet of Liquid Tin,* Physical Review Applied **13**, 024035 (2020).

[34] J. Fujimoto, T. Hori, T. Yamazaki, and H. Mizoguchi, *Development of laser-produced tin plasma-based EUV light source technology for HVM EUV lithography,* Physics Research International **2012**, 249495 (2012).

[35] Y. Tao, J. T. Stewart, J. Jur, A. LaForge, D. Brown, M. J. Arcand, A. A. Schafgans, and M. A. Purvis, *Extreme ultraviolet light source,* ASML Netherlands B.V., US Patent 20160007434A1.

[36] M. S. Krivokorytov, A. Yu Vinokhodov, Y. V. Sidelnikov, V. M. Krivtsun, V. O. Kompanets, A. A. Lash, K. N. Koshelev, V. V. Medvedev, and A. Y. Vinokhodov, *Cavitation and spallation in liquid metal droplets produced by subpicosecond pulsed laser radiation,* Physical Review E **95**, 031101 (2017).

[37] D. Kurilovich, T. de Faria Pinto, F. Torretti, R. Schupp, J. Scheers, A. S. Stodolna, H. Gelderblom, K. S. E. Eikema, S. Witte, W. Ubachs, R. Hoekstra, and O. O. Versolato, *Expansion Dynamics After Laser-Induced Cavitation in Liquid Tin Microdroplets,* Physical Review Applied **10**, 054005 (2018), arXiv:1805.07283 .

[38] O. O. Versolato, *Physics of laser-driven tin plasma sources of EUV radiation for nanolithography,* Plasma Sources Science and Technology **28**, 083001 (2019).

[39] S. Y. Grigoryev, B. V. Lakatosh, M. S. Krivokorytov, V. V. Zhakhovsky, S. A. Dyachkov, D. K. Ilnitsky, K. P. Migdal, N. A. Inogamov, A. Y. Vinokhodov, V. O. Kompanets, Y. V. Sidelnikov, V. M. Krivtsun, K. N. Koshelev, and V. V. Medvedev, *Expansion and fragmentation of liquid metal droplet by a short laser pulse,* Physical Review Applied **10**, 064009 (2018), arXiv:1807.01862 .

[40] M. M. Basko, V. G. Novikov, and A. S. Grushin, *On the structure of quasi-stationary laser ablation fronts in strongly radiating plasmas,* Physics of Plasmas **22**, 053111 (2015).

[41] S. A. Reijers, D. Kurilovich, F. Torretti, H. Gelderblom, and O. O. Versolato, *Laser-to-droplet alignment sensitivity relevant for laser-produced plasma sources of extreme ultraviolet light,* Journal of Applied Physics **124**, 013102 (2018), arXiv:1805.05647v2 .

[42] R. A. Meijer, A. S. Stodolna, K. S. E. Eikema, and S. Witte, *High-energy Nd:YAG laser system with arbitrary sub-nanosecond pulse shaping capability,* Optics Letters **42**, 2758 (2017).

[43] D. Goswami, *Optical pulse shaping approaches to coherent control,* Physics Reports **374**, 385 (2003).

[44] W. S. Warren, H. Rabitz, and M. Dahleh, *Coherent Control of Quantum Dynamics: The Dream Is Alive,* Science **259**, 1581 (1993).

[45] A. Assion, *Control of Chemical Reactions by Feedback-Optimized Phase-Shaped Femtosecond Laser Pulses,* Science **282**, 919 (1998).

[46] K. Pangovski, M. Sparkes, A. Cockburn, W. O'Neill, Peh Siong Teh, D. Lin, and D. J. Richardson, *Control of Material Transport Through Pulse Shape Manipulation-A Development Toward Designer Pulses,* IEEE Journal of Selected Topics in Quantum Electronics **20**, 51 (2014).

[47] P. Deladurantaye, D. Gay, A. Cournoyer, V. Roy, B. Labranche, M. Levesque, and Y. Taillon, *Material micromachining using a pulsed fiber laser platform with fine temporal nanosecond pulse shaping capability,* in *SPIE Fiber Lasers VI: Technology, Systems, and Applications*, Vol. 7195, edited by D. V. Gapontsev, D. A. Kliner, J. W. Dawson, and K. Tankala (2009) p. 71951S.

[48] O. A. Hurricane, D. A. Callahan, D. T. Casey, P. M. Celliers, C. Cerjan, E. L. Dewald, T. R. Dittrich, T. Döppner, D. E. Hinkel, L. F. B. Hopkins, J. L. Kline, S. Le Pape, T. Ma, A. G. MacPhee, J. L. Milovich, A. Pak, H.-S. Park, P. K. Patel, B. A. Remington, J. D. Salmonson, P. T. Springer, and R. Tommasini, *Fuel gain exceeding unity in an inertially confined fusion implosion,* Nature **506**, 343 (2014).

[49] G. V. Cojocaru, R. G. Ungureanu, R. A. Banici, D. Ursescu, O. Guilbaud, O. Delmas, A. Le Marec, O. Neveu, J. Demailly, M. Pittman, S. Kazamias, S. Daboussi, K. Cassou, L. Li, A. Klisnick, P. Zeitoun, and D. Ros, *One long and two short pumping pulses control for plasma x-ray amplifier optimization,* Optics Express **24**, 14260 (2016).

[50] K. M. Nowak, Y. Kurosawa, T. Suganuma, Y. Kawasuji, H. Nakarai, T. Saito, J. Fujimoto, and H. Mizoguchi, *Synthesis of arbitrary pulse waveforms in QCL-seeded ns-pulse CO2 laser for optimization of an LPP EUV source,* Optics Letters **41**, 3118 (2016).

[51] S. Yuspeh, K. L. Sequoia, Y. Tao, M. S. Tillack, R. A. Burdt, and F. Najmabadi, *Heating dynamics and extreme ultraviolet radiation emission of laser-produced Sn plasmas,* Applied Physics Letters **96**, 261501 (2010).

[52] J. Fülöp, Z. Major, B. Horváth, F. Tavella, A. Baltuška, and F. Krausz, *Shaping of picosecond pulses for pumping optical parametric amplification,* Applied Physics B **87**, 79 (2007).

[53] Yong Kong, Qi Zhong Liu, Chen Deng, Xiu Jiang Huang, and Guang Hui Chen, *64-Channel Optical Pulse Stacker,* Journal of Lightwave Technology **27**, 3017 (2009).

[54] A. Malinowski, K. T. Vu, K. K. Chen, J. Nilsson, Y. Jeong, S. Alam, D. Lin, and D. J. Richardson, *High power pulsed fiber MOPA system incorporating electro-optic modulator based adaptive pulse shaping,* Optics Express **17**, 20927 (2009).

[55] C. E. Rogers and P. L. Gould, *Nanosecond pulse shaping at 780 nm with fiber-based electro-optical modulators and a double-pass tapered amplifier,* Optics Express **24**, 2596 (2016), arXiv:1511.01228 .

[56] M. Nie, Q. Liu, E. Ji, X. Cao, X. Fu, and M. Gong, *Active pulse shaping for end-pumped Nd:YVO4 amplifier with high gain,* Optics Letters **42**, 1051 (2017).

[57] J. Morgenweg and K. S. E. Eikema, *A 1.8 mJ, picosecond Nd:YVO 4 bounce amplifier pump front-end system for high-accuracy XUV-frequency comb spectroscopy,* Laser Physics Letters **9**, 781 (2012).

[58] W. Koechner, *Springer Series in Optical Sciences*, 6th ed., 1 (Springer, 2014) p. 750.

[59] J. Sherman, *Thermal compensation of a cw-pumped Nd:YAG laser,* Applied Optics **37**, 7789 (1998).

[60] J. Jeong, S. Cho, and T. J. Yu, *Numerical extension of Frantz–Nodvik equation for double-pass amplifiers with pulse overlap,* Optics Express **25**, 3946 (2017).

[61] T. Baumert, T. Brixner, V. Seyfried, M. Strehle, and G. Gerber, *Femtosecond pulse shaping by an evolutionary algorithm with feedback,* Applied Physics B: Lasers and Optics **65**, 779 (1997).

[62] F. Torretti, J. Sheil, R. Schupp, M. M. Basko, M. Bayraktar, R. A. Meijer, S. Witte, W. Ubachs, R. Hoekstra, O. O. Versolato, A. J. Neukirch, and J. Colgan, *Prominent radiative contributions from multiply-excited states in laser-produced tin plasma for nanolithography,* Nature Communications **11**, 2334 (2020).

[63] J. Scheers, R. Schupp, R. A. Meijer, W. Ubachs, R. Hoekstra, and O. O. Versolato, *Time- and space-resolved optical Stark spectroscopy in the afterglow of laser-produced tin-droplet plasma,* Physical Review E **102**, 13204 (2020).

[64] R. Schupp, F. Torretti, R. A. Meijer, M. Bayraktar, J. Sheil, J. Scheers, D. Kurilovich, A. Bayerle, A. A. Schafgans, M. A. Purvis, K. S. E. Eikema, S. Witte, W. Ubachs, R. Hoekstra, and O. O. Versolato, *Radiation transport and scaling of optical depth in Nd:YAG laser-produced microdroplet-tin plasma,* Applied Physics Letters **115**, 124101 (2019).

[65] L. Behnke, R. Schupp, Z. Bouza, M. Bayraktar, Z. Mazzotta, R. Meijer, J. Sheil, S. Witte, W. Ubachs, R. Hoekstra, and O. O. Versolato, *Extreme ultraviolet light from a tin plasma driven by a 2-μm-wavelength laser,* Optics Express **29**, 4475 (2021).

[66] L. M. Frantz and J. S. Nodvik, *Theory of pulse propagation in a laser amplifier,* Journal of Applied Physics **34**, 2346 (1963).

[67] D. N. Schimpf, C. Ruchert, D. Nodop, J. Limpert, A. Tünnermann, and F. Salin, *Compensation of pulse-distortion in saturated laser amplifiers,* Optics Express **16**, 17637 (2008).

[68] G. Sobon, P. Kaczmarek, A. Antonczak, J. Sotor, A. Waz, and K. M. Abramski, *Pulsed dual-stage fiber MOPA source operating at 1550 nm with arbitrarily shaped output pulses,* Applied Physics B: Lasers and Optics **105**, 721 (2011).

[69] A. Agnesi, L. Carrà, P. Dallocchio, F. Pirzio, G. Reali, S. Lodo, and G. Piccinno, *50-mJ macro-pulses at 1064 nm from a diode-pumped picosecond laser system.* Optics Express **19**, 20316 (2011).

[70] M. Michalska, J. Swiderski, and M. Mamajek, *Arbitrary pulse shaping in Er-doped fiber amplifiers - Possibilities and limitations,* Optics and Laser Technology **60**, 8 (2014).

[71] Z. Li, A. M. Heidt, P. S. Teh, M. Berendt, J. K. Sahu, R. Phelan, B. Kelly, S. U. Alam, and D. J. Richardson, *High-energy diode-seeded nanosecond 2 μm fiber MOPA systems incorporating active pulse shaping,* Optics Letters **39**, 1569 (2014).

[72] R. J. St. Pierre, G. W. Holleman, M. Valley, H. Injeyan, J. G. Berg, G. M. Harpole, R. C. Hilyard, M. Mitchell, M. E. Weber, J. Zamel, T. Engler, D. Hall, R. Tinti, and J. Machan, *Active Tracker Laser (ATLAS),* IEEE Journal on Selected Topics in Quantum Electronics **3**, 64 (1997).

[73] S. Pearce, C. L. Ireland, and P. E. Dyer, *Simplified analysis of double-pass amplification with pulse overlap and application to Nd:YVO4 laser,* Optics Communications **255**, 297 (2005).

[74] M. Li, X. M. Zhang, Z. G. Wang, X. D. Cui, X. W. Yan, X. Y. Jiang, J. G. Zheng, W. Wang, and M. Li, *Analytical and numerical solutions to the amplifier with incoherent pulse temporal overlap,* Optics Communications **382**, 49 (2017).

[75] Y. Hirano, N. Pavel, S. Yamamoto, Y. Koyata, and T. Tajime, *100-W class diode-pumped Nd:YAG MOPA system with a double-stage relay-optics scheme,* Optics Communications **170**, 275 (1999).

[76] A. Y. Vinokhodov, K. N. Koshelev, V. M. Krivtsun, M. S. Krivokorytov, Y. V. Sidelnikov, V. V. Medvedev, V. O. Kompanets, A. A. Melnikov, and S. V. Chekalin, *Formation of a fine-dispersed liquid-metal target under the action of femto- and picosecond laser pulses for a laser-plasma radiation source in the extreme ultraviolet range,* Quantum Electronics **46**, 23 (2016).

[77] A. L. Klein, D. Kurilovich, H. Lhuissier, O. O. Versolato, D. Lohse, E. Villermaux, and H. Gelderblom, *Drop fragmentation by laser-pulse impact,* Journal of Fluid Mechanics **893**, A7(37) (2020), arXiv:1910.02522 .

[78] Y. Kawasuji, K. M. Nowak, T. Hori, T. Okamoto, H. Tanaka, Y. Watanabe, T. Abe, T. Kodama, Y. Shiraishi, H. Nakarai, T. Yamazaki, S. Okazaki, T. Saitou, and H. Mizoguchi, *Key components technology update of the 250W high-power LPP-EUV light source,* in *Proc. of SPIE*, Vol. 10143 (2017) p. 101432G.

[79] K. Tomita, Y. Sato, S. Tsukiyama, T. Eguchi, K. Uchino, K. Kouge, H. Tomuro, T. Yamazaki, Y. Wada, M. Kunishima, G. Soumagne, T. Kodama, H. Mizoguchi, A. Sunahara, and K. Nishihara, *Time-resolved two-dimensional profiles of electron density and temperature of laser-produced tin plasmas for extreme-ultraviolet lithography light sources,* Scientific Reports **7**, 12328 (2017).

[80] Y. Sato, K. Tomita, S. Tsukiyama, T. Eguchi, K. Uchino, K. Kouge, H. Tomuro, T. Yamazaki, Y. Wada, M. Kunishima, T. Kodama, and H. Mizoguchi, *Spatial profiles of electron density, electron temperature, average ionic charge, and EUV emission of laser-produced Sn plasmas for EUV lithography,* Japanese Journal of Applied Physics **56**, 036201 (2017).

[81] M. S. Krivokorytov, Q. Zeng, B. V. Lakatosh, A. Y. Vinokhodov, Y. V. Sidelnikov, V. O. Kompanets, V. M. Krivtsun, K. N. Koshelev, C. D. Ohl, and V. V. Medvedev, *Shaping and Controlled Fragmentation of Liquid Metal Droplets through Cavitation,* Scientific Reports **8**, 597 (2018).

[82] T. de Faria Pinto, J. Mathijssen, R. Meijer, H. Zhang, A. Bayerle, D. Kurilovich, O. O. Versolato, K. S. E. Eikema, and S. Witte, *Cylindrically and non-cylindrically symmetric expansion dynamics of tin microdroplets after ultrashort laser pulse impact,* Applied Physics A **127**, 93 (2021).

[83] M. M. Basko, M. S. Krivokorytov, A. Yu Vinokhodov, Y. V. Sidelnikov, V. M. Krivtsun, V. V. Medvedev, D. A. Kim, V. O. Kompanets, A. A. Lash, K. N. Koshelev, and A. Y. Vinokhodov, *Fragmentation dynamics of liquid-metal droplets under ultra-short laser pulses,* Laser Physics Letters **14**, 036001 (2017).

[84] C. A. Stan, P. R. Willmott, H. A. Stone, J. E. Koglin, M. Liang, A. L. Aquila, J. S. Robinson, K. L. Gumerlock, G. Blaj, R. G. Sierra, S. Boutet, S. A. Guillet, R. H. Curtis, S. L. Vetter, H. Loos, J. L. Turner, and F. J. Decker, *Negative Pressures and Spallation in Water Drops Subjected to Nanosecond Shock Waves,* Journal of Physical Chemistry Letters **7**, 2055 (2016).

[85] C. A. Stan, D. Milathianaki, H. Laksmono, R. G. Sierra, T. A. McQueen, M. Messerschmidt, G. J. Williams, J. E. Koglin, T. J. Lane, M. J. Hayes, S. A. Guillet, M. Liang, A. L. Aquila, P. R. Willmott, J. S. Robinson, K. L. Gumerlock, S. Botha, K. Nass, I. Schlichting, R. L. Shoeman, H. A. Stone, and S. Boutet, *Liquid explosions induced by X-ray laser pulses,* Nature Physics **12**, 966 (2016).

[86] G. E. Duvall, *Concepts of Shock Wave Propagation,* Bulletin of the Seismological Society of America **52**, 869 (1962).

[87] A. E. Mayer and P. N. Mayer, *Strain rate dependence of spall strength for solid and molten lead and tin,* International Journal of Fracture **222**, 171 (2020).

[88] M. A. Meyers and C. Taylor Aimone, *Dynamic fracture (spalling) of metals,* Progress in Materials Science **28**, 1 (1983).

[89] S. Eliezer, I. Gilath, and T. Bar-Noy, *Laser-induced spall in metals: Experiment and simulation,* Journal of Applied Physics **67**, 715 (1990).

[90] T. de Faria Pinto, J. Mathijssen, K. S. E. Eikema, and S. Witte, *Optical parametric chirped pulse amplifier producing ultrashort 10.5 mJ pulses at 1.55 μm,* Optics Express **27**, 29829 (2019).

[91] L. Balazs, R. Gijbels, and A. Vertes, *Expansion of Laser-Generated Plumes Near the Plasma Ignition Threshold,* Analytical Chemistry **63**, 314 (1991).

[92] D. Autrique, G. Clair, D. L'Hermite, V. Alexiades, A. Bogaerts, and B. Rethfeld, *The role of mass removal mechanisms in the onset of ns-laser induced plasma formation,* Journal of Applied Physics **114**, 023301 (2013).

[93] D. Kurilovich, M. M. Basko, D. A. Kim, F. Torretti, R. Schupp, J. C. Visschers, J. Scheers, R. Hoekstra, W. Ubachs, and O. O. Versolato, *Power-law scaling of plasma pressure on laser-ablated tin microdroplets,* Physics of Plasmas **25**, 012709 (2018), arXiv:1710.11426 .

[94] S. A. Reijers, J. H. Snoeijer, and H. Gelderblom, *Droplet deformation by short laser-induced pressure pulses,* Journal of Fluid Mechanics **828**, 374 (2017), arXiv:1702.01538 .

[95] G. Cisneros, J. S. Helman, and C. N. Wagner, *Dielectric function of liquid tin between 250 and 1100 °C,* Physical Review B **25**, 4248 (1982).

[96] D. Nakamura, K. Tamaru, Y. Hashimoto, T. Okada, H. Tanaka, and A. Takahashi, *Mitigation of fast ions generated from laser-produced Sn plasma for extreme ultraviolet light source by H2 gas,* Journal of Applied Physics **102**, 123310 (2007).

[97] A. Bayerle, M. J. Deuzeman, S. van der Heijden, D. Kurilovich, T. de Faria Pinto, A. S. Stodolna, S. Witte, K. S. E. Eikema, W. Ubachs, R. Hoekstra, and O. O. Versolato, *Sn ion energy distributions of ns- and ps-laser produced plasmas,* Plasma Sources Science and Technology **27**, 045001 (2017), arXiv:1711.02342 .

[98] A. S. Stodolna, T. de Faria Pinto, F. Ali, A. Bayerle, D. Kurilovich, J. Mathijssen, R. Hoekstra, O. O. Versolato, K. S. E. Eikema, and S. Witte, *Controlling ion kinetic energy distributions in laser produced plasma sources by means of a picosecond pulse pair,* Journal of Applied Physics **124**, 053303 (2018).

[99] D. Hudgins and R. S. Abhari, *Rupture time of droplets impacted by a burst of picosecond laser pulses,* Physical Review E **99**, 031102(R) (2019).

[100] A. L. Klein, W. Bouwhuis, C. W. Visser, H. Lhuissier, C. Sun, J. H. Snoeijer, E. Villermaux, D. Lohse, and H. Gelderblom, *Drop Shaping by Laser-Pulse Impact,* Physical Review Applied **3**, 044018 (2015).

[101] D. Hudgins, *Advanced Irradiation Schemes for Target Shaping in Droplet-Based Laser-Produced Plasma Light Sources*, Ph.D. thesis, ETH Zürich (2019).

[102] W. Lauterborn and C. D. Ohl, *Cavitation bubble dynamics.* Ultrasonics Sonochemistry **4**, 65 (1997).

[103] C. D. Ohl and R. Ikink, *Shock-Wave-Induced Jetting of Micron-Size Bubbles,* Physical Review Letters **90**, 214502 (2003).

[104] G. N. Sankin, W. N. Simmons, S. L. Zhu, and P. Zhong, *Shock wave interaction with laser-generated single bubbles,* Physical Review Letters **95**, 034501 (2005).

[105] D. Obreschkow, P. Kobel, N. Dorsaz, A. De Bosset, C. Nicollier, and M. Farhat, *Cavitation bubble dynamics inside liquid drops in microgravity,* Physical Review Letters **97**, 094502 (2006).

[106] E. Villermaux and B. Bossa, *Drop fragmentation on impact,* Journal of Fluid Mechanics **668**, 412 (2011).

[107] A. Loeb and S. Eliezer, *An analytical model for creation and decay of strong shock waves caused by a trapezoidal laser pulse,* Physics of Fluids **28**, 1196 (1985).

[108] R. A. Meijer, R. Schupp, J. Sheil, M. M. Basko, K. S. E. Eikema, O. O. Versolato, and S. Witte, *Spall-velocity reduction in double-pulse impact on tin microdroplets,* Phys. Rev. Applied **16**, 024026 (2021).

[109] D. Hudgins, N. Gambino, B. Rollinger, and R. S. Abhari, *Neutral cluster debris dynamics in droplet-based laser-produced plasma sources,* Journal of Physics D: Applied Physics **49**, 185205 (2016).

[110] C. D. Ohl, *Cavitation inception following shock wave passage,* Physics of Fluids **14**, 3512 (2002).

[111] T. De Rességuier, L. Signor, A. Dragon, P. Severin, and M. Boustie, *Spallation in laser shock-loaded tin below and just above melting on release,* Journal of Applied Physics **102**, 073535 (2007).

[112] M. A. Purvis, I. V. Fomenkov, A. A. Schafgans, P. Mayer, K. Hummler, M. H. Leenders, Y. Tao, S. I. Rokitski, J. Stewart, A. I. Ershov, R. J. Rafac, S. De Dea, G. O. Vaschenko, D. C. Brandt, and D. J. Brown, *Laser-produced plasma incoherent EUV light sources for high-volume manufacturing semiconductor lithography (Conference Presentation),* in *X-Ray Lasers and Coherent X-Ray Sources: Development and Applications XIII*, Vol. 11111, edited by A. Klisnick and C. S. Menoni, International Society for Optics and Photonics (SPIE, 2019) p. 19.

[113] M. M. Basko, *On the theory and numerical modeling of spall fracture in pure liquids,* arXiv , 1 (2021), arXiv:2102.01548 .

[114] Y. B. Zel'Dovich and Y. P. Raizer, *Physics of shock waves and high-temperature hydrodynamic phenomena* (Courier Corporation, 2002).

[115] M. J. Assael, A. E. Kalyva, K. D. Antoniadis, R. Michael Banish, I. Egry, J. Wu, E. Kaschnitz, and W. A. Wakeham, *Reference data for the density and viscosity of liquid copper and liquid tin,* Journal of Physical and Chemical Reference Data **39**, 033105 (2010).

[116] P. W. Humrickhouse, *An Equation of State and Compendium of Thermophysical Properties of Liquid Tin, a Prospective Plasma-Facing Material,* IEEE Transactions on Plasma Science **47**, 3374 (2019).

[117] D. E. Grady, *Physics of Shock and Impact, Volume 1; Fundamentals and dynamic failure* (IOP Publishing, 2017).

[118] M. M. Basko, J. Maruhn, and A. Tauschwitz, *An efficient cell-centered diffusion scheme for quadrilateral grids,* Journal of Computational Physics **228**, 2175 (2009).

[119] M. M. Basko, J. Maruhn, and A. Tauschwitz, *Development of a 2D radiation-hydrodynamics code RALEF for laser plasma simulations GSI Report 2010–1,* PLASMA-PHYSICS **25**, 410 (2010).

[120] M. M. Basko, P. V. Sasorov, M. Murakami, V. G. Novikov, and A. S. Grushin, *One-dimensional study of the radiation-dominated implosion of a cylindrical tungsten plasma column,* Plasma Physics and Controlled Fusion **54**, 055003 (2012).

[121] M. M. Basko, *On the maximum conversion efficiency into the 13.5-nm extreme ultraviolet emission under a steady-state laser ablation of tin microspheres,* Physics of Plasmas **23**, 083114 (2016).

[122] J. R. Blake and D. C. Gibson, *Growth and Collapse of A Vapour Cavity Near A Free Surface,* Journal of Fluid Mechanics **111**, 123 (1981).

[123] P. B. Robinson, J. R. Blake, T. Kodama, A. Shima, and Y. Tomita, *Interaction of cavitation bubbles with a free surface,* Journal of Applied Physics **89**, 8225 (2001).

[124] S. T. Thoroddsen, K. Takehara, T. G. Etoh, and C. D. Ohl, *Spray and microjets produced by focusing a laser pulse into a hemispherical drop,* Physics of Fluids **21**, 112101 (2009).

[125] E. Klaseboer, S. W. Fong, C. K. Turangan, B. C. Khoo, J. Andrew, M. L. Calvisi, G. N. Sankin, and P. Zhong, *Interaction of lithotripter shockwaves with single inertial cavitation bubbles,* J. Fluid. Mech. **593**, 33 (2007).

[126] A. Antkowiak, N. Bremond, S. Le Dizès, and E. Villermaux, *Short-term dynamics of a density interface following an impact,* Journal of Fluid Mechanics **577**, 241 (2007).

[127] G. J. Ball, B. P. Howell, T. G. Leighton, and M. J. Schofield, *Shock-induced collapse of a cylindrical air cavity in water: A Free-Lagrange simulation,* Shock Waves **10**, 265 (2000).

[128] J. F. Haas, *Interaction of Weak Shock Waves With Cylindrical And Spherical Gas Inhomogeneities,* Journal of Fluid Mechanics **181**, 41 (1987).

[129] I. R. Peters, Y. Tagawa, N. Oudalov, C. Sun, A. Prosperetti, D. Lohse, and D. Van Der Meer, *Highly focused supersonic microjets: Numerical simulations,* Journal of Fluid Mechanics **719**, 587 (2013), arXiv:1203.5029 .

[130] G. Xiang and B. Wang, *Numerical study of a planar shock interacting with a cylindrical water column embedded with an air cavity,* Journal of Fluid Mechanics **825**, 825 (2017).

[131] Y. Zhu, Z. Yang, K. H. Luo, J. Pan, and Z. Pan, *Numerical investigation of planar shock wave impinging on spherical gas bubble with different densities,* Physics of Fluids **31**, 056101 (2019).

[132] Y. Liang, Y. Jiang, C. Y. Wen, and Y. Liu, *Interaction of a planar shock wave and a water droplet embedded with a vapour cavity,* Journal of Fluid Mechanics **885**, R6(13) (2020).

[133] S. R. G. Avila and C. D. Ohl, *Fragmentation of acoustically levitating droplets by laser-induced cavitation bubbles,* Journal of Fluid Mechanics **805**, 551 (2016).

[134] G. Birkhoff, D. P. MacDougall, E. M. Pugh, and G. Taylor, *Explosives with lined cavities,* Journal of Applied Physics **19**, 563 (1948).

[135] A. Philipp, C. Scheffczyk, and A. Vogel, *Interaction of lithotripter-generated shock waves with air bubbles,* Journal of the Acoustical Society of America **93**, 2496 (1993).

[136] S. Mishra and V. Yadava, *Laser Beam MicroMachining (LBMM) - A review,* Optics and Lasers in Engineering **73**, 89 (2015).

[137] P. R. Willmott and J. R. Huber, *Pulsed laser vaporization and deposition,* Reviews of Modern Physics **72**, 315 (2000).

[138] A. J. Glass and A. H. Guenther, *Laser Induced Damage in Optical Materials,* in *Boulder damage symposium* (1976).

[139] D. W. Hahn and N. Omenetto, *Laser-induced breakdown spectroscopy (LIBS), part II: Review of instrumental and methodological approaches to material analysis and applications to different fields,* Applied Spectroscopy **66**, 347 (2012).

[140] P. Mora, *Theoretical model of absorption of laser light by a plasma,* Physics of Fluids **25**, 1051 (1982).

[141] O. Benavides, O. Lebedeva, and V. Golikov, *Reflection of nanosecond Nd:YAG laser pulses in ablation of metals,* Optics Express **19**, 21842 (2011).

[142] O. Benavides, L. d. l. C. May, and A. F. Gil, *A comparative study on reflection of nanosecond Nd-YAG laser pulses in ablation of metals in air and in vacuum,* Optics Express **21**, 13068 (2013).

[143] O. Benavides, L. De La Cruz May, A. Flores Gil, and J. A. Lugo Jimenez, *Experimental study on reflection of high-intensity nanosecond Nd:YAG laser pulses in ablation of metals,* Optics and Lasers in Engineering **68**, 83 (2015).

[144] Y. V. Afanasyev, O. N. Krokhin, and G. V. Sklizkov, *7A5—Evaporation and Heating of a Substance Due to Laser Radiation,* IEEE Journal of Quantum Electronics **2**, 483 (1966).

[145] H. M. J. Musal, *Thermomechanical Stress Degradation of Metal Mirror Surfaces Under Pulsed Laser Irradiation,* in *Laser Induced Damage in Optical Materials* (1979) pp. 159–173.

[146] A. Faghri and Y. Zhang, *Introduction To Transport Phenomena,* in *Transport Phenomena in Multiphase Systems* (2006) Chap. 1, pp. 1–106.

[147] B. N. Chichkov, C. Momma, S. Nolte, F. von Alvensleben, and A. Tünnermann, *Femtosecond, picosecond and nanosecond laser ablation of solids,* Applied Physics A Materials Science & Processing **63**, 109 (1996).

[148] I. V. Savchenko, S. V. Stankus, and A. S. Agadjanov, *Measurement of liquid tin heat transfer coefficients within the temperature range of 506-1170 K,* High Temperature **49**, 506 (2011).

[149] J. R. Bettis, R. A. I. House, and A. H. Guenther, *Spot Size and Pulse Duration Dependence of Laser-Induced Damage,* in *Laser Induced Damage in Optical Materials* (1976).

[150] D. Du, X. Liu, G. Korn, J. Squier, and G. Mourou, *Laser-induced breakdown by impact ionization in SiO2 with pulse widths from 7 ns to 150 fs,* Applied Physics Letters **64**, 3071 (1994).

[151] B. C. Stuart, M. D. Feit, A. M. Rubenchik, B. Shore, and M. D. Perry, *Laser-Induced Damage in Dielectrics with Nanosecond to Subpicosecond Pulses,* Physical Review Letters **74**, 2248 (1995).

[152] B. C. Stuart, M. D. Feit, S. Herman, A. M. Rubenchik, B. Shore, and M. Perry, *Nanosecond-to-femtosecond laser-induced breakdown in dielectrics,* Physical Review B - Condensed Matter and Materials Physics **53**, 1749 (1996).

[153] A. C. Tien, S. Backus, H. Kapteyn, M. M. Murnane, and G. Mourou, *Short-pulse laser damage in transparent materials as a function of pulse duration,* Physical Review Letters **82**, 3883 (1999).

[154] M. Aden, E. Beyer, G. Herziger, and H. Kunze, *Laser-Induced Vaporization of a Metal Surface,* Journal of Physics D: Applied Physics **25**, 57 (1992).

[155] E. G. Gamaly, A. V. Rode, B. Luther-Davies, and V. T. Tikhonchuk, *Ablation of solids by femtosecond lasers: Ablation mechanism and ablation thresholds for metals and dielectrics,* Physics of Plasmas **9**, 949 (2002).

[156] S. Sharafat and N. Ghoniem, *Summary of Thermo-Physical Properties of Sn, And Compounds of Sn-H, Sn-O, Sn-C, Sn-Li, and Sn-Si, And Comparison of Properties of Sn, Sn-Li, Li, and Pb-Li*, Tech. Rep. (University of California Los Angeles, 2000) UCLA-UCMEP-00-31.

[157] A. Miotello and R. Kelly, *Critical assessment of thermal models for laser sputtering at high fluences,* Applied Physics Letters **67**, 3535 (1995).

[158] Q. Lu, *Thermodynamic evolution of phase explosion during high-power nanosecond laser ablation,* Physical Review E - Statistical Physics, Plasmas, Fluids, and Related Interdisciplinary Topics **67**, 5 (2003).

[159] C. Porneala and D. A. Willis, *Effect of the dielectric transition on laser-induced phase explosion in metals,* International Journal of Heat and Mass Transfer **49**, 1928 (2006).

[160] C. Porneala and D. A. Willis, *Observation of nanosecond laser-induced phase explosion in aluminum,* Applied Physics Letters **89**, 211121 (2006).

[161] D. Marla, U. V. Bhandarkar, and S. S. Joshi, *Critical assessment of the issues in the modeling of ablation and plasma expansion processes in the pulsed laser deposition of metals,* Journal of Applied Physics **109**, 021101 (2011).

[162] F. Torretti, R. Schupp, D. Kurilovich, A. Bayerle, J. Scheers, W. Ubachs, R. Hoekstra, and O. O. Versolato, *Short-wavelength out-of-band EUV emission from Sn laser-produced plasma,* Journal of Physics B: Atomic, Molecular and Optical Physics **51**, 045005 (2018).

[163] A. Bogaerts, Z. Chen, R. Gijbels, and A. Vertes, *Laser ablation for analytical sampling: What can we learn from modeling?* Spectrochimica Acta - Part B Atomic Spectroscopy **58**, 1867 (2003).

[164] A. H. Lutey, *An improved model for nanosecond pulsed laser ablation of metals,* Journal of Applied Physics **114**, 083108 (2013).

[165] D. Marla, U. V. Bhandarkar, and S. S. Joshi, *A model of laser ablation with temperature-dependent material properties, vaporization, phase explosion and plasma shielding,* Applied Physics A: Materials Science and Processing **116**, 273 (2014).

[166] B. Liu, R. A. Meijer, J. Hernandez-Rueda, D. Kurilovich, Z. Mazzotta, S. Witte, and O. O. Versolato, *Laser-induced vaporization of a stretching sheet of liquid tin,* Journal of Applied Physics **129**, 053302 (2021).

[167] Y. Tao, M. S. Tillack, K. L. Sequoia, R. A. Burdt, S. Yuspeh, and F. Najmabadi, *Efficient 13.5 nm extreme ultraviolet emission from Sn plasma irradiated by a long CO2 laser pulse,* Applied Physics Letters **92**, 251501 (2008).

[168] J. Benschop, V. Banine, S. Lok, and E. Loopstra, *Extreme ultraviolet lithography: Status and prospects,* Journal of Vacuum Science & Technology B: Microelectronics and Nanometer Structures **26**, 2204 (2008).

[169] Y. Wang and L. Bourouiba, *Drop impact on small surfaces: Thickness and velocity profiles of the expanding sheet in the air,* Journal of Fluid Mechanics **814**, 510 (2017).

[170] Y. Wang, R. Dandekar, N. Bustos, S. Poulain, and L. Bourouiba, *Universal Rim Thickness in Unsteady Sheet Fragmentation,* Physical Review Letters **120**, 204503 (2018).

[171] Y. Wang and L. Bourouiba, *Unsteady sheet fragmentation: Droplet sizes and speeds,* Journal of Fluid Mechanics **848**, 946 (2018).

[172] A. Rozhkov, B. Prunet-Foch, and M. Vignes-Adler, *Dynamics of a liquid lamella resulting from the impact of a water drop on a small target,* Proceedings of the Royal Society A: Mathematical, Physical and Engineering Sciences **460**, 2681 (2004).

[173] J. Eggers, M. A. Fontelos, C. Josserand, and S. Zaleski, *Drop dynamics after impact on a solid wall: Theory and simulations,* Physics of Fluids **22**, 062101 (2010).

[174] H. Lastakowski, F. Boyer, A. L. Biance, C. Pirat, and C. Ybert, *Bridging local to global dynamics of drop impact onto solid substrates,* Journal of Fluid Mechanics **747**, 103 (2014).

[175] J. B. Blaisot and J. Yon, *Droplet size and morphology characterization for dense sprays by image processing: Application to the Diesel spray,* Experiments in Fluids **39**, 977 (2005).

[176] M. S. Qaisar and G. J. Pert, *Laser ablation of Mg, Cu, and Pb using infrared and ultraviolet low-fluence lasers,* Journal of Applied Physics **94**, 1468 (2003).

[177] C. Porneala and D. A. Willis, *Time-resolved dynamics of nanosecond laser-induced phase explosion,* Journal of Physics D: Applied Physics **42**, 155503 (2009).

[178] M. Duocastella, J. M. Fernández-Pradas, J. L. Morenza, and P. Serra, *Time-resolved imaging of the laser forward transfer of liquids,* Journal of Applied Physics **106**, 084907 (2009).

[179] A. I. Kuznetsov, C. Unger, J. Koch, and B. N. Chichkov, *Laser-induced jet formation and droplet ejection from thin metal films,* Applied Physics A: Materials Science and Processing **106**, 479 (2012).

Summary

Tailored Laser-Droplet Interaction
for target formation in extreme ultraviolet sources

The advancement of digital technology in society is made possible by the ever increasing capacity of computer chips. To continue this trend, the semiconductor industry is shifting to photolithography using extreme ultraviolet (EUV) light with a wavelength of 13.5 nm. This has pushed the development and production of a complex light source that, by itself, can easily be considered a marvel of modern science, technology, and engineering. In this source, micrometer-sized tin droplets are irradiated by high-power laser pulses to produce an EUV-emitting plasma. In a search for constant improvement of this source concept the *pre-pulse* was introduced, which provided a substantial and essential increase in EUV source power. A pre-pulse is a laser pulse that is used to initiate a hydrodynamic deformation of the droplet into a target which better serves the process of EUV generation. After impact of a pre-pulse, the droplet deforms into some extended target, which is then irradiated by a following *main-pulse* to generate the EUV-emitting tin plasma. All this happens in a matter of microseconds, fifty thousand times a second, and while the droplets are traveling at around 300 km/h.

The concept and technique of the pre-pulse, and *target formation* in general, supplies the motivation for the work presented in this thesis. In this thesis we study the interaction of laser pulses and tin microdroplets with a specific focus on exploiting the tunability of laser pulses and pulse sequences, and on exploring the parameter space of laser-induced droplet deformation.

To enable this investigation a 1-micron laser system was developed which combines programmable, arbitrary pulse shapes, with a temporal resolution of approximately 0.4 ns, and pulse energies of several 100 mJ. This is achieved by shaping pulses from a continuous-wave seed laser with electro-optic modulators and subsequently amplifying these pulses using a two-stage grazing-incidence Nd:YVO_4 pre-amplifier and a Nd:YAG power-amplifier. The fine temporal shaping resolution and high-energy pulses make this system extremely versatile. In addition to being used in all experiments presented throughout this thesis, it has also been essential in several other studies at ARCNL. The laser system is presented in Chapter 2.

The shortest pulses the aforementioned laser system is capable of generating have a duration close to 0.4 ns. Such pulses are short enough to, on impact, launch shock waves into the droplet interior. In Chapter 3 we study the deformation that results from impact of such pulses. The shock waves, if intense enough, can induce cavitation and spall fracture in the droplet interior, which dictate the ensuing

deformation. Due to cavity formation in the center of the droplet, the droplet expands spherically in a bubble-like fashion. Using shadowgraphy, we quantify the expansion velocities along with the velocity of the debris generated by spallation. We find that the expansion and spall velocities mainly depend on the ratio between the laser energy incident on the droplet and the droplet volume. By combining data from several experiments using different droplet sizes and laser focal spot sizes, we conclude that this similarity holds for a remarkably large range of experimental parameters, but observe significant differences between pulses of different durations. Both the expansion and spall velocities are found to accurately follow a power-law scaling over more than two orders of magnitude.

In Chapter 4 we study what happens if the pulse duration is gradually increased up to 7.5 ns. A transition in the type of deformation takes place—from a spherical deformation dominated by cavitation and spallation, to a cylindrical expansion into a thin sheet. We qualitatively describe the observed deformation types and find scaling laws for the propulsion, expansion, and spall velocities as a function of pulse duration and energy. The ratio of the pulse duration to the acoustic timescale of the droplet is identified to be the critical parameter determining the type of deformation. Additionally, we study the influence of fast rise times by comparing deformation resulting from square- and Gaussian-shaped laser pulses.

As an alternative to single pulses, we study the droplet deformation following a two-pulse sequence of short, 0.4 ns pulses in Chapter 5. When the delay between these pulses ranges from 1 ns to 100 ns the deformation following impact shows a complex behavior. In particular, we find a strong reduction of the velocity of spall debris as a function of the interpulse delay. We attribute this deceleration of the spall-debris front to the presence of plasma pressure following second pulse impact. Furthermore, we study the effects of the energy of the second pulse and qualitatively discuss the formation of microjets.

The liquid metal tin droplet is an efficient reflector of 1-micron laser light. After a gradual heating of the droplet surface during laser pulse impact, a threshold is passed and plasma forms around the droplet, which strongly absorbs the remainder of the laser pulse through inverse bremsstrahlung. Correspondingly, any reflection from the droplet disappears at this moment of plasma formation. In Chapter 6 we use long, ~ 100 ns pulses of relatively low intensity and flat temporal shapes, and measure the duration of reflection at a small angle. We find that this duration, and thereby the moment of plasma onset follows an inverse square scaling with laser intensity due to a square-root scaling of the thermal diffusion depth with time, as is well established in literature.

Lastly, in Chapter 7, we study the mass distribution of a target currently employed in industry—a stretching sheet of liquid tin formed after ns-pre-pulse impact. By using an auxiliary, low-intensity vaporization pulse with a constant spatial and temporal intensity distribution, we gradually vaporize the sheet enabling an investigation of the sheet thickness and mass. We use this method to show that increasing the energy of the pre-pulse incident on the droplet, which enables reaching a predetermined target radius more quickly, results in a larger mass fraction remaining in the sheet.

Samenvatting

Laser-Druppel Interactie op Maat
voor doelwit formatie in extreem ultraviolet lichtbronnen

De ontwikkeling van digitale technologie in de samenleving wordt mogelijk gemaakt door de continu toenemende capaciteit van computer chips. Om alsmaar snellere computer chips te kunnen blijven maken is de halfgeleider industrie overgestapt op fotolithografie met extreem ultraviolet (EUV) licht met een golflengte van 13.5 nanometer. Deze overstap heeft geleid tot de ontwikkeling en productie van een complexe lichtbron, welke met recht kan worden beschouwd als een wonder van de moderne wetenschap en technologie. In deze lichtbron worden kleine metalen tin druppels, met een diameter van enkele tientallen micrometers, belicht met een intense laser puls. Hierdoor vormt zich een tin plasma dat het benodigde EUV licht uitstraalt. Omdat de efficiëntie van deze lichtbron gelimiteerd is—maar een paar procent van het originele laser licht word omgezet in EUV straling—is men constant op zoek naar verbeteringen. Een relatief grootte toename in efficiëntie is recentelijk bereikt door de implementatie van een zogeheten *pre-puls*. Dit is een puls die een hydrodynamische deformatie van de druppel initialiseert, en deze laat expanderen tot een groter doelwit. Het belichten van dit doelwit met een volgende laser puls, die nu de 'hoofd-puls' wordt genoemd, leidt tot meer EUV generatie dan wanneer de oorspronkelijke druppel direct word belicht. Dit proces, de belichting van de druppel met de pre-puls, de expansie, en de daarop volgende belichting met de hoofd-puls, duurt opgeteld enkele microseconden. In de industriële lichtbron gebeurt dit vijftig duizend keer per seconde, terwijl de druppels zich door een vacuüm kamer bewegen met een snelheid van 300 km/h.

Het concept van de pre-puls, en in het algemeen het transformeren van de druppel in een beter geschikt doelwit, vormt de motivatie voor het werk in deze thesis. We bestuderen de interactie van laser pulsen met tin microdruppels en leggen nadruk op het benutten van de flexibiliteit van laser pulsen en reeksen van meerdere pulsen, en het in kaart brengen van de parameterruimte van laser-geïnduceerde druppel deformatie.

Om dit mogelijk te maken is een laser systeem ontwikkeld waarbij de pulsvorm willekeurig geprogrammeerd kan worden met een resolutie van 0.4 ns en puls energieën van enkele 100 mJ worden bereikt. In dit systeem worden de pulsen gevormd door het moduleren van een continue laser met elektro-optische modulatoren. Deze pulsen worden vervolgens versterkt door een tweestaps begrazingincidentie Nd:YVO_4 voorversterker en een Nd:YAG eindversterker. De fijne controle over de pulsvorm en de hoge pulsenergie maakt het een zeer veelzijdig laser systeem. Naast

dat dit systeem is gebruikt in alle experimenten die in deze thesis worden gepresenteerd is het ook essentieel geweest voor andere studies op ARCNL. Het laser systeem word gepresenteerd in Hoofdstuk 2.

De kortste pulsen die het hierboven genoemde laser systeem kan genereren hebben een lengte van ongeveer 0.4 ns. Bij het belichten van tin microdruppels met deze pulsen worden schokgolven in de druppel gegenereerd. In Hoofdstuk 3 bestuderen we de vervorming van de druppel die volgt na inslag van dit soort pulsen. The schokgolven kunnen, als ze intens genoeg zijn, cavitatie in de druppel en ook spallatie (afsplintering) veroorzaken, welke de verdere vervorming van de druppel bepalen. Door de cavitatie in het midden van de druppel expandeert deze als een bubbel. We kwantificeren zowel deze expansie snelheid als de snelheid van de fragmenten gegenereerd door spallatie door middel van *shadowgraphy*, waarbij de schaduw van de vervormende druppel word afgebeeld. We nemen waar dat de expansie en spall snelheden voornamelijk afhangen van de verhouding tussen de laser energie invallend op de druppel en het volume van de druppel. Door het combineren van data van meerdere experimenten waarin verschillende druppel en laserbrandpunt groottes zijn gebruikt, concluderen we dat deze gelijkheid geldt over een opmerkelijk groot bereik van experimentele parameters. Echter observeren we een significant verschil voor pulsen met een verschillende lengte. Zowel de expansie als spall snelheden volgen nauwkeurig een machtsverband over meer dan twee ordes van grootte.

In Hoofdstuk 4 bestuderen we wat er gebeurt als de puls lengte geleidelijk toeneemt tot 7.5 ns. Er vindt een transitie in het type vervorming plaats—van een sferische bubbel expansie gedomineerd door cavitatie en spallatie naar een cilindrische expansie tot een dunne pizza vorm. De verschillende deformatie types worden kwalitatief beschreven en we bepalen machtsverbanden voor de propulsie, expansie, en spall snelheden als functie van de puls lengte en energie. We identificeren de verhouding tussen de puls lengte en de akoestische tijdschaal van de druppel als de primaire parameter die het type vervorming bepaald. Daarnaast bestuderen we de invloed van een snelle puls flank door het vergelijken van de vervorming die volgt na inslag van vierkante en Gaussische pulsvormen.

Als alternatief voor enkele pulsen, bestuderen we in Hoofdstuk 5 de deformatie wanneer gebruik word gemaakt van een pulspaar van korte, 0.4 ns pulsen. Als de vertraging tussen deze twee pulsen in het bereikt valt van 1 ns tot 100 ns is de resulterende deformatie zeer complex. We observeren een sterke reductie in de spall snelheid als functie van de tijd tussen de pulsen. Deze remming van de spall laag schrijven wij toe aan de aanwezigheid van een plasma druk die volgt op de inslag van de tweede puls. Aanvullend hierop bestuderen we het effect van de energie van de tweede puls en discussiëren we de vorming van microjets.

De vloeibare metalen tin druppel is voornamelijk een efficiënte reflector van het gebruikte 1-micron laser licht. Een klein deel van het laser licht word wel geabsorbeerd door de druppel en zorgt voor een geleidelijke verwarming van het oppervlak, totdat het tin warm genoeg word en er een plasma vormt. In tegenstelling tot het originele, ongestoorde oppervlak van de druppel, absorbeert het plasma praktisch al het inkomende laserlicht via het mechanisme van inverse remstraling. Het gevolg is dat de reflectie van het laserlicht dat optreedt bij het oppervlak van de druppel

verdwijnt op het moment dat het plasma zich vormt. In Hoofdstuk 6 gebruiken we lange, ~ 100 ns pulsen met een relatief lage intensiteit en vlakke tijdsvormen. Met een fotodiode meten we de duur van de reflectie van de laser puls op een kleine hoek en observeren dat de duur van deze reflectie, en daarmee het moment van plasma formatie, een omgekeerd kwadratisch verband volgt. Deze schaling volgt direct uit een in de literatuur bekend wortelverband tussen de warmtediffusie diepte en de tijd.

Tot slot bestuderen we in Hoofdstuk 7 de massa verdeling van een doelwit dat momenteel gebruikt word in de industrie—een rekkende pizza vormige dunne laag vloeibaar tin die vormt na inslag van een ns-pre-puls op de druppel. Door gebruik te maken van een extra laser puls met een lage en constante intensiteit verdampen we deze dunne laag geleidelijk. Hiermee kunnen we het dikte profiel van dit soort doelwitten bestuderen en verkrijgen we informatie over de totale massa distributie. We gebruiken deze methode om te laten zien dat een hoog energetische pre-puls voordelig is voor het behoud van tin massa in de centrale laag. Doordat door de hogere puls energie een snellere expansie word gestart, en hiermee het benodigde formaat van het doelwit eerder wordt bereikt, zal een lagere fractie van de totale massa zich verplaatst hebben naar de rand en van daaruit naar fragmenten.

List of Publications

Chapter Two

R. A. Meijer, A. S. Stodolna, K. S. E. Eikema, and S. Witte, *High-energy Nd:YAG laser system with arbitrary sub-nanosecond pulse shaping capability*, Optics Letters **42**, 2758 (2017).

Chapter Four

R. A. Meijer, D. Kurilovich , K. S. E. Eikema, O. O. Versolato, and S. Witte, *The transition from short- to long-timescale pre-pulses: Laser-pulse impact on tin microdroplets*, In preparation.

Chapter Five

R. A. Meijer, R. Schupp, J. Sheil, Mikhail M. Basko, K. S. E. Eikema, O. O. Versolato, and S. Witte, *Spall-velocity reduction in double-pulse impact on tin microdroplets*, Physical Review Applied **16**, 024026 (2021).

Chapter Six

R. A. Meijer, D. Kurilovich, B. Liu, Z. Mazzotta, J. Hernandez-Rueda, K. S. E. Eikema, O. O. Versolato, and S. Witte, *Laser ablation threshold of liquid tin microdroplets*, Submitted.

Chapter Seven

B. Liu*, R. A. Meijer*, J. Hernandez-Rueda, D. Kurilovich, Z. Mazzotta, S. Witte, and O. O. Versolato, *Laser-induced vaporization of a stretching sheet of liquid tin*, Journal of Applied Physics **129**, 053302 (2021).

*These authors contributed equally.

The author has also contributed to the following publications:

6. T. de Faria Pinto, J. Mathijssen, R. A. Meijer, H. Zhang, A. Bayerle, D. Kurilovich, O. O. Versolato, K.S.E. Eikema, and S. Witte, *Cylindrically and non-cylindrically symmetric expansion dynamics of tin microdroplets after ultrashort laser pulse impact*, Applied Physics A **127**, 93 (2021).

5. L. Behnke, R. Schupp, Z. Bouza, M. Bayraktar, Z. Mazzotta, R. A. Meijer, J. Sheil, S. Witte, W. Ubachs, R. Hoekstra, and O. O. Versolato, *Extreme ultraviolet light from a tin plasma driven by a 2-µm-wavelength laser*, Optics Express **10**, 1364 (2021).

4. J. Scheers, R. Schupp, R. A. Meijer, W. Ubachs, R. Hoekstra, and O. O. Versolato, *Time- and space-resolved optical Stark spectroscopy in the afterglow of laser-produced tin-droplet plasma*, Physical Review E **102**, 13204 (2020).

3. F. Torretti, J. Sheil, R. Schupp, M. M. Basko, M. Bayraktar, R. A. Meijer, S. Witte, W. Ubachs, R. Hoekstra, O. O. Versolato, A. J. Neukirch, and J. Colgan, *Prominent radiative contributions from multiply-excited states in laser-produced tin plasma for nanolithography*, Nature Communications **11**, 2334 (2020).

2. R. Schupp, F. Torretti, R. A. Meijer, M. Bayraktar, J. Sheil, J. Scheers, D. Kurilovich, A. Bayerle, A. A. Schafgans, M. Purvis, K. S. E. Eikema, S. Witte, W. Ubachs, R. Hoekstra, and O. O. Versolato, *Radiation transport and scaling of optical depth in Nd:YAG laser-produced microdroplet-tin plasma*, Applied Physics Letters **115**, 124101 (2019).

1. R. Schupp, F. Torretti, R. A. Meijer, M. Bayraktar, J. Scheers, D. Kurilovich, A. Bayerle, K. S. E. Eikema, S. Witte, W. Ubachs, R. Hoekstra, and O. O. Versolato, *Efficient generation of extreme ultraviolet light from Nd:YAG-Driven microdroplet-tin plasma*, Physical Review Applied **12**, 014010 (2019).

Acknowledgements

I joined ARCNL, I would say, when it was still in its early teenage years. With half-empty labs and students walking around somewhat clueless, including me. Slowly the labs were being filled with equipment and experiments started to take shape. This was the start of a PhD journey in which I've learned and done so much more than I ever thought I would. Many years of hard, but exciting work followed and eventually led to the realization of this thesis. Of course I did not do all the work alone. I was very fortunate to be part of a research group and institute with some amazing people that have helped me along the way.

Stefan, thank you for giving me this opportunity and for all your guidance and support. Your positive mentality and patience seem inexhaustible and made it always easy for me to walk into your office for a brief discussion or some advice, even when I was holding expensive broken optics. Before I joined the group as a PhD student, I first came to you for a small one-month lab project that I still needed to do to complete my master. It was a great way to get a taste of the atmosphere in the group, which, very much thanks to you, has always been very welcoming and relaxed.

Kjeld, thank you for everything, for all your advice, for the humour you brought to the group, and especially for all the help in the lab during the first year. Discussing laser-building experiences and tricks never gets old, although sometimes it felt more like learning about myth and fairy tales.

Aneta, thank you for teaching me the ropes. You were a great example to me and to the rest of the group. You laid the base for the now named *SNS* laser system and the success it has become. All these long days, tinkering in the lab, staring at the scopes, tweaking the alignment, they were worth it in the end. I could not have done it without your help.

Tiago, thank you for being my laser-building companion and friend on the opposite side of the optical table and in the office. It was great being able to share experiences and learn from each other. I think we were very lucky to be sent to the ASSL 2016 conference in Boston as two rookie PhD students. There, you developed a brief(?) addiction to Boston Kreme donuts and we couldn't help but (inappropriately) laugh at a particular event occurring daily on the street in front of the hotel. Together with Aneta, I felt we formed a little laser-lab team, fortunately sharing the somewhat obsessive need for order and tidiness in the lab.

Nik, without your technical support my PhD life would have been a whole lot harder. Thank you for always being there to help and also for your positive,

lighthearted, and upbeat character. Nowadays, whenever I encounter a technical issue I often think to myself 'what would Nik do', that says a lot.

Zeudi, I don't think there could've been a better person to "inherit" the laser system. You came at just the right moment, helped move it to the new lab, and brought it back to life with a meticulous approach. Thank you for that, and for the energy you brought and still bring to the group.

I would like to thank all other members that were part of the EUV Generation & Imaging group during my PhD time, for their helpful work advice, collaboration, and for their social presence. In particular I would like to mention Ale, Amelie, Anne, Dirk, Faisal, Hao, Jan, Kevin, Lars F., Lars L., and Thijs.

After the first part of my PhD project, assembling the laser system, was done, it was time to start doing experiments with tin droplets. This, I did in collaboration with the EUV Plasma Processes group, from which I would like to thank Oscar and all the members for all their help and support. I would especially like to acknowledge my co-authors Bo, Dmitry, Javier, John, and Ruben for their contributions.

The experiments would never have worked out the way they did without the many minds and hands at work in the various technical support departments of AMOLF and ARCNL. They have been essential to getting these amazing experiments to work at a high level. I would like to in particular thank Duncan, Marco S., Jorijn, and Henk-Jan for their hard work. Thanks also to all other group technicians that in one way or another contributed to the work in this thesis.

I should not forget how I ended up doing this work in the first place. Thank you Mr. Bruning for making physics so enjoyable in high school. Ewold, Rick, and Freek, thank you for making my master internship at AMOLF the experience that motivated me to do a PhD.

Naturally, there is more to life than work and I'm tremendously grateful to have been surrounded by so many great colleagues and friends that made life outside of work so rich.

Ale, we became friends during our internships at AMOLF and have since then shared many laughs and beers, at and outside of ARCNL. Thank you for showing me your hometown, the magnificent metropolitan city of Bari. I will never forget the burning pain I felt as the fluid mozzarella, like lava from a volcano, escaped the panzerotto and made its way across my hand.

Vanessa, thank you for being you, and for not kicking my ass after I asked you "what did you say?" for the gazillionth time. Tomorrow I will go to Italy to visit you, I'm sure we'll have a great time as we did so many times before in Amsterdam.

Nothing beats traveling with friends. Thank you Görsel and Victor for the amazing time we had in Greece. Remember to bring a shirt next time when you go hiking in the scorching sun. Oh, and a dozen bottles of water, two for drinking and ten for Görsel to pour over himself.

Stephen, John, and Lianjia, I'm sorry I didn't actually warn you when I noticed that the dust devil was on a collision course with our car when driving through Death Valley. Oh well, we made it out alive with some scratches and one more story to tell. Thank you for all the fun times, the beers in Vegas, the beers in that one shady bar in the dessert town, and many more.

Thanks everyone, for all the enjoyable coffee breaks, foosball games, borrels, parties, BBQs at the Flevopark, beach volleyball games, birthdays, dinners, and outings. Although I'm sure I'm forgetting some people, let me also name Ale T., Camila, Christina, Daan, Felix, Fengchun, Filippo, Fiona, Guido, Joris, Lucas, Maarten, Najmeh, Neha, Reinout, Robbert, Sylvianne, Thomas, Vasco, Zazo, and Zoey.

I would also like to thank my paranymph and friend Tony for all the relaxing evening drinks and dinners with you and Eva, they were a great distraction from the PhD work.

Maisie, you have been around for all of it, the work, the laughter, the traveling. I'm not sure if I would've made it through without you. Thank you for everything.

Last but not least, I would like to thank all my family, my sister, and my parents for their everlasting interest and support.